Near-Field Structure-Borne Sound Holography: Extrapolation of bending wave fields in homogenous plates

vorgelegt von Dipl.-Ing. Dietmar Greussing
geb. in Bregenz

von der Fakultät V - Verkehrs- und Maschinensysteme
der Technischen Universität Berlin
zur Erlangung des akademischen Grades

Doktor der Ingenieurwissenschaften (Dr.-Ing.)

genehmigte Dissertation

Promotionsausschuss

Vorsitzender:	Prof. Dr.-Ing. Gerd Holbach
Gutachter:	Prof. Dr.-Ing. Michael Möser
Gutachter:	Prof. Dr.-Ing. Martin Ochmann

Tag der wissenschaftlichen Aussprache: 06. Oktober 2014

Berlin 2014

D 83

Acknowledgements

My thanks go out to my dear family and friends, mostly for not being acoustic engineers. They provide distraction when distraction is needed and they remind me of the things that truly matter. On the occasion that physics come up, they do not forget to remind me of my grades in school as well.

I would like to thank my colleagues at the Institute of Fluid Dynamics and Engineering Acoustics, be it the guys at the workshop, the ladies guarding the doors of the secretariat or the fellow academic staff. Kudos for providing so many exchanges of thought that ultimately informed this work. I especially need to thank Dipl.-Ing. Agnes Sayer, who did most of the heavy listening and discussing. If there is any single person I should dedicate this thesis to, it is her, but I assume she has seen quite enough of it.

Thanks to Prof. Björn Petersson for providing the interesting idea that led to this thesis. Thanks to Prof. Martin Ochmann for kindly agreeing to stand in as examiner. Finally, I want to express my gratitude to Prof. Michael Möser, who readily took on my supervision and supported my work unconditionally.

Dietmar Greussing

Abstract

This thesis investigates the extrapolation of bending wave fields in homogenous plates. Using a number of structural response measurements, the continuous spatial field and the spectra of the response are reconstructed without knowledge of the mechanical boundaries or the excitation forces. It is clarified whether the deliberate inclusion of the structural near-fields close to sources and boundaries can be beneficial in the process.

Two methods are therefore presented. The first one represents an application of Fourier transform-based Near-Field Acoustic Holography in a structure-borne sound setting. The use of a polar coordinate system allows analytical propagation functions to be convolved and deconvolved with boundary values measured in the structural near-field of the plate. Because this constitutes an inverse problem, numerical stabilization in the form of wavenumber filtering and regularization is applied. The second method utilizes the Kirchhoff-Helmholtz integral and requires far-field conditions at the measurement positions. It constitutes the solution of a direct problem in comparison and is not restricted to a specific coordinate system for measurement.

The methods are evaluated through a series of simulations and experiments, considering three distinct cases: the infinite plate, the fully free and the simply supported plate, excited by normal point forces, respectively. In terms of the usually neglected influence of the near-field, the latter two can be seen as worst and best case scenarios for the wide range of possible boundary conditions in engineering practice.

It is found that the average reconstruction error to be expected from holography ranges from 1 dB to 3 dB, depending on the boundary condition. The method is not very well suited to analyze very narrow frequencies in a spectrum, and the extrapolatable plate area is inherently limited. The Kirchhoff-Helmholtz integral-based method leads to an average reconstruction error between 2 dB and 3 dB. As with the holographic method, the observed deviations at individual field positions and frequencies can be significantly larger, however. The presence of near-fields requires a distance of at least a sixth of the considered bending wavelength between measurement positions and structural discontinuities.

Zusammenfassung

Diese Arbeit beschäftigt sich mit der Extrapolation von Biegewellenfeldern in homogenen Platten. Ohne Kenntnis der mechanischen Randbedingungen oder der anregenden Kräfte werden sowohl das kontinuierliche räumliche Wellenfeld als auch die Spektren der Strukturantwort anhand von Strukturantwort-Messungen rekonstruiert. Es wird aufgezeigt, inwiefern die bewusste Einbeziehung von Körperschall-Nahfeldern im unmittelbaren Bereich der Quellen und der Ränder der Struktur von Vorteil sein kann.

Hierfür werden zwei Verfahren vorgestellt. Das erste Verfahren stellt eine Anwendung des Prinzips der akustischen Nahfeldholographie im Körperschallbereich dar. Die Wahl eines Polarkoordinatensystems ermöglicht eine Extrapolation des Feldes durch Faltung und Entfaltung von analytischen Ausbreitungsfunktionen mit Randbedingungen, die im strukturdynamischen Nahfeld gemessen werden. Da dieses Vorgehen der Lösung eines inversen Problems entspricht, kommt zudem numerische Stabilisierung in Form von Wellenzahlfilterung und Regularisierung zur Anwendung. Das zweite Verfahren verwendet die Theorie des Kirchhoff-Helmholtz Integrals und setzt Fernfeldbedingungen an den Messpositionen voraus. Dies stellt eine direkte Lösung des Ausbreitungsproblems dar und erfordert im Gegensatz zur Nahfeld-Methode kein spezifisches Koordinatensystem für die Messungen.

Beide Verfahren werden in einer Reihe an Simulationen und Experimenten anhand von drei distinktiven Fallbeispielen evaluiert: eine unendlich ausgedehnte Platte sowie eine vollständig freie und eine einfach aufgestützte Platte, jeweils angeregt durch Punktkräfte normal zur Plattenoberfläche. Im Hinblick auf die oftmals vernachlässigten Nahfelder stellen die beiden letzteren Beispiele Extremfälle für die große Bandbreite an unterschiedlichen Randbedingungen in der Realität dar.

Die Untersuchungen zeigen, dass der zu erwartende mittlere Rekonstruktionsfehler des holographischen Verfahrens zwischen 1 dB und 3 dB liegt, abhängig von der Randbedingung. Das Verfahren ist nicht zur Beurteilung von sehr schmalbandigen Spektren geeignet und der extrapolierbare Bereich der Platte ist geometrisch eingeschränkt. Das Verfahren auf Basis des Kirchhoff-Helmholtz Integrals führt im Mittel zu Rekonstruktionsfehlern zwischen 2 dB und 3 dB. Wie bei der Nahfeld-Methode können für einzelne Feldpunkte und Frequenzen auch deutlich größere Abweichungen beobachtet werden. Im Fall von signifikant auftretenden Nahfeldern sollte dabei ein Messabstand von mindestens einem Sechstel der betrachteten Biegewellenlänge zu den Diskontinuitäten in der Struktur eingehalten werden.

Contents

1
Introduction

1.1 Motivation

In the field of acoustics, several analyses require the reconstruction of a structural wave field. Special attention is thereby given to plate-like structures, since they occur very frequently in engineering practice. Both sound radiation and structural health are strongly related to the propagation of bending waves in plates or shells, and a thorough analysis of any related problem requires, or at least profits from, the spatial mapping of the resulting vibrations.

If provided with details about the mechanical excitation and the boundary conditions, engineers nowadays have a wide range of numerical options in order to calculate the resulting bending wave field directly. Unfortunately, however, the strength or exact location of any applied excitation is often unknown in practice. Depending on the intricacy of the construction, the true boundary conditions may be estimated at best. For this reason, researchers have constantly been looking for ways to reconstruct bending-related wave fields from experimental data rather than relying solely on numerical predictions.

Independent of the type of field to be reconstructed, a significant amount of input data is needed to reconstruct a continuous field. While many different approaches exist, they either require the measurement of forces or the measurement of the response over an area that covers the whole plate. Measurement of forces or moments can prove difficult if the structure cannot be set up under laboratory conditions. Measurement of the whole plate surface can become a chore if an expensive scanning system is not available. It might be downright impossible if some areas of the plate are not accessible for measurement in situ.

As a consequence, the question arises whether it is possible to reconstruct the continuous field from input data that does not have to be collected evenly across the whole structure. Herein lies the general research context and motivation for this thesis: the problem of structural wave field extrapolation.

When it comes to reconstructing or actively controlling structure-borne sound fields, existing methods usually require the negligence of structural near-fields. This is often justified since the corresponding terms complicate the mathematical model but do not affect a greater part of the field. The existence of structural near-fields is basically a nuisance. As a practical consequence, measurement in the near-field region is prohibited, however, which poses a problem if the wavelength is large or if measurements have to be made close to a structural discontinuity. Yet in the field of fluid-borne sound, the arguably most established method for wave field extrapolation, Near-Field Acoustic Holography,[1] draws its main adavantages from including the (hydrodynamic) near-field. This interesting circumstance leads to the questions that serve as the specific motivation for this thesis: Is it possible to perform a procedure analogous to Near-Field Acoustic Holography in the structure-borne sound domain? Would this be preferable over a similar far-field-based method?

1.2 Aims of this thesis

This thesis sets out to investigate a method for wave field extrapolation in a pure structure-borne sound scenario, that is, the reconstruction of a continuous bending wave field based on a limited number of structural response measurements. It is postulated that the bending wave field of homogenous plates can be propagated forward and backward through a procedure that follows the basic idea behind Fourier transform-based Near-field Acoustic Holography. It is further postulated that the bending wave field can be extrapolated in a mathematically different but practically similar fashion, based on the utilization of the Kirchhoff-Helmholtz integral in the far-field of the plate. It is to be shown that with both methods neither mechanical boundary conditions nor the excitations need to be known beforehand, assuming that a true bending wave field is observed under stationary conditions.

This thesis seeks to evaluate and compare the accuracy and feasability of the proposed methods in both theory and practice. It aims to clarify to which extent the inclusion of near-field influences improves the results. It further aims to determine a practical criterion for the satisfaction of the near-field (or far-field) requirement and to suggest suitable measurement parameters.

1.3 Methodology

In order to gain perspective on the investigations presented in this thesis, a literature survey is conducted in Chapter 2. The main purpose of the survey is to discuss those branches of acoustical research that share “DNA” with the present

[1] Early literature refers to the method as “Nearfield Acoustic Holography” or “Nearfield Acoustical Holography”.

work. There are many approaches to vibro-acoustic field reconstruction and therefore the number of related research aspects is very large. It is intended to highlight mainly the aspects that will appear in this thesis in some form as well. Chapter 2 is therefore not a thorough overview of acoustic wave field reconstruction and extrapolation techniques in general. It should act as a preview on the subjects that together form the body of this thesis and help to identify future research possibilities in the conclusions.

The theoretical groundwork for near-field-based extrapolation through Fourier transforms is laid in Chapter 3. First, the principles of fluid-borne NAH are discussed in some detail because their structure-borne counterpart is analogous in many ways. The sought-after formulae is then derived, and the corresponding procedure for infinite and finite plate structures is outlined and illustrated. Because the near-field-based method poses an "inverse" problem by nature, the resulting numerical challenges are discussed toward the end of Chapter 3. In Chapter 4, the formulae for far-field-based extrapolation by means of the Kirchhoff-Helmholtz integral is derived. The corresponding procedure for infinite and finite plate structures is outlined and illustrated, with a short discussion of the application of the Boundary Element Method in the infinite case.

As a first step in evaluating the methods, different numerical case studies are performed in Chapter 5. Primarily, an infinite plate, a free plate and a simply supported plate are considered. The infinite case thereby represents the very basic, academic scenario. The free plate is a rather academic scenario as well and represents an extreme case due to its significant near-field influence and its high modal density. The simply supported plate, which has no near-fields at the edges, can be seen as the other extreme. The choices therefore represent best and worst case scenarios. Investigating both extremes is assumed to give a good indication on how the two methods will handle different boundary conditions in general. Both the continuous reconstruction of the spatial velocity response field as well as the reconstruction of response spectra are simulated. A study of different measurement parameters is conducted for the case of the infinite plate. For the sake of completeness, a stiffened infinite plate and a plate with more arbitrary geometry and boundaries are simulated as well.

As a second step in the evaluation, the simulated cases will be studied by experiment in Chapter 6. An infinite perspex plate, a free aluminum plate and a simply supported aluminum plate are used to test the methods under laboratory conditions. Again, the continuous reconstruction of the spatial velocity response field as well as the reconstruction of response spectra are performed. As a conclusion of this analysis, the experimental results are compared to equivalent simulated results, which brings the identified reconstruction error into perspective.

Chapter 7 closes the discussion presented in this thesis with a final assessment of the presented methods, weighing the advantages and disadvantages. Suggestions for future research possibilities are provided.

2
Related Research

As noted and exemplified by Bobrovnitskii [1], the problem of reconstructing continuous sound or vibration fields from a limited amount of measurement data is frequently encountered in acoustics and structural dynamics. It has also been extensively investigated in other fields, such as seismology, medical diagnostics or non-destructive testing, resulting in a truly vast body of literature on the subject in general. The following literature survey considers research that aims or allows to reconstruct structure-borne sound fields in plates. This is a wide field itself, with very different approaches. Many of these approaches deal with certain physical or numerical problems that are partial aspects of the general problem discussed in this thesis. The survey focusses mostly on a few key references whose topics of discusion can be found within this thesis in some form. It is acknowledged that an exhaustive overview on the subject is thereby not provided.

The existing approaches might roughly be categorized according to the type of field that is to be reconstructed or according to the type of measurement data that is utilized to do so. Among these approaches, one might furthermore distinguish a class that attempts the reconstruction of a continuous field from a limited number of decidedly localized measurements. This is generally referred to as *wave field extrapolation* and is attempted in this thesis in a specific manner. By categorizing according to the type of reconstructed field, three focal points can be identified in the literature: applied load distribution, structural intensity field and structural displacement field.

The first may be denoted as *force reconstruction* (FR)-techniques. They are primarily aimed at identifying magnitude and phase of the forces exciting the plate, which in turn may be used to calculate the vibratory response at any part of the structure as a benefit. This requires that the structure is well-known and that an analytical or numerical model can be established, however. As seen in a literature review by Dobson and Rider [2], conventionally, point forces can be de-

termined using the measurement of transfer functions if the location of the forces is known. Under practical conditions, direct measurement of the required transfer functions may be cumbersome, which is why procedures based on the measurement of response data have been investigated. In this regard, Zhang and Mann [3, 4] investigated the reconstruction of a spatial force distribution based on the structural intensity distribution. The structural intensity was thereby determined from discrete measurement of the normal velocity of the entire plate. It was shown that the force distribution can be calculated directly in the wavenumber domain, using two-dimensional Fourier transforms in conjunction with wavenumber filtering and spatial windowing.

In order to be able to reconstruct a local part of the force field from localized measurements only, Pézerat and Guyader [5] proposed to use the *Force Analysis Technique* (F.A.T.) [6]. The approach consists of a discretization of the equation of motion by a finite diffference scheme and the use of either singular value decomposition or wavenumber filtering in order to render the inverse procedure numerically stable. Other researchers have pursued approaches in which the distributed load is described by a superposition of modal basis functions whose contribution can be determined by measurement of the structural response. Liu and Shepard [7] therefore used modified basis functions that are required to be defined merely over the finite region of the force. Arguing that modal expansion approaches only allow reconstruction in a limited frequency range, Jiang and Hu [8] proposed a procedure in which only a number of appropriate modes are selected. In general, most force reconstruction techniques rely on severe numerical stabilization due to the ill-posedness of the problem and can therefore be inconvenient in practice [9].

The second focal point is the reconstruction of structural intensity fields. Because structural intensity is a vectorial quantity that describes the magnitude and direction of power flow, it is well-suited to analyze noise and vibration problems. Determination of the bending wave intensity requires the computation of the spatial derivatives of the normal velocity field. It has been shown by Williams et al. [10] that the spatial derivatives can be obtained using forward and inverse Fourier transforms of the normal velocity field. Later, Pascal et al. [11] suggested to use this kind of data processing in conjunction with laser vibrometer measurements, which was subsequently pursued by several authors. As with FR, spatial data processing is required in order to reduce the influence of measurement noise in the reconstruction process. Morikawa et al. [12] as well as Nejade and Singh [13] investigated different wavenumber filtering techniques, for instance. Arruda and Mas [14] proposed to improve spatial data processing by using discrete Fourier series with arbitrary fundamental period instead of conventional Fourier transforms, which would also allow for non-equally spaced measurement grids.

While the investigated approaches differ in computational terms, their practical basis is always the sampling of the response over the entire surface of the plate. Halkyard and Mace [15] presented a different procedure, in which far-field condi-

tions remote from discontinuities were assumed so that a Fourier series representation of plane waves could be employed to calculate the bending wave intensity. A circular assembly of accelerometers was thereby used to evaluate the Fourier coefficients, from which the required plate response and its spatial derivatives could be determined. However, the procedure does not allow a continuous extrapolation of the normal velocity field from a limited number of localized measurements.

The third and more recent focal point is the reconstruction of the displacement field for real-time structural health monitoring, predominantly through *shape sensing* techniques, based on finite element analysis. Tessler and Spangler [16, 17] used the minimization of a least-squares error function that compared analytical and experimentally measured strains to develop an inverse *Finite Element Method* (FEM). The continuous displacment field can thus be reconstructed if strain sensors are distributed over the entire surface, with the sensor locations corresponding to the (coarse) FEM-mesh. Chierichetti and Ruzzene [18] suggested an iterative procedure in which a repeatedly updated estimation of the structural load is used to compare the structural response of an FEM-model with the experimentally measured response. The approach requires fewer sensor positions that do not have to be extensively distributed. The sensor position has to be chosen carefully, however, and the approach requires good knowledge of the structure in order to generate a corresponding FEM-model.

Another approach to the reconstruction of structural displacement from a few localized sensor positions is the utilization of beamforming theory. Berkhout et al. [19] developed an algorithm for the removal of dispersion from bending wave datasets, allowing the principles of array-based acoustic imaging to be applied to bending wave propagation. The difference between *acoustic imaging* and *wave field reconstruction* was clarified by Maginness [20], who stated that imaging "is taken to mean the production of pictures having geometrical congruence to such discontinuities as may be of interest within the medium. Field reconstruction on the other hand is, as the term implies, merely estimation of the field parameters over a region of interest." Following Berkhouts research, Hoerchens [21] showed that a line or circular array of structural response measurements can be used to localize sources and visualize discontinuities in plates effectively. Only far-field measurements were considered, as the benefit of including the near-field was deemed to be negligible for imaging purposes in plate-like structures. Hoerchens and de Vries [22] showed that the resolution of the images is improved by taking into account boundary reflections. The above method for extrapolation relies on the use of the Rayleigh integral predominantly, which in principle is a special case of the Kirchhoff-Helmholtz integral. With its clear focus on imaging, it appears that this line of research has not fully explored the reconstruction of a continuous bending wave field itself. Yet the underlying application of Rayleigh or Kirchhoff theorems in the structure-borne sound domain could be put to further use in that regard. The Kirchhoff-Helmholtz integral in particular already forms the basis for

wave field extrapolation in very different scientific fields. In fact, Doelman [23] showed in a general manner that it can be used for wave field extrapolation in any bounded or unbounded homogenous medium. The mathematical operation was thereby simplified by decomposing the field into a series of eigenfunctions that could be extrapolated seperately. Also, waves travelling back and forth were extrapolated separately. The latter is a known approach in geophysics, where the elastic formulation of the Kirchhoff-Helmholtz integral can be used to reconstruct the seismic wave field through a layered medium [24, 25]. In electroacoustics, the conventional formulation of the integral can be used to control the acoustic environment [26] in what is now known as *wave field synthesis*. It is therefore justified to assume that it can be used to extrapolate a bending wave field in a homogenous plate as well.

While it is intuitive to calculate a structure-borne sound quantity from structural response measurements, it might be attempted from measurements in the adjacent fluid as well. Williams et al. [10] demonstrated how the structural intensity of a vibrating plate can be determined using acoustic holography. The concept of acoustic holography, dating back to around 1966 [27], first introduced a promising way to project wave fields, in which the inverse problem of wave field reconstruction was solved by "*backtracking the pressure field in space and time towards the source*" [28]. Williams and Maynard [29] showed that the reconstruction at the source has to include evanescent waves in order to differentiate acoustic sources that are separated by a distance less than a wavelength. Consequently, Maynard et al. [30] addressed the problems of conventional holography through the method of *Near-Field Acoustic Holography* (NAH). The case of NAH for cylindrical geometry was subsequently considered by Williams and Dardy [31]. In classic NAH, or closely related acoustic wave extrapolation methods considered by Candel and Chassaignon [32] or Blacodon et al. [33], the sound pressure field is initially obtained very close to the source, on a surface in either plane, cylindrical or spherical coordinates, and is then decomposed into its plane wave components by means of a spatial Fourier transform. By solving the Helmholtz equation in the wavenumber domain, the field can be extrapolated from one surface to another and then be reconstructed by applying an inverse transform. In this way, the wave field can be backward-propagated right onto the surface of the radiating structure, as long as it is conformal to the chosen separable geometry. In the case of a vibrating plate, the surface field can therefore be calculated from sound pressure measurements in the immediately adjacent surrounding fluid.

In order to apply NAH to structures with arbitrary shape, the numerical solution of a system of integral equations, i.e. the Kirchhoff-Helmholtz integral equation, instead of analytic Fourier transforms was pursued by Veronesi et al. [34]. This led to research by Kim and Lee [35], Bai [36], Kim and Ih [37] and many others, in which the *Boundary Element method* (BEM) is used to solve the integral equations, now referred to as BEM-based NAH.

As the survey shows, the reconstruction of a structure-borne sound field from a limited number of measurements usually requires either good knowledge of the structure, i.e. material properties, geometry and boundary conditions, or measurements that are evenly distributed across the whole structure. An extrapolation approach that allows to reconstruct and clearly visualize the bending wave response of a plate without the need for numerical modeling appears to be missing. Since NAH is capable of determining the desired field information solely based on acoustic response measurements, it needs to be investigated whether the underlying theory can be transferred to the structure-borne sound domain. A similar procedure based on structural response measurements would be a promising way to achieve structural wave field extrapolation. These considerations lead to Chapter 3. Given that NAH is a near-field- and wave-based approach, it is fair to ask whether a far-field wave-based approach would be more convenient ultimately. This question leads to Chapter 4. The subsequent chapters demonstrate how these purely wave-based approaches hold up in theory and in practice.

3

Theory for Near-Field Structure-Borne Sound Holography

In this chapter, the bending wave equation for thin homogenous plates is used to derive a formulation for the extrapolation of the normal structural velocity. The author has previously presented a shortened form of the derivation for infinite plates [38] and used the related solution for finite plates to present preliminary studies [39, 40]. The formulation represents a set of expanded eigenfunctions of the plate in polar geometry and allows to perform a procedure that is analogous to Near-Field Acoustic Holography, albeit in a pure structure-borne sound context. The practical procedure for the presented method is discussed step by step. As an inverse problem, the method comes with typical numerical issues, wherefore the use of wavenumber filtering and regularization is discussed. The significance of the near-field and its implications for the procedure are discussed as well.

3.1 On the principle of Near-Field Acoustic Holography

Broadly speaking, the principle of holography is applied whenever the analysis of a distinct part of a wave field is used to reconstruct the continuous field. The Greek words *holos* and *gramma* mean *whole* and *message*, indicating that a *hologram* holds all the required information. More specifically, acoustic holography is synonymous with the act of using a two-dimensional spatial segment (the hologram) of a sound field in order to reconstruct a series of remote two-dimensional segments (images) which together form the continuous three-dimensional field. In general terms, such extrapolation is made possible if the eigenfunctions of the medium and a specific set of boundary informations are known. In Fourier transform-based NAH specifically, "*...one simply measures a uniform (Dirichlet or Neumann) boundary condition on a surface for which there is a known Green's function. The holographic reconstruction process is then simply the convolution (or deconvolution)*

of the measured boundary values with the Green's function" [30]. In practice, this means that the spatial sound pressure field is measured on said surface and is then decomposed into its plane wave components by means of a two-dimensional spatial Fourier transform. These plane wave components are the eigenfunctions for the considered acoustic medium. In this way, the field is transformed to an eigenspace wherein the wave field can be propagated by multiplication with a propagation function. In order to establish the propagation function or propagator, Green's function[1] must be known. A multiplication with the propagator corresponds to shifting the magnitude and the phase of the wave field in the wavenumber domain. Therefore, by taking the inverse Fourier transform again after the multiplication, a projection of the spatial field from one surface to another is made. The actual spatial sound pressure field can thus be reconstructed at positions remote from the initial measurement.

The procedure that constitutes Fourier transform-based NAH requires a separable coordinate system, i.e. a coordinate system that allows all solutions of a partial differential equation to be built up by a linear combination of separated solutions, each dependent on only one coordinate [41]. The coordinate system must be able to describe level surfaces that are a function of two coordinates while the third coordinate is constant, as depicted in Fig. 3.1. Only then can the wave field be projected from surface to surface along the remaining third coordinate. The permitted coordinate systems are those of planar, cylindrical and spherical coordinates because they grant a solution through analytical eigenfunctions that satisfy the boundary conditions on level surfaces.

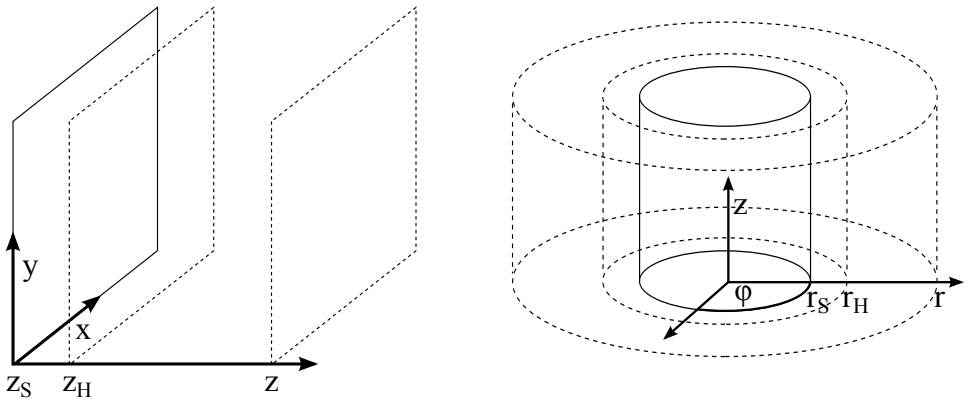

(a) planar (Cartesian) coordinates **(b)** cylindrical coordinates

Figure 3.1: Examples for separable coordinate systems.

[1] A stickler's aside: In this thesis it will either be referred to "Green's function" or "the Green function", depending on what seems grammatically reasonable to the author. In any case, both denote the same.

The characteristic aspect of all NAH-procedures is that the hologram must be obtained on a surface very close to a radiating sound source in order to include important evanescent wave information. The aimed-at image surfaces, on the other hand, might be located much further away from the source or even closer to the source than the hologram surface, constituting either a forward- or a backward-propagation problem. In acoustics, the term *holography* is often associated with the latter, since the ability to propagate toward the radiating source is especially appealing. If the source has a surface that is conformal to the chosen hologram surface, it is ultimately possible to calculate the surface velocity of the source. The mathematical description of Fourier transform-based NAH for planar and cylindrical coordinates is given in Eqs. (3.1.1) and (3.1.3), respectively.

The sound pressure p on a source plane can be calculated by

$$p(x, y, z_\mathrm{S}) = \mathcal{F}_x^{-1}\mathcal{F}_y^{-1}\left\{\mathcal{F}_x\mathcal{F}_y[p(x, y, z_\mathrm{H})]Q^\mathrm{f}(k_x, k_y, z_\mathrm{S} - z_\mathrm{H})\right\}, \tag{3.1.1}$$

with the propagator

$$Q^\mathrm{f}(k_x, k_y, z_\mathrm{S} - z_\mathrm{H}) = \mathrm{e}^{jk_z(z_\mathrm{S}-z_\mathrm{H})}. \tag{3.1.2}$$

Here, $z = z_\mathrm{H}$ is the location of the hologram plane and $z = z_\mathrm{S}$ is the location of the source plane. The sound pressure on a source cylinder can be calculated by

$$p(r_\mathrm{S}, \varphi, z) = \mathcal{F}_\varphi^{-1}\mathcal{F}_z^{-1}\left\{\mathcal{F}_\varphi\mathcal{F}_z[p(r_\mathrm{H}, \varphi, z)]Q^\mathrm{f}(k_\varphi, k_z, r_\mathrm{S} - r_\mathrm{H})\right\}, \tag{3.1.3}$$

with the propagator

$$Q^\mathrm{f}(k_\varphi, k_z, r_\mathrm{S} - r_\mathrm{H}) = \frac{H_n^{(2)}(kr_\mathrm{S})}{H_n^{(2)}(kr_\mathrm{H})}. \tag{3.1.4}$$

Here, $r = r_\mathrm{H}$ is the location of the hologram surface and $r = r_\mathrm{S}$ is the location of the cylindrical source surface. Eqs. (3.1.2) and (3.1.4) are the so-called pressure propagators for plane and cylindrical waves in a fluid. For imaginary arguments, corresponding to subsonic wavenumbers, the propagators represent an exponential increase toward the source.

Because the reconstruction of the source field requires the source to be conformal to the hologram surface, the choice of a suitable coordinate system, e.g. planar, cylindrical or spherical, depends on the geometry of the source surface. If a planar image is backward-propagated toward a cylindrical source for example, the reconstruction of the continuous field can only be achieved to the point where the propagated image first "touches" the cylinder, never beyond. Because the utilized solution to the wave equation is only valid in a source-free medium, the hologram surface separates the valid extrapolatable region from the source region. If the hologram surface encloses all the sources, this is known as an *exterior problem*. Its counterpart is the so-called *interior problem*, in which all the sources are located outside the hologram surface. The problem geometries are illustrated in Fig. 3.2.

NAH allows extrapolation of the radiated sound field from measurement of the surrounding fluid response, i.e. sound pressure or particle velocity. It will be shown that the physical principle of Fourier transform-based NAH can be used to extrapolate continuous structural bending wave fields from structural response measurements as well. As will be seen, the application of Fourier transform-based wave field extrapolation in the structure-borne sound domain inherits significant limitations due to the fundamental requirements discussed above.

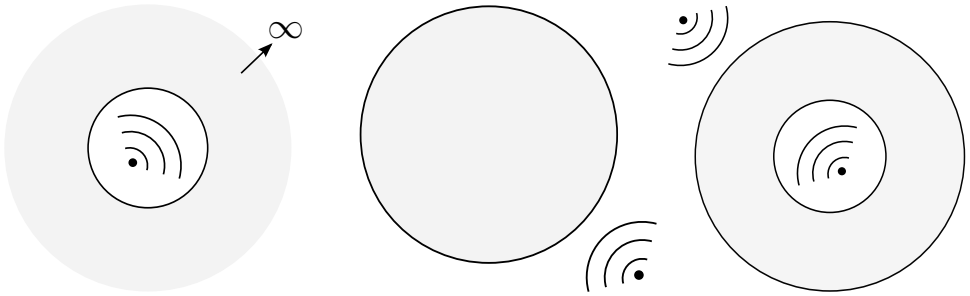

(a) exterior problem **(b)** interior problem **(c)** combined problem

Figure 3.2: General types of boundary value problems.

3.2 Formulation of the plate velocity

In the most general way, holography is the projection of a wave field. Any such projection obviously requires an exact understanding of how waves propagate in a certain medium. A suitable formulation for wave propagation is needed. Considering a structure-borne sound scenario, it is therefore necessary to specify the structural medium of interest as well as the excitation and response under consideration. In this section, the bending motion of a thin, homogenous and isotropic plate[2] of infinite extent, excited by point forces normal to the surface, shall be considered. The according response to a single point excitation in the frequency domain is well known to be radially symmetric. It is described by a combination of Bessel- and Neumann functions, called Hankel functions, of zero order [42]. As discussed in Section 3.1, if wave field extrapolation in the sense of classic NAH is intended, wave propagation needs to be described via a whole set of eigenfunctions. The holographic procedure for the radial propagation of a bending wave field resulting from multiple point forces will therefore require an expanded formulation of Hankel functions in n orders.

[2]Both homogenity and isotropy are required by the methods considered in this thesis. Although they are different characteristics of a structure, the subsequent discussion will only emphasize the former. Referring to a "homogenous plate" shall imply that it is isotropic as well.

As a starting point, the general equation of motion for the normal displacement of a thin homogeneous plate is considered [43]:

$$\frac{B'}{m''}\nabla^2\nabla^2 u(x,y,t) + \frac{\partial^2 u(x,y,t)}{\partial t^2} = 0, \tag{3.2.1}$$

where ∇^2 is the Laplacian operator, u is the normal displacement, B' is the bending stiffness and m'' is the mass per unit area of the plate. Taking the temporal Fourier transform, see Appendix A.4, of Eq. (3.2.1) yields

$$\frac{B'}{m''}\nabla^2\nabla^2 u(x,y,\omega) - \omega^2 u(x,y,\omega) = 0. \tag{3.2.2}$$

By introducing the bending wavenumber k_B through the relation

$$k_B^4 = \frac{m''\omega^2}{B'}, \tag{3.2.3}$$

the equation can be written as

$$\nabla^2\nabla^2 u(x,y,\omega) - k_B^4 u(x,y,\omega) = 0. \tag{3.2.4}$$

Since velocity, the time derivative of displacement, is often preferred over displacement in the analysis of structure-borne sound problems, it is reasonable to formulate the equation of motion accordingly as

$$\nabla^2\nabla^2 v(x,y,\omega) - k_B^4 v(x,y,\omega) = 0, \tag{3.2.5}$$

where v is the normal velocity amplitude.

The fourth order differential equation can be replaced by a set of second order equations

$$\nabla^2 v_1(x,y,\omega) + k_B^2 v_1(x,y,\omega) = 0, \tag{3.2.6}$$

$$\nabla^2 v_2(x,y,\omega) - k_B^2 v_2(x,y,\omega) = 0, \tag{3.2.7}$$

where $v_1(x,y,\omega)$ and $v_2(x,y,\omega)$ constitute components of velocity $v(x,y,\omega)$. The first of the two equations is known as Helmholtz equation, the wave equation for non-dispersive media. Solutions to both equations can be obtained by the method of separation of variables. In general, the method presumes that the solution of a partial differential equation in n variables is a product of n ordinary differential equations, each being equal to a constant. Because of the requirement to match analytical eigenfunctions with a level hologram geometry that leaves one coordinate fixed, as discussed in Section 3.1, it comes natural to look for solutions based on a polar coordinate system. These solutions are

$$v_1(r,\varphi,\omega) = R_1(r,\omega)\Phi_1(\varphi,\omega), \tag{3.2.8}$$

$$v_2(r,\varphi,\omega) = R_2(r,\omega)\Phi_2(\varphi,\omega). \tag{3.2.9}$$

By inserting Eq. (3.2.8) into Eq. (3.2.6) and using the Laplacian operator in polar coordinates

$$\nabla^2 = \frac{\partial^2}{\partial r^2} + \frac{1}{r}\frac{\partial}{\partial r} + \frac{1}{r^2}\frac{\partial^2}{\partial \varphi^2}, \tag{3.2.10}$$

Eq. (3.2.6) becomes[3]

$$\Phi_1 \frac{\mathrm{d}^2 R_1}{\mathrm{d}r^2} + \frac{\Phi_1}{r}\frac{\mathrm{d}R_1}{\mathrm{d}r} + \frac{R_1}{r^2}\frac{\mathrm{d}^2\Phi_1}{\mathrm{d}^2\varphi} + k_B^2 R_1 \Phi_1 = 0. \tag{3.2.11}$$

The arguments of the functions have been omitted for compactness, as will be done in the following steps. Division by $R_1\Phi_1/r^2$ yields

$$\frac{r^2}{R_1}\left(\frac{\mathrm{d}^2 R_1}{\mathrm{d}r^2} + \frac{1}{r}\frac{\mathrm{d}R_1}{\mathrm{d}r}\right) + \frac{1}{\Phi_1}\frac{\mathrm{d}^2\Phi_1}{\mathrm{d}^2\varphi} + k_B^2 r^2 = 0, \tag{3.2.12}$$

or, if sorted by variables,

$$\frac{r^2}{R_1}\left(\frac{\mathrm{d}^2 R_1}{\mathrm{d}r^2} + \frac{1}{r}\frac{\mathrm{d}R_1}{\mathrm{d}r}\right) + k_B^2 r^2 = -\frac{1}{\Phi_1}\frac{\mathrm{d}^2\Phi_1}{\mathrm{d}^2\varphi}. \tag{3.2.13}$$

It is now apparent that the left hand side of Eq. (3.2.13) depends on r alone, whereas the right hand side only depends on φ. Thus, both sides must be equal to a constant, called the *separation constant* [44]. Since the solution must be periodic in φ, the constant is chosen to be n^2 and the right hand side of Eq. (3.2.13) becomes

$$-\frac{1}{\Phi_1}\frac{\mathrm{d}^2\Phi_1}{\mathrm{d}^2\varphi} = n^2, \tag{3.2.14}$$

resulting in an ordinary second order differential equation

$$\frac{\mathrm{d}^2\Phi_1}{\mathrm{d}^2\varphi} + n^2\Phi_1 = 0. \tag{3.2.15}$$

For the left hand side, consequently, it is obtained:

$$\frac{\mathrm{d}^2 R_1}{\mathrm{d}r^2} + \frac{1}{r}\frac{\mathrm{d}R_1}{\mathrm{d}r} + \left(k_B^2 - \frac{n^2}{r^2}\right) R_1 = 0. \tag{3.2.16}$$

Proceeding in the same manner for Eq. (3.2.7), insertion of (3.2.9) into Eq. (3.2.7) yields

$$\frac{\mathrm{d}^2\Phi_2}{\mathrm{d}^2\varphi} + n^2\Phi_2 = 0 \tag{3.2.17}$$

and

$$\frac{\mathrm{d}^2 R_2}{\mathrm{d}r^2} + \frac{1}{r}\frac{\mathrm{d}R_2}{\mathrm{d}r} - \left(k_B^2 + \frac{n^2}{r^2}\right) R_2 = 0. \tag{3.2.18}$$

[3] Because R and Φ represent functions of one variable only, the differential equation is written by means of the total differential d.

Equation (3.2.15) and Eq. (3.2.17) represent the so-called harmonic oscillator equation, whose general elementary solution is respectively given by

$$\Phi_{1,n}(\varphi) = \alpha_n e^{jn\varphi} + \gamma_n e^{-jn\varphi}, \tag{3.2.19}$$

$$\Phi_{2,n}(\varphi) = \beta_n e^{jn\varphi} + \delta_n e^{-jn\varphi}, \tag{3.2.20}$$

where α_n, β_n, γ_n and δ_n are arbitrary coefficients.

Equation (3.2.16) and Eq. (3.2.18) are forms of Bessel's equation of order n. For integer n they were shown to have independent solutions in the form of so-called Bessel functions of the first and second kind $J_n(z)$ and $Y_n(z)$. The latter is also known as Neumann- or Weber function. For a propagating wave solution it is required to use linear combinations of the two [45], known in general as Hankel functions of the first and second kind

$$H_n^{(1)}(z) = J_n(z) + jY_n(z), \tag{3.2.21}$$

$$H_n^{(2)}(z) = J_n(z) - jY_n(z). \tag{3.2.22}$$

General elementary solutions for the nth order of Eq. (3.2.16) and Eq. (3.2.18) are given by

$$R_{1,n}(r,\omega) = a_n H_n^{(2)}(k_B r) + c_n H_n^{(1)}(k_B r), \tag{3.2.23}$$

$$R_{2,n}(r,\omega) = b_n H_n^{(2)}(-jk_B r) + d_n H_n^{(1)}(-jk_B r), \tag{3.2.24}$$

where a_n, b_n, c_n and d_n are arbitrary complex coefficients.

Using the time dependence $e^{j\omega t}$, the Hankel function of the first kind $H_n^{(1)}(k_B r)$ represents an incoming wave, whereas the Hankel function of the second kind $H_n^{(2)}(k_B r)$ represents an outgoing wave. This can be seen by employing Sommerfeld's radiation condition, which states that an outgoing radial wave must originate from a source, not from a sink of energy [46]. The imaginary arguments in Eq. (3.2.24) lead to exponentially decaying terms, generally referred to as *evanescent waves*. They do affect the immediate area around their origin, which in this context is referred to as *near-field region*. Their significance for the problem considered in this thesis is discussed in Section 3.7.

A general elementary solution to Eq. (3.2.5) is ultimately given by the superposition of the solutions

$$\begin{aligned} v_{12,n}(r,\varphi,\omega) =& R_1(r)\Phi_1(\varphi) + R_2(r)\Phi_2(\varphi) \\ =& \left\{ a_n H_n^{(2)}(k_B r) + c_n H_n^{(1)}(k_B r) \right\} \left(\alpha_n e^{jn\varphi} + \gamma_n e^{-jn\varphi} \right) \\ &+ \left\{ b_n H_n^{(2)}(-jk_B r) + d_n H_n^{(1)}(-jk_B r) \right\} \left(\beta_n e^{jn\varphi} + \delta_n e^{-jn\varphi} \right). \end{aligned} \tag{3.2.25}$$

The mathematical solution apparently provides terms for incoming and outgoing wave propagation. Considering a plate of infinite extent, it is evident that only

outgoing wave propagation is possible. In order to obtain a physically comprehensible solution, the terms corresponding to incoming wave propagation have to be discarded. The elementary solution consequently simplifies to

$$v_{12,n}(r,\varphi,\omega) = \\ a_n H_n^{(2)}(k_B r)\left(\alpha_n e^{jn\varphi} + \gamma_n e^{-jn\varphi}\right) + b_n H_n^{(2)}(-jk_B r)\left(\beta_n e^{jn\varphi} + \delta_n e^{-jn\varphi}\right). \tag{3.2.26}$$

Due to the linearity of the wave equation, a complete general solution is obtained by linear superposition of all possible solutions:

$$\begin{aligned} v(r,\varphi,\omega) &= \sum_{n=0}^{\infty} v_{12,n}(r,\varphi,\omega) \\ &= \sum_{n=0}^{\infty}\left\{a_n\alpha_n H_n^{(2)}(k_B r) + b_n\beta_n H_n^{(2)}(-jk_B r)\right\} e^{jn\varphi} \\ &\quad + \sum_{n=0}^{\infty}\left\{a_n\gamma_n H_n^{(2)}(k_B r) + b_n\delta_n H_n^{(2)}(-jk_B r)\right\} e^{-jn\varphi} \\ &= \sum_{n=-\infty}^{0}\left\{a_n\alpha_n^* H_n^{(2)}(k_B r) + b_n\beta_n^* H_n^{(2)}(-jk_B r)\right\} e^{-jn\varphi} \\ &\quad + \sum_{n=0}^{\infty}\left\{a_n\gamma_n H_n^{(2)}(k_B r) + b_n\delta_n H_n^{(2)}(-jk_B r)\right\} e^{-jn\varphi}, \end{aligned} \tag{3.2.27}$$

in which the arbitrary coefficients α_n^* and β_n^* shall replace α_n and β_n for the sake of generality. The sums in Eq. (3.2.27) can be combined to form a single sum over all negative and positive values of n. It is noted that the sign in the exponential term is chosen in order to have consistency in the chosen conventions for Fourier analysis, given in Appendix A. Replacing the coefficients in Eq. (3.2.27) once more ultimately yields a convenient formulation for the radial bending wave propagation in a homogenous infinite plate in terms of the normal velocity in polar coordinates

$$v(r,\varphi,\omega) = \sum_{n=-\infty}^{\infty}\left\{A_n H_n^{(2)}(k_B r) + B_n H_n^{(2)}(-jk_B r)\right\} \mathrm{e}^{-jn\varphi}. \tag{3.2.28}$$

A_n and B_n are arbitrary complex coefficients. Knowledge of the wave field is therefore equivalent to knowledge of these expansion coefficients.

A very simple formulation of the infinite plate velocity results from neglecting the influence of the near-field:

$$v(r,\varphi,\omega) = \sum_{n=-\infty}^{\infty} A_n H_n^{(2)}(k_B r)\mathrm{e}^{-jn\varphi}. \tag{3.2.29}$$

This expression will be used as an alternative mathematical basis for the reconstruction of the bending wave field in an infinite plate in sections 5.6.3 and 6.1.2.

The derived Eqs. (3.2.28) and (3.2.29) constitute a Fourier series, respectively. If the utilized polar coordinate system is interpreted in terms of closed circular contours of radius r, the bending wave field along any such contour is a spatially periodic function, which can be "built" by a sum of discrete series coefficients. As can be understood from Appendix A, where the relation between Fourier series and Fourier transforms is shown, these sums correspond to inverse Fourier transforms in the φ-coordinate. The calculation of the series' coefficient functions, from here on simply referred to as *Fourier components*, can be achieved by performing a forward Fourier transform. The Fourier components are expanded eigenfunctions and essentially represent generalized propagation functions or propagators of order n. They describe the propagation of bending waves in the infinite plate based on the velocity propagator

$$Q_n^{\mathrm{inf}}(r,\omega) = H_n^{(2)}(k_B r) + H_n^{(2)}(-jk_B r). \tag{3.2.30}$$

In matrix form,[4] the velocity propagator is denoted as

$$\mathbf{Q}_n^{\mathrm{inf}}(r,\omega) = \begin{bmatrix} H_n^{(2)}(k_B r) & H_n^{(2)}(-jk_B r) \end{bmatrix}. \tag{3.2.31}$$

How the above relations can be used to extrapolate the continuous bending wave field in an infinite plate is shown in Section 3.3. A physical interpretation of Eq. (3.2.28) and the mathematical operations involved in the holographic procedure is given in Section 3.6.

The difference between wave propagation in infinite and finite plates is the simultaneous occurence of outgoing and incoming waves, caused by reflection at the edges. Since the edges constitute material discontinuities, near-fields can form in their vicinity, depending on the boundary condition. These near-fields can be considered as evanescent waves that point inward. An elementary solution for finite plates has already been presented in the form of Eq. (3.2.25), where both outgoing and incoming propagating waves as well as outgoing and incoming near-fields are accounted for. While it was appropriate to discard the corresponding incoming terms in the infinite case, it is now required to retain them. By proceeding analogously to Eq. (3.2.27), the linear superposition of all elementary solutions yields the complete solution

$$v(r,\varphi,\omega) = \sum_{n=-\infty}^{\infty} \left\{ A_n H_n^{(2)}(k_B r) + B_n H_n^{(2)}(-jk_B r) + C_n H_n^{(1)}(k_B r) + D_n H_n^{(1)}(-jk_B r) \right\} e^{-jn\varphi} \tag{3.2.32}$$

[4] In this thesis, boldface is used to identify matrix notation.

for a finite plate, in which A_n, B_n, C_n and D_n are arbitrary complex coefficients. Eq. (3.2.32) represents a formulation for the radial bending wave propagation in a general homogenous finite plate in terms of the normal velocity. It is noted that, like in Eq. 3.2.28, no specific boundary conditions at the edges are included in this formulation. As in the infinite case, knowledge of the wave field is equivalent to knowledge of the expansion coefficients. The edge boundary conditions should therefore be accounted for once these four coefficients are determined. It is important to note that this is merely an assumption, and not necessarily a justified one. It is known that there are physical boundary conditions for which there are no analytical (or so-called closed form) solutions in the form of a sum of suitable eigenfunctions. Yet, Fourier transform-based NAH relies on the existence of such eigenfunctions. It will therefore be seen that this assumption is not equally warranted in every case. Equation (3.2.32) constitutes a Fourier series in φ as well. Its coefficient functions are eigenfunctions for the finite plate, as long as the mathematical boundary is circular. They can be considered as propagation functions of order n. The corresponding velocity propagator is thus given by

$$Q_n^{\text{fin}}(r,\omega) = H_n^{(2)}(k_B r) + H_n^{(2)}(-jk_B r) + H_n^{(1)}(k_B r) + H_n^{(1)}(-jk_B r), \quad (3.2.33)$$

and in matrix form

$$\mathbf{Q}_n^{\text{fin}}(r,\omega) = \begin{bmatrix} H_n^{(2)}(k_B r) & H_n^{(2)}(-jk_B r) & H_n^{(1)}(k_B r) & H_n^{(1)}(-jk_B r) \end{bmatrix}. \quad (3.2.34)$$

Since the governing Eq. (3.2.5) is derived from thin plate theory, the results presented above are based on the assumption that the effects of shear stiffness and rotational inertia can be neglected. These asumptions are valid as long as sufficiently large wavelengths are considered. As the bending wavelength λ_B starts to equal the sixfold plate thickness h [42],

$$\lambda_B/6 = h, \quad (3.2.35)$$

the resulting error becomes

$$k_B/k_{B,\text{corr}} \approx 0.1, \quad (3.2.36)$$

which is usually deemed tolerable. For wavelengths smaller than that, however, the resulting error becomes significant, which is why some form of correction should be applied. From Mindlin's extended equation of motion, the corrected bending wave phase velocity can be derived [42]

$$c_{B,\text{corr}} \approx c_B\{1 - 4(h/\lambda_B)^2]\}, \quad (3.2.37)$$

which includes the phase velocity found from Kirchhoff's "conventional" plate theory

$$c_B = \frac{\omega}{k_B} = \sqrt[4]{\frac{B'}{m''}}\sqrt{\omega}. \quad (3.2.38)$$

From Eq. (3.2.37), a corresponding corrected bending wavenumber can be derived:

$$k_{B,\mathrm{corr}} \approx \frac{k_B}{1-(k_B h/\pi)^2}. \tag{3.2.39}$$

The corrected bending wavenumber is used in the computations performed for the acrylic plate in Chapter 6.

3.3 Holographic procedure for infinite plates

This section explains how the equations established in Section 3.2 can be used to perform both backward- and forward-propagation of the bending wave field, based on structural response measurements. The procedure constitutes an exterior problem, as depicted in Fig. 3.2a. Formally, backward-propagation is considered in the following, but it is important to note that the procedure for forward-propagation is identical and merely differs by a change of the argument r in a mathematical sense.

Fig. 3.3 illustrates the exterior problem of an infinite plate, excited by point forces arbitrarily aligned along a circular source contour of radius r_S, exhibiting the normal velocity $v(r,\varphi,\omega)$. For now, it shall be assumed that the velocity distribution $v(r_\mathrm{S},\varphi,\omega)$ along the source contour at r_S is of prime interest. The procedure relies on the polar coordinate system, wherefore the extrapolatable area is bounded inward by the circular source contour at r_S. This can be compared to the conformal source surfaces discussed in Section 3.1.

The mathematical procedure can be summarized as

$$\begin{aligned}
v(r_\mathrm{S},\varphi,\omega) &= \mathcal{F}_\varphi^{-1}\left\{ \mathbf{Q}_n^{\mathrm{inf}}(r_\mathrm{S},\omega) \begin{bmatrix} \mathbf{Q}_n^{\mathrm{inf}}(r_1,\omega) \\ \mathbf{Q}_n^{\mathrm{inf}}(r_2,\omega) \end{bmatrix}^{-1} \begin{bmatrix} \mathcal{F}_\varphi\{v(r_1,\varphi,\omega)\} \\ \mathcal{F}_\varphi\{v(r_2,\varphi,\omega)\} \end{bmatrix} \right\} \\
&= \mathcal{F}_\varphi^{-1}\left\{ \mathbf{Q}_n^{\mathrm{inf}}(r_\mathrm{S},\omega) \begin{bmatrix} H_n^{(2)}(k_B r_1) & H_n^{(2)}(-jk_B r_1) \\ H_n^{(2)}(k_B r_2) & H_n^{(2)}(-jk_B r_2) \end{bmatrix}^{-1} \begin{bmatrix} v_n(r_1,\omega) \\ v_n(r_2,\omega) \end{bmatrix} \right\} \\
&= \mathcal{F}_\varphi^{-1}\left\{ \begin{bmatrix} H_n^{(2)}(k_B r_\mathrm{S}) & H_n^{(2)}(-jk_B r_\mathrm{S}) \end{bmatrix} \begin{bmatrix} A_n \\ B_n \end{bmatrix} \right\} \\
&= \mathcal{F}_\varphi^{-1}\left\{ A_n H_n^{(2)}(k_B r_\mathrm{S}) + B_n H_n^{(2)}(-jk_B r_\mathrm{S}) \right\},
\end{aligned} \tag{3.3.1}$$

where $\mathcal{F}_\varphi^{-1}$ and $\mathcal{F}_\varphi$ indicate inverse and forward Fourier transforms in the φ-coordinate. The interpretation is as follows: A part of the wave field is sampled in polar coordinates and decomposed into Fourier components by means of a spatial Fourier transform. This represents a determination of the boundary values in the wavenumber domain. The components are then multiplied by an expanded propagator function, which means that magnitude and phase of the field are shifted

in the wavenumber domain. The field is ultimately reconstructed in the frequency domain by performing an inverse Fourier transform.

By comparison, the mathematical methodology is closely related to that of cylindrical NAH, summarized in Eq. (3.1.3), or NAH in general. The procedure outlined above is therefore termed *Near-Field Structure-Borne Sound Holography*, from here on referred to as NSBSH. Like NAH, NSBSH poses an *inverse* problem by nature. The traits of an inverse problem and the resulting numerical challenges are discussed in Sections 3.9.1 and 3.9.2. Considering the geometry given in Fig. 3.3, the procedure is discussed step-by-step in the following. Five consecutive steps may be differentiated:

1. Obtaining the hologram data, i.e. measurement of the normal velocity distributions $v(r_1, \varphi, \omega)$ and $v(r_2, \varphi, \omega)$ along two circular contour lines;

2. Performing a spatial Fourier transform

$$v_n(r_1, \omega) = \mathcal{F}_\varphi\{v(r_1, \varphi, \omega)\} = \int_{-\pi}^{\pi} v(r_1, \varphi, \omega) \mathrm{e}^{jn\varphi} \, \mathrm{d}\varphi, \tag{3.3.2}$$

$$v_n(r_2, \omega) = \mathcal{F}_\varphi\{v(r_2, \varphi, \omega)\} = \int_{-\pi}^{\pi} v(r_2, \varphi, \omega) \mathrm{e}^{jn\varphi} \, \mathrm{d}\varphi, \tag{3.3.3}$$

   where n represents the index of the Fourier components;

3. Establishing a linear system of equations

$$v_n(r_1, \omega) = A_n H_n^{(2)}(k_B r_1) + B_n H_n^{(2)}(-jk_B r_1), \tag{3.3.4}$$

$$v_n(r_2, \omega) = A_n H_n^{(2)}(k_B r_2) + B_n H_n^{(2)}(-jk_B r_2), \tag{3.3.5}$$

   and solving for the unknown coefficients A_n, B_n;

4. Extrapolating in the wavenumber domain

$$v_n(r_\mathrm{S}, \omega) = A_n H_n^{(2)}(k_B r_\mathrm{S}) + B_n H_n^{(2)}(-jk_B r_\mathrm{S}); \tag{3.3.6}$$

5. Performing an inverse Fourier transform

$$v(r_\mathrm{S}, \varphi, \omega) = \mathcal{F}_\varphi^{-1}\{v_n(r_\mathrm{S}, \omega)\} = \frac{1}{2\pi} \int_{-\infty}^{\infty} v_n(r_\mathrm{S}, \omega) \mathrm{e}^{-jn\varphi} \, \mathrm{d}n. \tag{3.3.7}$$

1. Obtaining the hologram data Eq. (3.2.28) states that two expansion coefficients, A_n and B_n, have to be determined in order to describe radial bending wave propagation by means of the normal plate velocity. In order to obtain the coefficients, two boundary conditions are needed. They are found by measurement of the spatial velocity distribution along two circular contour lines in the near-field

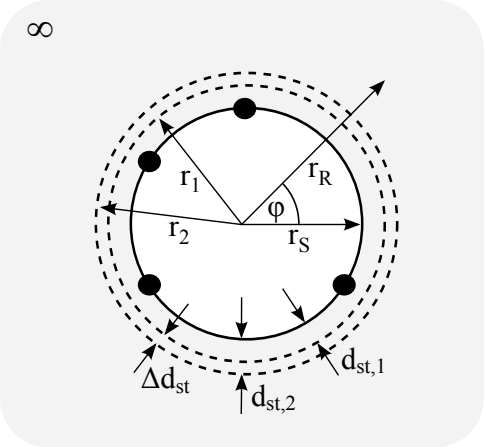

Figure 3.3: Exterior problem geometry for NSBSH on an infinite plate; **- -** hologram contour; **—** source contour; • normal point force; extrapolatable plate area.

of the source, $v(r_1, \varphi, \omega)$ and $v(r_2, \varphi, \omega)$. These distributions are the holograms from which the other images of the wave field can be extrapolated. The distance between hologram contour and source contour is referred to as *standoff distance*. Corresponding to the hologram contour radii r_1 and r_2 there are two standoff distances

$$d_{\mathrm{st},1} = r_1 - r_{\mathrm{S}}, \tag{3.3.8}$$

$$d_{\mathrm{st},2} = r_2 - r_{\mathrm{S}} \tag{3.3.9}$$

which differ by the contour distance

$$\Delta d_{\mathrm{st}} = r_2 - r_1. \tag{3.3.10}$$

As in fluid-borne NAH, a reconstruction at the source requires the hologram data to contain evanescent wave information, wherefore the corresponding measurements have to be taken in the structural near-field region.

Since the amplitude of vibration does not depend on a coordinate normal to the plate surface, bending wave propagation in a thin plate is a function of two dimensions. Therefore, whereas in classic NAH a hologram surface is used to reconstruct a fluid-borne field that is a function of three dimensions, hologram contour lines are used to reconstruct a structure-borne field that is a function of two dimensions. Practically speaking, whereas in NAH the spatial distribution of sound pressure is measured in a single plane or on a cylindrical or spherical surface, in NSBSH the spatial distribution of structural acceleration or velocity is measured along separate circular contour lines.

Measurement has to sample the distribution at a sufficient rate in order to avoid aliasing effects. The intricacy of the distribution along a contour depends on the

smallest occuring wavelength in general but more specifically on the radius of the contour. A substantial discussion of spatial sampling by means of a circular sensor array is not aimed at in this thesis, mostly because spatial signal processing is a complex topic of its own. Further research might benefit the processing performed in Chapters 5 and 6, however, and it stands to reason that in this regard clues might be taken from literature dealing with the recording and reproduction of airborne sound by means of circular microphone arrays, e.g. [47,48]. It is acknowledged that by discounting specific aliasing effects due to the circular measurement aperture, the following consideration is a simplified one. Since these effects will be shifted to higher frequencies if a reasonably high amount of sampling points is used, they shall not be considered specifically in this thesis.

In order to have a simple and approximate criterion for the required number of sampling points, far-field conditions are assumed. The required number of sampling points N_{crit} might then be estimated by the spatial Nyquist criterion that relates the sampling distance Δx and the smallest occuring wavelength

$$\frac{\lambda_{B,\mathrm{min}}}{2} > \Delta x = \frac{2r\pi}{N_{\mathrm{crit}}}. \tag{3.3.11}$$

Depending on the outer radius r to be sampled, it is given by

$$N_{\mathrm{crit}} > \frac{4r\pi}{\lambda_{B,\mathrm{min}}} = 2rk_{B,\mathrm{max}}. \tag{3.3.12}$$

For a contour located in the near-field, however, the relation is not so clear, wherefore the number obtained from Eq. (3.3.12) should preferably be increased by a small amount. Eq. (3.3.12) basically states that contour lines with larger radii require a higher number of sampling points to resolve the smallest wavelength under consideration. It refers to the correct resolution of the propagating bending wave components only. It is not a criterion for evanescent wave resolution, which, as is discussed in Section 3.7, cannot be given as explicitly.

2. Fourier transform As seen in Eqs. (3.3.2) and (3.3.3), both distributions have to be decomposed into Fourier components in order to be used with Eq. (3.2.28). Because the velocity distribution along each hologram contour has to be determined by discrete measurement in practice, the Fourier transforms are carried out by means of discrete Fourier transformation (DFT). For periodic signals such as the spatial velocity distribution along a closed contour, performing a DFT will yield the Fourier components that make up the governing Fourier series, as shown in Appendix A. In this thesis, all practical spatial transforms are performed by using the fast Fourier Transform (FFT)-algorithms provided by MATLAB®.

3. Establishing and solving a linear system of equations Using the Fourier transform of the velocity distributions obtained by measurement, a linear system

of equations can be established, allowing to solve for A_n and B_n. The right hand side of Eq. (3.3.4) and Eq. (3.3.5), respectively, consitutes the coefficient function of the Fourier series in Eq. (3.2.28), i.e. the velocity propagator scaled by the expansion coefficients A_n and B_n. Obviously, the system itself is most basic and can therefore be solved in a straightforward manner. The solutions are given in Appendix C.1.

4. Extrapolation Having determined A_n and B_n, the propagation of waves is determined in the wavenumber domain. The wave field can now be extrapolated without difficulty. Backward-propagation to the wave field at r_S is performed by application of Eq. (3.3.6). The legitimate region for extrapolation is the whole plate area $r > r_\mathrm{S}$ encompassing the sources, as marked in Fig. 3.3. As stated above, forward-propagation can be conducted by exchanging r_S for r_R in Eq. (3.3.6), where $r_\mathrm{R} > r_2$.

5. Inverse Fourier transform Performing the inverse Fourier transform according to Eq. (3.3.7) ultimately yields the velocity along the source contour at r_S in the frequency domain. This represents a summation of the constituing Fourier components, i.e. the scaled velocity propagators of order n that make up the Fourier series derived in Section 3.2. It is understood from Appendix A that performing the inverse Fourier transform is equal to the Fourier series.

Forward-propagation can be conducted analogously. By setting the radius to any desired value $r_\mathrm{R} > r_2$, the velocity distribution in the far-field may be reconstructed. Thus, the continuous bending wave field for $r > r_\mathrm{S}$ can be reconstructed.

An unwelcome side effect of this kind of procedure is the amplification of measurement noise. If backward-propagation toward the sources is attempted from data collected outside of the immediate near-field region, large error seems inevitable in practice. This can be seen from an analysis of the governing equation. Using Eqs. (C.1.1) and (C.1.2), Eq. (3.3.6) can be written as

$$\begin{aligned} v_n(r_\mathrm{S}) =& \frac{H_n^{(2)}(k_B r_\mathrm{S}) \left[v_n(r_2) H_n^{(2)}(-jk_B r_1) - v_n(r_1) H_n^{(2)}(-jk_B r_2) \right]}{H_n^{(2)}(k_B r_2) H_n^{(2)}(-jk_B r_1) - H_n^{(2)}(k_B r_1) H_n^{(2)}(-jk_B r_2)} \\ &+ \left\{ v_n(r_1) - \frac{H_n^{(2)}(k_B r_1) \left[v_n(r_2) H_n^{(2)}(-jk_B r_1) - v_n(r_1) H_n^{(2)}(-jk_B r_2) \right]}{H_n^{(2)}(k_B r_2) H_n^{(2)}(-jk_B r_1) - H_n^{(2)}(k_B r_1) H_n^{(2)}(-jk_B r_2)} \right\} \\ &\cdot \left\{ \frac{H_n^{(2)}(-jk_B r_\mathrm{S})}{H_n^{(2)}(-jk_B r_1)} \right\}. \end{aligned} \tag{3.3.13}$$

Eq. (3.3.13) represents an explicit formulation for backward-propagation from the wave field at r_1 and r_2 to the wave field at r_S. It is a rather cryptic formulation,

but its behavior can be made more transparent by using asypmtotic expressions for the Hankel functions of large argument [49]

$$H_n^{(2)}(z) \to \sqrt{2/\pi z}\mathrm{e}^{-jz+j(\pi n/2+\pi/4)}, \quad |z| \gg n. \tag{3.3.14}$$

By using Eq. (3.3.14) and applying standard arithmetic operations, Eq. (3.3.13) becomes

$$\begin{aligned} v_n(r_\mathrm{S}) \approx & \frac{\sqrt{\frac{r_2}{r_\mathrm{S}}}v_n(r_2)\mathrm{e}^{-k_B r_1} - \sqrt{\frac{r_1}{r_\mathrm{S}}}v_n(r_1)\mathrm{e}^{-k_B r_2}}{\mathrm{e}^{-k_B(r_1+jr_2)} - \mathrm{e}^{-k_B(r_2+jr_1)}}\mathrm{e}^{-jk_B r_\mathrm{S}} \\ & + \left\{ v_n(r_1) - \frac{\mathrm{e}^{-k_B(r_1+jr_1)} - \mathrm{e}^{-k_B(r_2+jr_1)}}{v_n(r_2)\mathrm{e}^{-k_B(r_1+jr_2)} - v_n(r_1)\mathrm{e}^{-k_B(r_2+jr_1)}} \right\} \sqrt{\frac{r_1}{r_\mathrm{S}}}\mathrm{e}^{k_B(r_1-r_\mathrm{S})}. \end{aligned} \tag{3.3.15}$$

The first summand of Eq. (3.3.15) and Eq. (3.3.13) is of propagating wave character, while the second summand is an exponential function whose magnitude quickly becomes dominant as the ratio r_1/r_S and therefore the difference $r_1 - r_\mathrm{S}$ increases. Backward-propagation is thus characterized by a strong exponential increase of the Fourier components' magnitude. As measurements are made further away from the source, the required increase becomes more drastic. This is especially true for high wavenumbers and, although not directly shown by Eq. (3.3.15), Fourier components of high order n. This behavior is legitimate as long as the input data resolves the evanescent waves with sufficient accuracy, which can be assumed as long as the two hologram contours are located close enough to the source and at a reasonable distance to each other, depending on the dynamic range of the measurement system. On the other hand, if the resolution is inaccurate, even small errors will be greatly amplified. In the presence of measurement noise, backward-propagation is therefore likely to yield erratically blown-up results.

If forward-propagation is attempted, reconstruction does not need to backtrack such evanescence. Because there is no drastic exponential increase of measurement values, the effect of noise is not expected to be as destructive.

3.4 Holographic procedure for finite plates

In the case of a finite plate, the problem of radial wave field extrapolation is a combination of exterior and interior problem. Although Eq. (3.2.32) describes a field of waves of opposing direction, it is only valid in a region where said field is free of sources. Considering the polar coordinate system that was utilized to obtain the solutions to the governing differential equation, the valid region therefore has to be annular. This is shown in Fig. 3.4 which illustrates the problem of a finite plate, excited by arbitrarily positioned normal point forces, exhibiting the normal velocity $v(r, \varphi)$. In analogy to Section 3.3, the mathematical process

of reconstruction is summarized as

$$v(r_\mathrm{R},\varphi) = \mathcal{F}_\varphi^{-1}\left\{ \mathbf{Q}_n^\mathrm{fin}(r_\mathrm{R},\omega) \begin{bmatrix} \mathbf{Q}_n^\mathrm{fin}(r_1,\omega) \\ \mathbf{Q}_n^\mathrm{fin}(r_2,\omega) \\ \mathbf{Q}_n^\mathrm{fin}(r_3,\omega) \\ \mathbf{Q}_n^\mathrm{fin}(r_4,\omega) \end{bmatrix}^{-1} \begin{bmatrix} \mathcal{F}_\varphi\{v(r_1,\varphi,\omega)\} \\ \mathcal{F}_\varphi\{v(r_2,\varphi,\omega)\} \\ \mathcal{F}_\varphi\{v(r_3,\varphi,\omega)\} \\ \mathcal{F}_\varphi\{v(r_4,\varphi,\omega)\} \end{bmatrix} \right\}. \tag{3.4.1}$$

1. Obtaining the normal velocity distributions $v(r_1,\varphi), v(r_2,\varphi), v(r_3,\varphi)$ and $v(r_4,\varphi)$ along the hologram contour lines;

2. Performing a spatial Fourier transform

$$\mathcal{F}_\varphi\{v(r_1,\varphi,\omega)\} \to v_n(r_1,\omega), \tag{3.4.2}$$
$$\mathcal{F}_\varphi\{v(r_2,\varphi,\omega)\} \to v_n(r_2,\omega), \tag{3.4.3}$$
$$\mathcal{F}_\varphi\{v(r_3,\varphi,\omega)\} \to v_n(r_3,\omega), \tag{3.4.4}$$
$$\mathcal{F}_\varphi\{v(r_4,\varphi,\omega)\} \to v_n(r_4,\omega); \tag{3.4.5}$$

3. Establishing a linear system of equations

$$v_n(r_1,\omega) = A_n H_n^{(2)}(k_B r_1) + B_n H_n^{(2)}(-jk_B r_1) + C_n H_n^{(1)}(k_B r_1) + D_n H_n^{(1)}(-jk_B r_1), \tag{3.4.6}$$

$$v_n(r_2,\omega) = A_n H_n^{(2)}(k_B r_2) + B_n H_n^{(2)}(-jk_B r_2) + C_n H_n^{(1)}(k_B r_2) + D_n H_n^{(1)}(-jk_B r_2), \tag{3.4.7}$$

$$v_n(r_3,\omega) = A_n H_n^{(2)}(k_B r_3) + B_n H_n^{(2)}(-jk_B r_3) + C_n H_n^{(1)}(k_B r_3) + D_n H_n^{(1)}(-jk_B r_3), \tag{3.4.8}$$

$$v_n(r_4,\omega) = A_n H_n^{(2)}(k_B r_4) + B_n H_n^{(2)}(-jk_B r_4) + C_n H_n^{(1)}(k_B r_4) + D_n H_n^{(1)}(-jk_B r_4), \tag{3.4.9}$$

   and solving for the unknown coefficients A_n, B_n, C_n, D_n;

4. Extrapolating in the wavenumber domain

$$v_n(r_\mathrm{R},\omega) = A_n H_n^{(2)}(k_B r_\mathrm{R}) + B_n H_n^{(2)}(-jk_B r_\mathrm{R}) + C_n H_n^{(1)}(k_B r_\mathrm{R}) + D_n H_n^{(1)}(-jk_B r_\mathrm{R}); \tag{3.4.10}$$

5. Performing an inverse Fourier transform

$$\mathcal{F}_\varphi^{-1}\{v_n(r_\mathrm{R},\omega)\} \to v(r_\mathrm{R},\varphi,\omega). \tag{3.4.11}$$

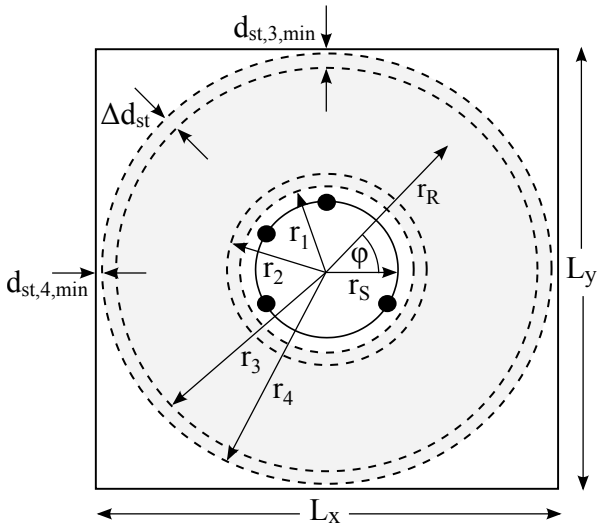

Figure 3.4: Annular problem geometry for NSBSH on a finite plate; **- -** hologram contour; • normal point force; extrapolatable plate area; — plate boundary with arbitrary geometry and boundary condition.

In order to apply numerical stabilization techniques such as regularization in step 2, the system of equations has to be put in matrix form

$$\begin{bmatrix} v_n(r_1,\omega) \\ v_n(r_2,\omega) \\ v_n(r_3,\omega) \\ v_n(r_4,\omega) \end{bmatrix} = \begin{bmatrix} \mathbf{Q}_n^{\text{fin}}(r_1,\omega) \\ \mathbf{Q}_n^{\text{fin}}(r_2,\omega) \\ \mathbf{Q}_n^{\text{fin}}(r_3,\omega) \\ \mathbf{Q}_n^{\text{fin}}(r_4,\omega) \end{bmatrix} \begin{bmatrix} A_n \\ B_n \\ C_n \\ D_n \end{bmatrix}. \tag{3.4.12}$$

The system is small enough to be solved by hand, however. The solutions found by using Gaussian elimination are given in Appendix C.2.

Although mathematically the procedure is identical to the procedure for infinite plates, it is different in a physical sense. The wave field is not propagated "backward" or "forward" anymore because now there is more than one direction in which the waves do propagate. Applying Eq. (3.4.1) rather means to propagate "inward" or "outward" toward either boundary given by the hologram contours. Ultimately, the difference between both procedures is of practical nature. In comparison to the finite case, four contour lines are necessary to obtain the required hologram data, corresponding to the four unknown coefficients in Eq. (3.2.32). Identically to the infinite plate scenario, the standoff distances $d_{\text{st},1}$ and $d_{\text{st},2}$ are defined according to Eqs. (3.3.8) and (3.3.9). Additionally,

$$d_{\text{st,3,min}} = L_{x,y}/2 - r_3 \tag{3.4.13}$$

and

$$d_{\text{st,4,min}} = L_{x,y}/2 - r_4 \tag{3.4.14}$$

are respectively defined as the the minimum distances between outer hologram contour and plate border.

Taking into account that larger contours require more sampling points, the amount of measurement data is more than doubled. Secondly, as can be seen in Fig. 3.4, the wave field of a finite plate can only be reconstructed in the annular region $r_1 \leq r_\mathrm{R} \leq r_4$ confined by the hologram contour lines. As stated above, Eq. (3.2.32) is only valid in a source-free region of the wave field. As a consequence, the region confined by the hologram contour lines cannot be extended inward beyond the position of the sources. In outward direction, it cannot be extended beyond the dimensions of the plate, obviously. It is thus not possible to reconstruct the field either in the center between the excitation sources or toward the corners of the plate. This might not be too big of a limitation if a circular plate is excited at the center, but it is a significant one if rectangular plates with higher aspect ratios are considered. The geometry of the plate itself can be arbitrary and does not need to be rectangular or symmetric.

3.5 Remarks on semantics

It is important to mention that the holographic procedure presented in Section 3.3 and Section 3.4 does not necessitate near-field information if only the far-field is to be reconstructed. It is in fact possible to reconstruct the continuous far-field from hologram data that includes no near-field information at all. *Near-Field Structure-Borne Sound Holography* would be a misleading term in such instances. In that sense, the ramifications of the near-field in NSBSH are different from those in NAH. In NAH, near-field information is crucial in order to resolve sources that are closer than the distance of one wavelength. NSBSH, as presented in this thesis, does not allow the clear identification of two point forces because the surrounding field cannot be reconstructed wholly. The role of the near-field in NSBSH, apart from being a physically different effect, is therefore different from that in NAH. It is "merely" required in order to reconstruct the correct response magnitude of the field.

In the infinite case, a certain terminology was used to highlight the analogies between NAH and the procedure presented in this thesis. If waves do only propagate outward it is clear that backward-propagation describes the act of backtracking the outgoing wave field toward the source. In the finite case, where waves are reflected back and forth, the prefixes "backward" and "forward" lose their original meaning, as one rather propagates "inward" or "outward".

3.6 Physical interpretation

Equation. (3.2.28) describes the constitution of a wave field in polar coordinates in a very general manner. The bending wave field of a homogenous infinite plate

can be described as a Fourier series whose components are generalized propagation functions. For comparison, the wave field of such a plate in response to a single point excitation at the origin of the coordinate system can be described by the propagation function [42]

$$v(r,\omega) = v_0 \left\{ H_0^{(2)}(k_B r) - H_0^{(2)}(-jk_B r) \right\}, \tag{3.6.1}$$

in which v_0 may be any amplitude of normal velocity. The corresponding wave field is rotationally symmetric, as depicted in Fig. 3.5a. The amplitude along the path of a circular section at any given radius is constant. In the time domain, the perturbances in the medium are analogous to those that are observed when a stone is dropped in quiescent water. Circular wavefronts propagate outward and essentially become plane wavefronts at a large distance. In this sense, the wave field in Fig. 3.5a only consists of the zero order of Eq. (3.2.28) because at a fixed radius all the particles move up and down in phase.

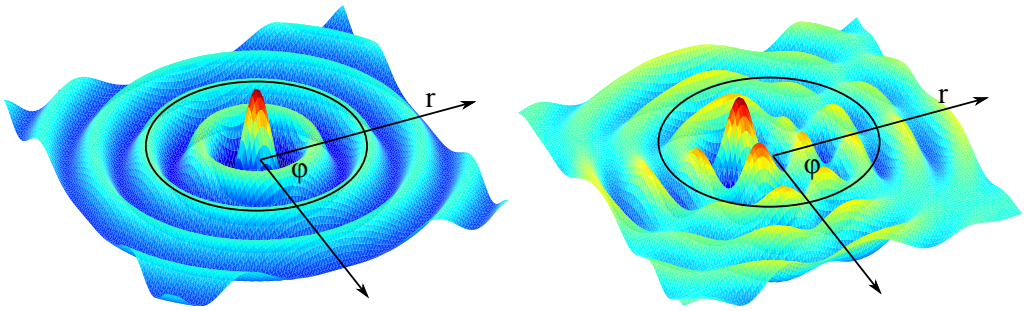

(a) excitation by a single force **(b)** excitation by a set of forces

Figure 3.5: Infinite plate response due to normal forces.

Imagining a set of arbitrary point forces randomly positioned around the origin, it is understood that the resulting wave field is no longer rotationally symmetric. The amplitude along the path of a circular section at any given radius will have an arbitrary spatial distribution, as depicted in Fig. 3.5b. According to Eq. (3.2.28), this distribution can be exactly described if an infinite number of sinusoidal distributions $e^{-jn\varphi}$ of different amplitude are summed up.[5] Hereby, n indicates the number of "wavelengths" that make up each distribution, as is visualized in Fig. 3.6. It is a direct application of the Fourier series theorem in the spatial domain, in which spatial data is considered as a spectrum of discrete Fourier components. Using such a series expansion approach is quite common for structural vibration problems, e.g. in the analysis of structure-borne sound transmission [50, 51].

The procedure can thus be interpreted as follows: Through the forward Fourier transform, the arbitrary spatial distribution along a circular section of the bending

[5] In the field of antenna arrays, these terms would be known as "phase modes" [47], for example.

wave field is broken down to a set of basic sinusoidal distributions. Given a few discrete sampling points, they are better imagined as a series of points in normal vibration, with the displacements having a certain phase relation. From the boundary conditions it is possible to calculate propagation functions that determine how each of these sinusoids must change in radial direction. The boundary conditions themselves are given by the spatial distribution of the normal velocity along the hologram contour lines. Radial wave field extrapolation scales each sinusoidal distribution in magnitude and phase accordingly, as indicated in the right half of Fig. 3.6. The inverse Fourier transform finally reconstructs the actual spatial distribution along a circular contour at any desired radius by summing up the corresponding set of scaled basic spatial distributions.

This interpretation appears to be less illustrative in the finite case, but it applies as well. The same set of basic spatial distributions is summed up, but their scaling is now informed by both inner and outer boundary conditions at the same time.

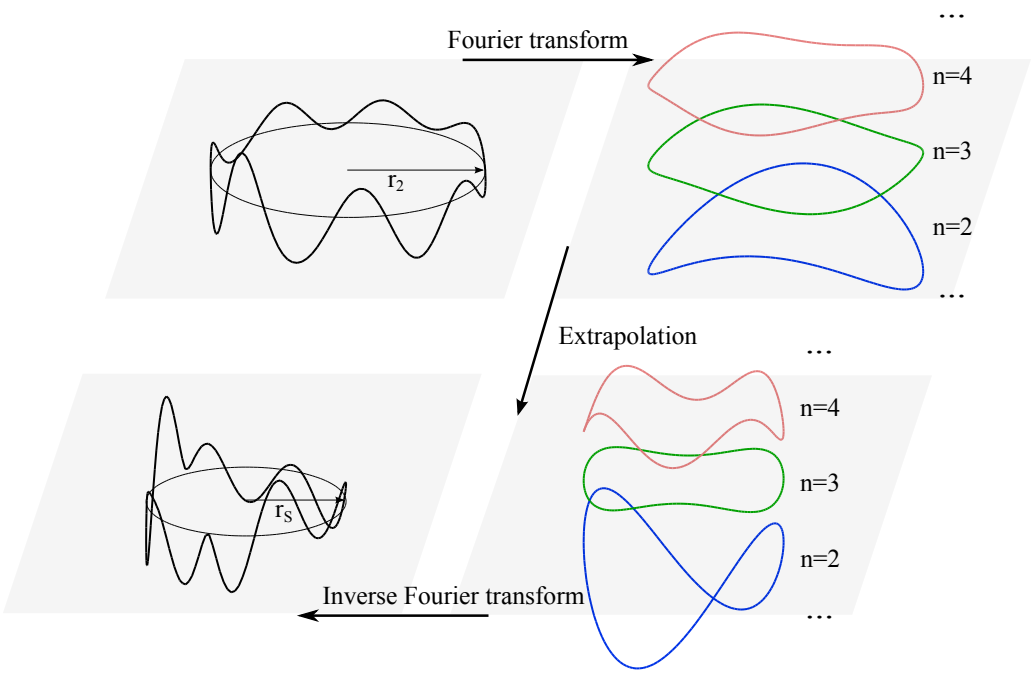

Figure 3.6: Schematic illustration of the holographic procedure for backward-propagation.

3.7 Definition of the near-field region

The bending wave field of a plate consists of propagating and exponentially decaying wave components. The latter form at the points of excitation and at structural discontinuities, namely the plate boundaries, and are referred to as evanescent waves. Although they decay within short distance, they do affect the immediate area around their origin, which in this context is referred to as *near-field region*. It is a structural region that is to be differentiated from the radiated near-field regions of a vibrating surface, i.e. the hydrodynamic and the geometric near-field [52]. Therefore, whenever this thesis utilizes considerations regarding the near-field in NAH, it is acknowledged that fluid-borne near-fields are physically different effects. This thesis only considers pure structural bending wave near-fields, which may be further differentiated from near-field effects that occur when the excitation is a distributed force or moment or when excitations or discontinuities of thick structures are considered [53]. The corresponding mathematical terms pose an inconvenience in the analysis of structure-borne sound problems because they complicate the governing differential equations. In order to find solutions, they are often rightfully discarded when far-field conditions sufficiently remote from discontinuities can be assumed. The problem considered in this thesis, however, is the reconstruction of the wave field from measurements close to structural discontinuities, wherefore evanescent wave components cannot be discarded a priori on the same basis. Moreover, if the aim is to reconstruct the wave field at the source where evanescent waves are suspected to prevail, it is comprehensible that the information of these wave components has to be incorporated. Practically, this means that the hologram contour lines have to be located within the near-field region of the wave field. Only if this condition is met, will use of the formulae presented in Section 3.3 produce accurate results.

This raises the question about the spatial extent of the near-field region in practice and its definition in general. How close to the source does one have to get for measurement? The constituents of the analytical solution for a point-driven infinite plate, given in Eq. (3.6.1), may therefore be considered. The solution is not precisely separated into pure propagating and evanescent components because the Hankel function of real argument shows near-field behavior as well. However, the term that involves the imaginary argument is purely evanescent, wherefore the level difference

$$\Delta L_H = 10 \log \left| \frac{H_0^{(2)}(-jk_B r)}{H_0^{(2)}(k_B r)} \right|^2 \tag{3.7.1}$$

may be used to analyze the relative decay of the evanescent wave in a theoretical wave-based context. From Fig. 3.7, where ΔL_H is plotted over the dimensionless distance $r/\lambda_B = k_B r/2\pi$, it is observed that the evanescent wave is diminished by almost 30 dB at a distance $r = \lambda_B/2$ and by almost 60 dB at a distance $r = \lambda_B$. It is noted that almost the same decay is found when the level difference is calculated

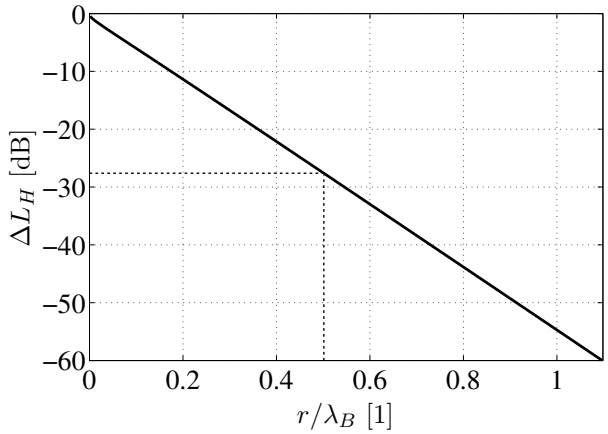

Figure 3.7: Relative decay of the evanescent bending wave.

through exponential functions $e^{jk_B r}$ and $e^{-k_B r}$ that are used to describe propagating and evanescent bending waves, respectively, in one-dimensional structures.

The condition most often found in literature is that evanescent waves can be neglected if $k_B r \gg 1$, which equals $r/\lambda_B \gg 1/(2\pi)$. It can be estimated that in practice the effect of the near-field region will be negligible at distances greater than $r = \lambda_B/2$. The near-field region might also be considered in terms of structure-borne power flow. In the immediate area surrounding a vibration source there is a significant amount of reactive power fluctuation. A near-field limit might therefore be chosen where the reactive power fluctuation is less by a significant amount than the corresponding active power [54]. This approach is not without difficulty. It is known that in isolation, propagating waves transmit energy while evanescent waves do not. On the other hand, if incoming and outgoing waves are present at once, evanescent waves can interact to transmit energy, as has been shown for thin beams [55] and plates [56]. Given a set of excitation forces in close proximity, this interaction should be accounted for. In early research on power flow, it was deduced that the near-field practically vanishes half a wavelength away from the boundary of a semi-infinite beam and approximately one wavelength away from the boundary of a finite beam in the presence of a standing wave [57].

In general, researchers often assume evanescent waves to vanish at a distance of about half a wavelength from stuctural discontinuities, e.g. [53, 58], notably if active control of bending vibration is attempted [59, 60]. For the purpose of this thesis, this limit shall be used as point of reference. It is not a strict criterion, however. In practice, the successful resolution of the decaying near-field depends greatly on the dynamic range of the measurement system. The presence of noise or the use of low sensitivity accelerometers may therefore require measurement closer to the source than $\lambda_B/2$, wherefore $\lambda_B/4$ might be a more suitable point of reference in practice. For a conclusion in this regard it is referred to Chapter 6.

3.8 Remarks on the geometrical limitation

It is evident that the polar coordinate system that is used to describe the propagation of bending wave components is not best suited for a medium that constitutes a rectangular plate. As a consequence, it would be desirable to formulate the procedure in Cartesian coordinates, since these are conformal to the geometry of rectangular plates. However, recalling the nature of Fourier-transform-based NAH, to which NSBSH is analogous to, it becomes clear that this is not possible. As discussed in Section 3.1 and as can be understood from Eqs. (3.1.1) and (3.1.3), extrapolation needs to be performed in a coordinate system that allows the following: The measured hologram needs to form a surface that is normal to the general direction of the propagating waves and the surface must be constant in one separable coordinate along which the field is to be projected. In other words, the section of the wave field that is used as a hologram must not be a function of the projection-coordinate. For the two-dimensional problem of bending wave propagation in a thin plate, these requirements are only met in polar coordinates where the Hankel functions represent eigenfunctions independent of the coordinate φ. In Cartesian coordinates, an encompassing hologram would be a function of both coordinates x and y, which is not permitted.

Despite the mathematical analogy to NAH, NSBSH is a problem of its own in many ways. Apart from a different practical measurement procedure, the description of the wave field, the field variables and the boundary conditions are different since elastic wave propagation is considered. Section 3.9 shows that the required data processing can be handled with the same basic tools used in NAH, however.

3.9 Stabilization techniques

NSBSH is an example of what in mathematical physics is referred to as an *inverse* problem, which is to be differentiated from a direct problem. As is noted by Kabanikhin in a survey paper on the topic [61], there is no strict definition for inverse problems. Following Keller [62], who declares two problems inverse to each other if the formulation of one problem involves the other, he states that the inverse problem seeks to find unknown functions that include some of the functions occuring in the formulation of the direct problem. For stationary processes, direct problems usually seek to determine a response function that describes a physical field at any point of a given spatial domain, based on knowledge of the domain, the carrier medium, the source function and the boundary conditions. Because in NSBSH the sought-after propagation functions require the determination of boundary conditions through similar propagation functions for the direct problem, it is an inverse problem according to the above definition.

Inverse problems are very often *ill-posed* problems. The concept of well-posedness and ill-posedness goes back to Hadamard [63], who defines a problem as well-posed

if it has a solution that is unique and is a continuous function of the input data. A problem is therefore ill-posed if it has more than one solution or none at all, or if small errors in the data lead to large errors in the solutions. In the latter case, the solution will be very sensitive to perturbances of either the input data or the matrix that represents the system of equations, which is called an *ill-conditioned* system. As seen in Section 3.7, ill-conditioning unfortunately applies to the mathematical models used in NSBSH. It is therefore necessary to apply some form of data conditioning or enhanced processing in order to stabilize the reconstruction.

3.9.1 Wavenumber filtering

If noisy input data causes the extrapolated higher order Fourier components to blow up, as discussed in Section 3.7, it is natural to try to reduce the contribution of these components. This is generally known as low-pass wavenumber filtering. The most basic filter is realized by a rectangular function that sets the problematic components to zero. The sharp cut-off of a rectangular function can cause ringing effects, however, which is why tapered windows are preferred in general. Fairly early in the development of NAH, a filter with exponential taper was suggested [64] for planar geometry:

$$X_f(k, k_c, \alpha) = \begin{cases} 1 - \frac{1}{2}\mathrm{e}^{(k/k_c - 1)/\alpha}, & k \leq k_c \\ \frac{1}{2}\mathrm{e}^{1-(k/k_c)/\alpha}, & k > k_c \end{cases}, \tag{3.9.1}$$

in which $k = \sqrt{k_x^2 + k_y^2}$ represents the so-called radiation circle outside of which wavenumbers indicate evanescent waves, meaning they are subsonic. A thorough discussion of the wavenumber space in regard to radiation problems and the wavenumber filtering required in NAH is given by Williams [28]. The exponential taper of the filter is explained by the exponential rise in Eq. (3.1.2) for subsonic wavenumbers. The parameter k_c represents the cut-off number and α determines the slope of the cut-off. The cut-off value has to be chosen by hand, which requires a certain amount of a priori knowledge of the source. It was therefore suggested to use some form of regularization that can replace the procedure of manually selecting such filter parameters [65].

Although the bending wave near-field is a different physical effect than the hydrodynamic near-field, its mathematical description is similar, wherefore the numerical effect to be battled is similar. It is therefore assumed that the same type of filter can be used to stabilize the extrapolation of a bending wave field:

$$X_p(n, n_c, \alpha) = \begin{cases} 1 - \frac{1}{2}\mathrm{e}^{(|n|/n_c - 1)/\alpha}, & |n| \leq n_c \\ \frac{1}{2}\mathrm{e}^{1-(|n|/n_c)/\alpha}, & |n| > n_c \end{cases}, \tag{3.9.2}$$

in which n_c represents the cut-off number for the (positive and negative) n Fourier components v_n.

The stabilized mathematical procedure for infinite plates is summarized as

$$v(r_\mathrm{S},\varphi,\omega)=\mathcal{F}_\varphi^{-1}\left\{X_p(n,n_c,\alpha)\mathbf{Q}_n^\mathrm{inf}(r_\mathrm{S},\omega)\begin{bmatrix}\mathbf{Q}_n^\mathrm{inf}(r_1,\omega)\\ \mathbf{Q}_n^\mathrm{inf}(r_2,\omega)\end{bmatrix}^{-1}\begin{bmatrix}\mathcal{F}_\varphi\{v(r_1,\varphi,\omega)\}\\ \mathcal{F}_\varphi\{v(r_2,\varphi,\omega)\}\end{bmatrix}\right\}, \tag{3.9.3}$$

and for finite plates it is summarized as

$$v(r_\mathrm{R},\varphi,\omega)=\mathcal{F}_\varphi^{-1}\left\{X_p(n,n_c,\alpha)\mathbf{Q}_n^\mathrm{fin}(r_\mathrm{R},\omega)\begin{bmatrix}\mathbf{Q}_n^\mathrm{fin}(r_1,\omega)\\ \mathbf{Q}_n^\mathrm{fin}(r_2,\omega)\\ \mathbf{Q}_n^\mathrm{fin}(r_3,\omega)\\ \mathbf{Q}_n^\mathrm{fin}(r_4,\omega)\end{bmatrix}^{-1}\begin{bmatrix}\mathcal{F}_\varphi\{v(r_1,\varphi,\omega)\}\\ \mathcal{F}_\varphi\{v(r_2,\varphi,\omega)\}\\ \mathcal{F}_\varphi\{v(r_3,\varphi,\omega)\}\\ \mathcal{F}_\varphi\{v(r_4,\varphi,\omega)\}\end{bmatrix}\right\}. \tag{3.9.4}$$

Although formally similar, the filter according to Eq. (3.9.2) is a rather loose analogy to Eq. (3.9.1). Unlike k, which differentiates propagating and evanescent waves that are radiated from a structure, $|n|$ does not do the same for bending waves in a structure. Equation (3.9.2) merely states to which extent a certain number of Fourier components are excluded from the reconstruction process, without discerning propagating or evanescent components. This is shown in Fig. 3.8. Because n relates to the N sampling points used for measurement, n_c has a very practical meaning nonetheless. In Fig. 3.8, the reconstruction of the velocity distribution along the source contour of a fictitious source is considered. Despite only slight noise corruption, the reconstruction of the corresponding higher-order Fourier components becomes increasingly unstable. The filter cuts the problematic components from the spectrum, depending on n_c and α.

3.9.2 Tikhonov regularization

A look at Eqs. (3.3.1) and (3.4.1) shows that the problem considered in this thesis is of the form

$$v(r_\mathrm{R},\varphi,\omega)=\mathcal{F}_\varphi^{-1}\left\{\mathbf{g}\mathbf{A}^{-1}\mathbf{b}\right\}, \tag{3.9.5}$$

where $\mathbf{g}$ is the image velocity propagator, $\mathbf{A}\in\mathbb{C}^{m\times m}$ is the square matrix formed by the hologram velocity propagators and $\mathbf{b}\in\mathbb{C}^{m\times 1}$ is the Fourier transformed measured velocity. The heart of the problem is to find

$$\mathbf{x}=\mathbf{A}^{-1}\mathbf{b}, \tag{3.9.6}$$

that is to solve the linear system of equations

$$\mathbf{A}\mathbf{x}=\mathbf{b}, \tag{3.9.7}$$

with $\mathbf{x}\in\mathbb{C}^{m\times 1}$ being the solution for the expansion coefficients that determine the reconstructed velocity.

An important tool in the analysis of ill-posed problems, assuming $\mathbf{A} \in \mathbb{C}^{l\times m}$ with $l \geq m$ for generality, is the *singular value decomposition* (SVD)

$$A = U\Sigma V^T = \sum_{i=1}^{m} u_i \sigma_i v_i^T. \tag{3.9.8}$$

Here, $U \in \mathbb{C}^{l\times l}$ and $V \in \mathbb{C}^{m\times m}$ are matrices consisting of the orthonormal column vectors u_i and v_i, respectively. The diagonal elements of the matrix $\Sigma = \mathrm{diag}(\sigma_1, ..., \sigma_n) \in \mathbb{C}^{l\times m}$ are the *singular values* of $\mathbf{A}$ that appear in decreasing order $\sigma_1 \geq \sigma_2 \geq ... \geq \sigma_n \geq 0$. This means that $\mathbf{A}$ maps the orthonormal vectors v_i into the orthogonal directions u_i, with the singular values σ_i as scaling factors. It is thus possible to determine the solution to the system of equations

$$x = \sum_{i=1}^{\mathrm{rank}(A)} \frac{u_i^T b}{\sigma_i} v_i. \tag{3.9.9}$$

Although the system in Eq. (3.9.7) is fully determined and therefore has an exact solution, $\mathbf{A}$ is ill-conditioned if the wave field of a finite plate is to be reconstructed. This can be seen by looking at the condition number

$$\mathrm{cond}(\mathbf{A}) = \|\mathbf{A}\|_2 \left\|\mathbf{A}^{-1}\right\|_2 = \max(\sigma_i)/\min(\sigma_i), \tag{3.9.10}$$

in which $\|\mathbf{A}\|_2$ is the Euclidian norm of $\mathbf{A}$. The condition number of $\mathbf{A}$ is the ratio of its largest singular value to its smallest and quantifies the sensitivity of the solution $\mathbf{x}$ to a small change in the input data $\mathbf{b}$. The higher the condition number, the more likely it is for the solution to become erratic. The condition numbers that are obtained for $\mathbf{A}$ in the finite plate scenario are plotted in Fig. 3.9, as a function of the Fourier component index n. Curves are shown for different spans of the inner and outer hologram contour

$$d_{\mathrm{span}} = r_3 - r_2, \tag{3.9.11}$$

for different frequencies that are given by the *number of bending wavelengths per unit meter*[6]. The numbers are very bad, especially if d_{span} is large compared to the considered bending wavelength. This indicates that a straightforward application of the procedure in practice could fail quite spectacularly if the numerical side is left unmodified.

A common way to stabilize an ill-posed and ill-conditioned problem is to introduce additional information about the desired solution. This is called *regularization*. Due to the large number and diversity of ill-posed problems that have been considered over time, a vast range of different regularization methods have been developed. Algorithms can be separated in *direct* and *iterative* methods [66] and in addition there are different methods for choosing the regularization parameters.

[6] See the description in Section 5.4

Tikhonov regularization is probably the most common form of direct regularization, although it is not necessarily the best choice for any given problem. The main idea behind Tikhonov regularization is to alter the original ill-posed problem and consider a less sensitive approximation instead. If the alteration is subtle enough, then the solution to the regularized problem will hopefully be an acceptable approximation of the true solution. In mathematical terms, Tikhonov regularization of a discrete ill-posed problem is a minimization problem

$$\min\{\|\mathbf{A}\mathbf{x}-\mathbf{b}\|_2^2+\lambda^2\Omega(\mathbf{x})^2\}, \tag{3.9.12}$$

where the function $\|\mathbf{A}\mathbf{x}-\mathbf{b}\|_2^2$ is called the *residual norm*, the function $\Omega(\mathbf{x})$ is called the *smoothing norm* and λ is called the *regularization parameter*. In so-called standard form, the regularized solution is

$$x_{\text{reg}}=\text{argmin}\{\|\mathbf{A}\mathbf{x}-\mathbf{b}\|_2^2+\lambda^2\|\mathbf{x}-\mathbf{x}^*\|_2^2\}, \tag{3.9.13}$$

where $\mathbf{x}^*$ is an a priori estimation of the solution vector $\mathbf{x}$. The regularized solution of Eq. (3.9.13) can also be obtained by means of SVD and filter factors f_i:

$$x_{\text{reg}}=\sum_{i=1}^{m} f_i\frac{u_i^T b}{\sigma_i}v_i=\sum_{i=1}^{m}\frac{\sigma_i^2}{\sigma_i^2+\lambda^2}\frac{u_i^T b}{\sigma_i}v_i=\sum_{i=1}^{m}\frac{\sigma_i u_i^T b}{\sigma_i^2+\lambda^2}v_i. \tag{3.9.14}$$

In this way, Tikhonov regularization can be interpreted as a filter that "dampens" problematic components corresponding to the singular values $\sigma_i<\lambda$. Equation (3.9.14) is important because it allows a very simple numerical implementation of Tikhonov regularization. In Chapters 5 and 6 the corresponding part of a publicly available MATLAB®-toolbox created by Hansen [67] is used for that purpose.

Equation (3.9.13) shows that the regularized solution depends heavily on the choice of the regularization parameter λ but may also be informed by an estimation $\mathbf{x}^*$ of the expected solution. Essentially, λ dictates the tradeoff between stability and accuracy. Seen in the physical context of this thesis, the larger λ is chosen, the smoother the reconstruction, but the greater the risk of underestimating the correct response magnitude. On the other hand, small λ mean that the original problem is approximated closely, leaving it probably unstable. It is noted that the choice of the regularization parameter is an extensive topic by itself that offers different established methods. No such method will be applied or discussed in this thesis since an investigation of a suitable method would steer too far outside its scope. Nevertheless, the choice of the regularizaton parameter is crucial and will be commented on.

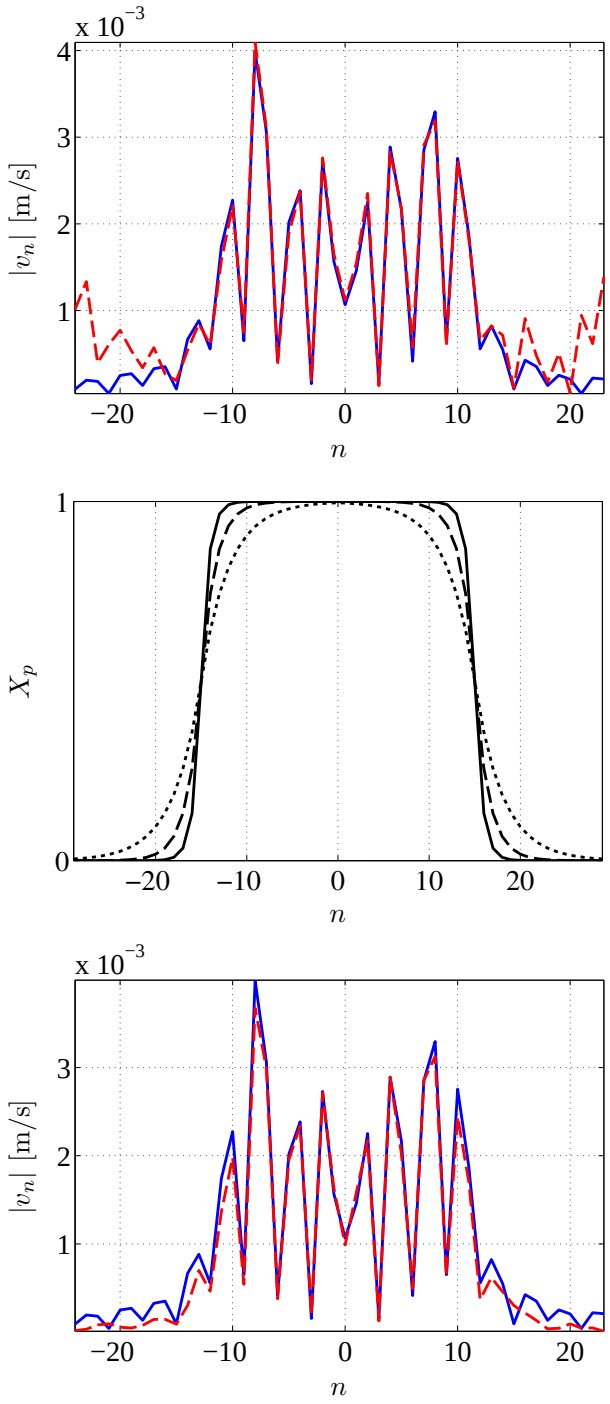

(a) unfiltered

(b) tapered filter for $|n_c| = 15$

(c) wavenumber-filtered

Figure 3.8: Filter curves and wavenumber spectrum for $(1\,\mathrm{m})/\lambda_B = 10$; — analytical solution; - - reconstruction from backward-propagation; — $\alpha = 0.05$, - - $\alpha = 0.1$, · · · $\alpha = 0.2$.

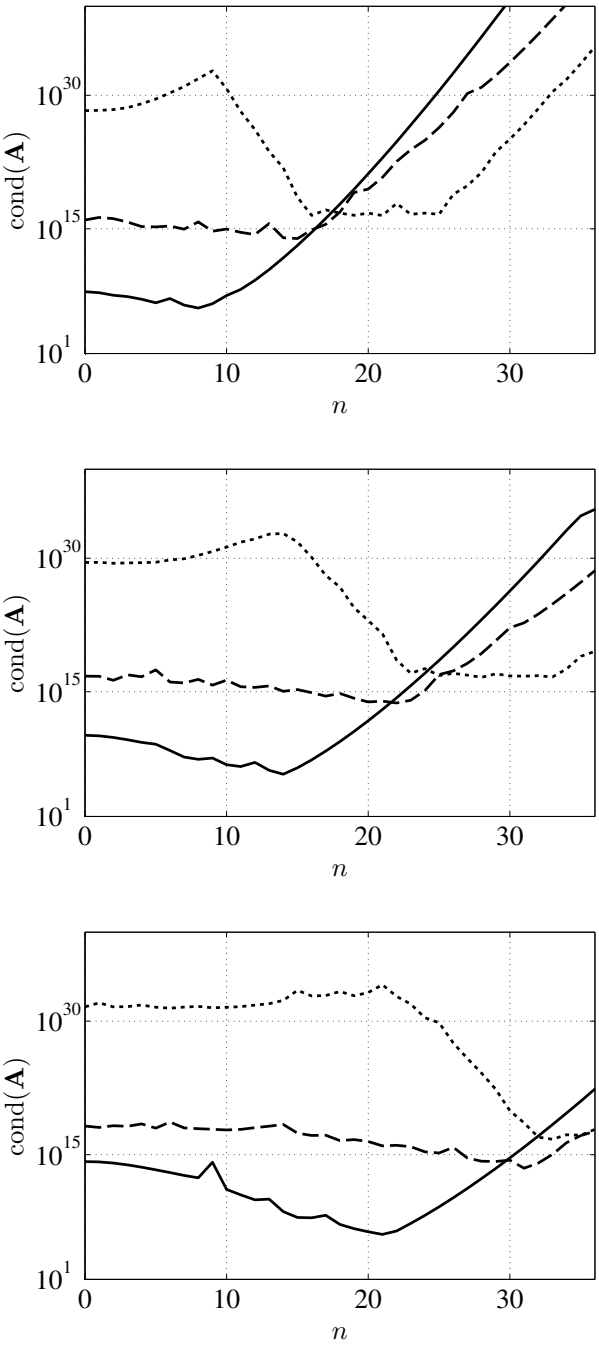

(a) $(1\,\mathrm{m})/\lambda_B = 2$

(b) $(1\,\mathrm{m})/\lambda_B = 5$

(c) $(1\,\mathrm{m})/\lambda_B = 10$

Figure 3.9: Condition numbers for NSBSH in the case of finite plates; — $d_{\mathrm{span}} = 2\lambda_B$, - - $d_{\mathrm{span}} = 5\lambda_B$, ··· $d_{\mathrm{span}} = 10\lambda_B$.

4

Theory for Kirchhoff-Helmholtz integral-based bending wave field extrapolation

Assuming far-field conditions, this chapter describes the utilization of the Kirchhoff-Helmholtz integral for the extrapolation of bending wave fields in thin homogenous plates. To that end, the governing differential equation is used to derive the two-dimensional form of Green's function first. The two-dimensional form of the Kirchhoff-Helmholtz integral is then derived generally and ultimately formulated in terms of the normal structural velocity of a plate. Both infinite and finite plates are thereby considered.

4.1 Green's function for bending wave propagation in the far-field

In textbooks on physics, Green's functions are usually derived for either one- or three-dimensional coordinate systems. It is less straightforward to derive the two-dimensional case in a direct manner. One way to do so is to start from the inhomogenous wave equation in Cartesian coordinates and use Fourier transforms and contour integration. This approach is used by Hoerchens [21], for example, in order to derive Green's function for bending wave propagation in a thin plate. Here, it will be applied in order to derive Green's corresponding far-field function.

In order to find Green's function for the propagation of bending waves in the far-field of a thin homogenous plate, first the inhomogenous bending wave equation is considered

$$\frac{B'}{m''}\nabla^2\nabla^2 u(x,y,t) + \frac{\partial^2 u(x,y,t)}{\partial t^2} = -\frac{F_0(t)}{m''}\delta(x-x_0)\delta(y-y_0), \tag{4.1.1}$$

where $F_0(t)$ is a point force at the position x_0, y_0. Apart from the excitation, Eq. (4.1.1) is identical to Eq. (3.2.1). A temporal Fourier transform of Eq. (4.1.1) yields

$$\nabla^2\nabla^2 u(x,y,\omega) - k_B^4 u(x,y,\omega) = -Q_0(\omega)\delta(x-x_0)\delta(y-y_0), \tag{4.1.2}$$

where

$$Q_0(\omega) = \frac{F_0(\omega)}{B'}. \tag{4.1.3}$$

Because Eq. (4.1.2) is supposed to describe a linear system, it can be separated into the following equations

$$\nabla^2 u_1(x,y,\omega) + k_B^2 u_1(x,y,\omega) = -Q_{0,1}(\omega)\delta(x-x_0)\delta(y-y_0), \tag{4.1.4}$$

$$\nabla^2 u_2(x,y,\omega) - k_B^2 u_2(x,y,\omega) = -Q_{0,2}(\omega)\delta(x-x_0)\delta(y-y_0). \tag{4.1.5}$$

As seen in Section 3.2, u_2 represents an evanescent wave and might therefore be neglected if far-field conditions are given. In this case, bending wave propagation is adequately described by Eq. (4.1.4), i.e. the well-known Helmholtz equation with a wavenumber that includes the effect of dispersion. Green's two-dimensional free space function $G(x, x_0|y, y_0)$ is defined as the solution to the following inhomogenous equation

$$\nabla^2 G(x,y|x_0,y_0) + k_B^2 G(x,y|x_0,y_0) = -\delta(x-x_0)\delta(y-y_0). \tag{4.1.6}$$

The dependence on ω is omitted in the notation of Green's function. This is done to ensure more compact equations in the following and to further differentiate Green's functions from the propagation functions used in Chapter 3. Taking the spatial Fourier transform of Eq. (4.1.6),

$$\mathcal{F}_x\mathcal{F}_y\{\nabla^2 G(x,y|x_0,y_0) + k_B^2 G(x,y|x_0,y_0)\} = \mathcal{F}_x\mathcal{F}_y\{-\delta(x-x_0)\delta(y-y_0)\}, \tag{4.1.7}$$

yields

$$(-k_x^2 - k_y^2)G(k_x,k_y) + k_B^2 G(k_x,k_y) = -\mathrm{e}^{jk_x x_0}\mathrm{e}^{jk_y y_0} \tag{4.1.8}$$

which can be rearranged to

$$G(k_x,k_y) = -\frac{\mathrm{e}^{jk_x x_0 + jk_y y_0}}{k_B^2 - k_x^2 - k_y^2}. \tag{4.1.9}$$

The inverse spatial Fourier transform of this equation leads to the following integral representation of Green's function

$$\begin{aligned} G(x,y|x_0,y_0) &= \mathcal{F}_x^{-1}\mathcal{F}_y^{-1}\{G(k_x,k_y)\} \\ &= -\frac{1}{4\pi^2}\iint_{-\infty}^{\infty} \frac{\mathrm{e}^{-j[k_x(x-x_0)+k_y(y-y_0)]}}{k_B^2 - k_x^2 - k_y^2}\,\mathrm{d}k_x\,\mathrm{d}k_y. \end{aligned} \tag{4.1.10}$$

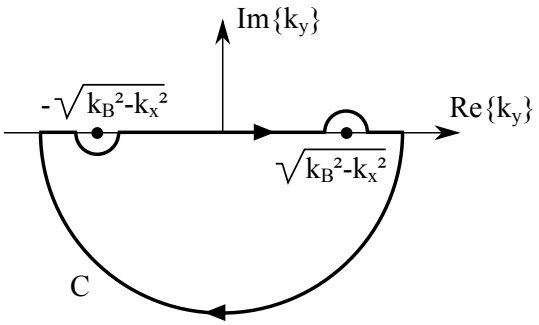

Figure 4.1: Path for the contour integral in Eq. (4.1.11).

By factorizing the denominator in Eq. (4.1.10), one of the integrals can be interpreted as a contour integral in the k_y-plane, so that

$$G(x,y|x_0,y_0) = \frac{1}{4\pi^2}\int_{-\infty}^{\infty}\oint_C \frac{\mathrm{e}^{-j[k_x(x-x_0)+k_y(y-y_0)]}}{k_y+\sqrt{k_B^2-k_x^2}}\frac{1}{k_y-\sqrt{k_B^2-k_x^2}}\,\mathrm{d}k_y\,\mathrm{d}k_x. \tag{4.1.11}$$

By choosing the contour path shown in Fig. 4.1, application of the residue theorem for a single pole,

$$\oint_C f(z)\,\mathrm{d}z = 2\pi j \lim_{z\to a}(z-a)f(z), \tag{4.1.12}$$

leads to

$$G(x,y|x_0,y_0) = -\frac{j}{4\pi}\int_{-\infty}^{\infty}\frac{\mathrm{e}^{-j[k_x(x-x_0)+\sqrt{k_B^2-k_x^2}(y-y_0)]}}{\sqrt{k_B^2-k_x^2}}\,\mathrm{d}k_x. \tag{4.1.13}$$

In order to solve the remaining integral, substitutions have to be carried out. The following substitutions can be used [21]:

$$k_x = k_B\cos(\tau-j\upsilon), \tag{4.1.14}$$
$$\mathrm{d}k_x = jk_B\sin(\tau-j\upsilon)\mathrm{d}\upsilon, \tag{4.1.15}$$
$$\sqrt{k_B^2-k_x^2} = k_B\sin(\tau-j\upsilon), \tag{4.1.16}$$
$$x-x_0 = r\cos(\tau), \tag{4.1.17}$$
$$y-y_0 = r\sin(\tau), \tag{4.1.18}$$
$$r = \sqrt{(x-x_0)^2+(y-y_0)^2}. \tag{4.1.19}$$

By inserting these expressions in Eq. (4.1.13), and by using the identity

$$\cosh(\upsilon) = \cos(\tau-j\upsilon)\cos(\tau)+\sin(\tau-j\upsilon)\sin(\tau), \tag{4.1.20}$$

the following integral is obtained:

$$G(r|r_0) = \frac{1}{4\pi} \int_{-\infty}^{\infty} \mathrm{e}^{-jk_B r \cosh(\upsilon)} \, \mathrm{d}\upsilon. \tag{4.1.21}$$

Finally, from the relation established in Appendix B,

$$H_0^{(2)}(k_B r) = \frac{j}{\pi} \int_{-\infty}^{\infty} \mathrm{e}^{-jk_B r \cosh(\upsilon)} \, \mathrm{d}\upsilon, \tag{4.1.22}$$

Green's function for the far-field-propagation of a bending wave in a thin homogenous plate is obtained as

$$G(r|r_0) = G_{2D}(r|r_0) = -\frac{j}{4} H_0^{(2)}(k_B r). \tag{4.1.23}$$

It is noted that the sign in Eq. (4.1.23) depends on the choice of the sign on the right hand side of Eq. (4.1.6). The general result is equal to that obtained for compressional wave propagation in a fluid. The description of harmonic far-field bending wave propagation in terms of the normal plate response is therefore no different from acoustic pressure propagation in a fluid. This relates to wave field extrapolation as well. Since Kirchhoff's integral equation is known to allow the extrapolation of an airborne wave field, it should allow the extrapolation of a bending wave field as well.

4.2 The general Kirchhoff-Helmholtz integral for the exterior problem

In order to find the integral equation that permits the extrapolation of a bending wave field in a homogenous plate, the general form of the Kirchhoff-Helmholtz integral for any type of homogenous and isotropic volume is derived first. The sought-after extrapolation method will be referred to as *Kirchhoff-Helmholtz integral extrapolation* (KHI). The derivation is based on Williams' considerations [28] rather than the somewhat shorter methodology used in other relevant textbooks, e.g. [68], in which the Kirchhoff-Helmholtz integral follows from the general solution of the inhomogenous wave equation. In the following expressions, the function argument ω is omitted again.

A Volume V bounded by the surface $S = S_i + S_\infty$ is considered, as depicted in Fig. 4.2. S_∞ is imagined as the surface of a sphere whose radius tends toward infinity. If only sources inside S_i are present, it is assumed that the continuous functions $\Phi(r)$ and $\Psi(r)$ satisfy the homogenous Helmholtz equations

$$\nabla^2 \Phi + k^2 \Phi = 0, \tag{4.2.1}$$

$$\nabla^2 \Psi + k^2 \Psi = 0, \tag{4.2.2}$$

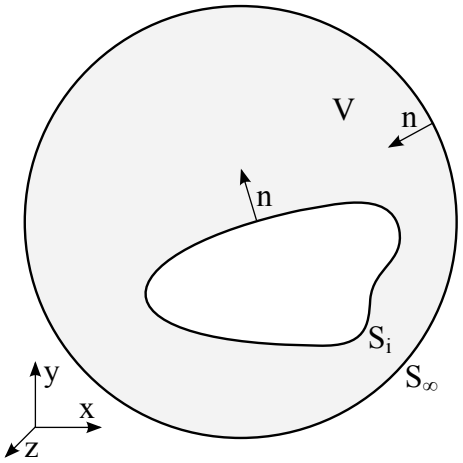

Figure 4.2: Infinite volume V surrounding the boundary surface S_i with the surface normal n.

for all points $r = \sqrt{(x-x_0)^2 + (y-y_0)^2 + (z-z_0)^2}$ within the volume, including the surface. Since the derivatives of these functions are continuous as well, the functions obey Green's second theorem

$$\iiint_V (\Phi\nabla^2\Psi - \Psi\nabla^2\Phi)\mathrm{d}V = \iint_S (\Phi\frac{\partial\Psi}{\partial n} - \Psi\frac{\partial\Phi}{\partial n})\ \mathrm{d}S, \tag{4.2.3}$$

in which $\frac{\partial}{\partial n}$ is considered to be the derivative with respect to the surface normal n. Here, the normal is chosen such that it points toward the volume of interest, as shown in Fig. 4.2. By subtraction of Eq. (4.2.1) times Ψ from Eq. (4.2.2) times Φ, and through substitution of the resulting expression in Eq. (4.2.3), the following integral equation is obtained:

$$\iint_S (\Phi\frac{\partial\Psi}{\partial n} - \Psi\frac{\partial\Phi}{\partial n})\ \mathrm{d}S = 0. \tag{4.2.4}$$

Assuming that a wave field described by $\Psi(r)$ is only generated by a point source at r', then $\Psi(r)$ is Green's free space function $G_{3D}(r|r') = G(r|r')$, i.e. the solution to the inhomogenous equation

$$\nabla^2 G(r|r') + k^2 G(r|r') = -\delta(r - r'). \tag{4.2.5}$$

Equation (4.2.5) represents the three-dimensional form of Eq. (4.1.6) that has been presented in Section 4.1. Because the principle of reciprocity holds for Green's functions,

$$G(r|r') = G(r'|r). \tag{4.2.6}$$

The singularity presented by the point source violates the requirement of continuity in Green's theorem, however. In order to apply the theorem, the source point r'

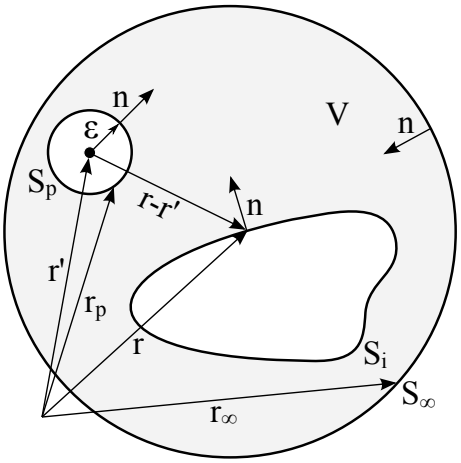

Figure 4.3: Geometry for the derivation of the exterior problem Kirchhoff-Helmholtz integral; Green's theorem is applicable in the volume V bounded by the surfaces S_p, S_i and S_∞.

can be excluded from the volume by surrounding it with a small sphere of radius ϵ and surface S_p, as shown in Fig. 4.3. Both $\Phi(r)$ and $G(r|r')$ are thus continuous in V. It follows that

$$S = S_p + S_i + S_\infty. \tag{4.2.7}$$

Using Eq. (4.2.7) with Eq. (4.2.4) results in

$$\begin{aligned} 0 = &\iint_{S_i} (\Phi(r)\frac{\partial G(r|r')}{\partial n} - G(r|r')\frac{\partial \Phi(r)}{\partial n})\ \mathrm{d}S_i \\ &+ \lim_{\epsilon\to 0} \iint_{S_p} (\Phi(r_p)\frac{\partial G(r_p|r')}{\partial n} - G(r_p|r')\frac{\partial \Phi(r_p)}{\partial n})\ \mathrm{d}S_p \\ &+ \lim_{r_\infty\to\infty} \iint_{S_\infty} (\Phi(r_\infty)\frac{\partial G(r_\infty|r')}{\partial n} - G(r_\infty|r')\frac{\partial \Phi(r_\infty)}{\partial n})\ \mathrm{d}S_\infty. \end{aligned} \tag{4.2.8}$$

By considering Green's function on the the small sphere

$$G(r_p|r') = \frac{\mathrm{e}^{-jk|r_p - r'|}}{4\pi|r_p - r'|} = \frac{\mathrm{e}^{-jk\epsilon}}{4\pi\epsilon} \tag{4.2.9}$$

and the surface element in spherical coordinates

$$dS_p = \epsilon^2 \sin\theta\ \mathrm{d}\theta\ \mathrm{d}\varphi \equiv \epsilon^2 \mathrm{d}\Omega, \tag{4.2.10}$$

it can be shown that for the second integral in Eq. (4.2.8)

$$\lim_{\epsilon\to 0} \iint_{S_p} (\Phi(r_p)\frac{\partial G(r_p|r')}{\partial n})\ \mathrm{d}S_p = \lim_{\epsilon\to 0} \Phi(r_p) \iint_\Omega \frac{1}{4\pi}\frac{\partial \mathrm{e}^{-jk\epsilon}/\epsilon}{\partial \epsilon}\epsilon^2\ \mathrm{d}\Omega = -\Phi(r') \tag{4.2.11}$$

and

$$\lim_{\epsilon\to 0}\iint_{S_p}(-G(r_p|r')\frac{\partial\Phi(r_p)}{\partial n})\,\mathrm{d}S_p = \lim_{\epsilon\to 0}\frac{\partial\Phi(r_p)}{\partial\epsilon}\iint_{\Omega}\frac{\mathrm{e}^{-jk\epsilon}\epsilon}{4\pi}\,\mathrm{d}\Omega = 0. \tag{4.2.12}$$

From a physical point of view, the third integral in Eq. (4.2.8) must vanish because there are no sources that could contribute from infinity. By using Green's function on the infinite sphere

$$G(r_\infty|r') = \frac{\mathrm{e}^{-jk|r_\infty - r'|}}{4\pi|r_\infty - r'|} \approx \frac{\mathrm{e}^{-jk|r_\infty - r'|}}{4\pi r_\infty}, \tag{4.2.13}$$

the integral must be

$$\lim_{r_\infty\to\infty}\frac{1}{4\pi}\iint_{S_\infty}(-\Phi(r_\infty)\frac{\partial}{\partial r_\infty}\frac{\mathrm{e}^{-jk|r_\infty - r'|}}{r_\infty} + \frac{\mathrm{e}^{-jk|r_\infty - r'|}}{r_\infty}\frac{\partial\Phi(r_\infty)}{\partial r_\infty})\,\mathrm{d}S_\infty = 0. \tag{4.2.14}$$

Because the mathematical solution of the Helmholtz equation allows both incoming and outgoing waves, Eq. (4.2.14) does not hold by default, however. For the integral to vanish, all incoming waves have to be rejected. This is achieved by applying Sommerfeld's radiation condition [46]:

$$\lim_{r_\infty\to\infty} r_\infty\left[\frac{\partial\Phi(r_\infty)}{\partial r_\infty} + jk\Phi(r_\infty)\right] = 0. \tag{4.2.15}$$

Inserting Eqs. (4.2.11), (4.2.12) and (4.2.14) in Eq. (4.2.8) yields the Kirchhoff-Helmholtz integral equation for the exterior problem

$$K\Phi(r') = -\iint_{S_i}(G(r|r')\frac{\partial\Phi(r)}{\partial n} - \Phi(r)\frac{\partial G(r|r')}{\partial n})\,\mathrm{d}S_i, \tag{4.2.16}$$

where

$$K = \begin{cases} 1, & r'\in V \\ 1/2, & r'\in S_i \\ 0, & r'\notin V \end{cases}.$$

If r' is a point on S_i, only half of S_p lies within V, wherefore the left hand side of Eq. (4.2.16) will have a factor 1/2. If r' is a point outside of S_i, the left hand side of Eq. (4.2.16) will be zero since the homogenous case of Eq. (4.2.4) applies. The latter means that the wave field will be computed as zero if the point r' and the source are located on the same side of the boundary. Since the corresponding factor K is the same for any iteration of the integral, it will be omitted after Section 4.3.

Most importantly, Eq. (4.2.16) states that the wave field at any point r' in a source-free volume surrounding an arbitrary boundary surface S_i can be calculated from knowledge of the field and the field gradient on the surface. The first integrand represents the contribution of monopole sources across the surface, while the second integrand can be interpreted as the contribution of dipole sources.

4.3 The general Kirchhoff-Helmholtz integral for a combined boundary problem

The derivation in Section 4.2 can be adapted to suit a combined boundary value problem. It is assumed that the volume of interest is now bounded by two arbitrary finite surfaces S_i and S_e, as depicted in Fig. 4.4.

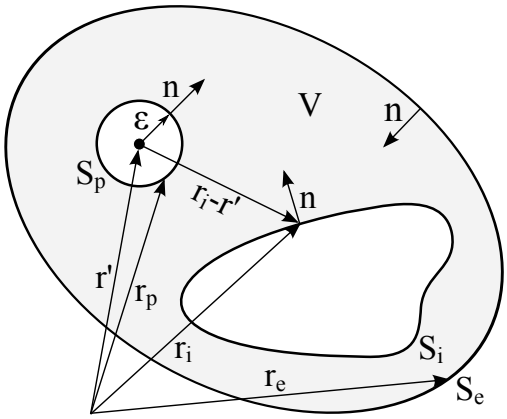

Figure 4.4: Geometry for the derivation of the combined problem Kirchhoff-Helmholtz integral; Green's theorem is applicable in the volume V bounded by the surfaces S_p, S_i and S_e.

It can be imagined that sources exist inside S_i and outside of S_e. In order to derive the corresponding integral, the methodology of Section 4.2 can be used, whereby the pairs r, S_i and r_∞, S_∞ are exchanged for r_i, S_i and r_e, S_e. The only difference to the exterior problem is found in the third integral in Eq. (4.2.8), which is taken over the finite surface S_e now and will not vanish. As a consequence, the Kirchhoff-Helmholtz integral for the combined problem is

$$\begin{aligned} K\Phi(r') = &- \iint_{S_i} (G(r_i|r')\frac{\partial\Phi(r_i)}{\partial n} - \Phi(r_i)\frac{\partial G(r_i|r')}{\partial n})\ \mathrm{d}S_i \\ &- \iint_{S_e} (G(r_e|r')\frac{\partial\Phi(r_e)}{\partial n} - \Phi(r_e)\frac{\partial G(r_e|r')}{\partial n})\ \mathrm{d}S_e, \end{aligned} \tag{4.3.1}$$

where

$$K = \begin{cases} 1, & r' \in V \\ 1/2, & r' \in S_i \vee S_e \\ 0, & r' \notin V \end{cases}.$$

The statement of Eq. (4.3.1) is clear: If the wave field and its gradient are known across both the inner and the outer bounding surface, the field in the encompassed volume can be determined at any point.

4.4 Applicability of the general Kirchhoff-Helmholtz integral to a 2D-problem

Physically, the 2D-problem can be viewed as a special case of the 3D-problem, i.e. the case where the field distribution is independent of a third coordinate. This reasoning can be employed for 2D-applications of the Kirchhoff-Helmholtz integral, as discussed by Spors [69] or Rabenstein et al. [70]. If the wave field does not change along the third coordinate, the normal derivatives of the field $\frac{\partial}{\partial n}$ are independent of that coordinate as well. The considered volume can then be interpreted as a prism, as illustrated in Fig. 4.5. The surface integral over S_i can therefore be split into an integral along the contour C and an integral over z.

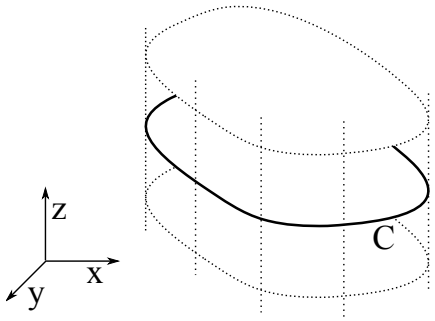

Figure 4.5: Considered volume for the Kirchhoff-Helmholtz integral if the wave field does not depend on the z-coordinate.

Equation (4.2.16) is thus rewritten as

$$\begin{aligned}\Phi(r') &= -\iint_{S_i} G_{3D}(r|r')\frac{\partial\Phi(r)}{\partial n}\mathrm{d}S_i + \iint_{S_i}\Phi(r)\frac{\partial G_{3D}(r|r')}{\partial n}\,\mathrm{d}S_i \\ &= -\int_C \frac{\partial\Phi(r)}{\partial n}\int_{-\infty}^{\infty} G_{3D}(r|r')\,\mathrm{d}z\,\mathrm{d}C + \int_C \Phi(r)\int_{-\infty}^{\infty}\frac{\partial G_{3D}(r|r')}{\partial n}\,\mathrm{d}z\,\mathrm{d}C.\end{aligned} \tag{4.4.1}$$

Using the relation between two- and three-dimensional free-space Green functions for a medium free of shear stresses [28]

$$\int_{-\infty}^{\infty} G_{3D}(r|r')\,\mathrm{d}z = -\frac{j}{4}H_0^{(2)}(k\sqrt{(x'-x)^2+(y'-y)^2}) = G_{2D}(r|r'), \tag{4.4.2}$$

Eq. (4.4.1) becomes

$$\Phi(r') = -\int_{C_i}(G_{2D}(r|r')\frac{\partial\Phi(r)}{\partial n} - \Phi(r)\frac{\partial G_{2D}(r|r')}{\partial n})\,\mathrm{d}C_i. \tag{4.4.3}$$

Equivalently, Eq. (4.3.1) becomes

$$\begin{aligned}\Phi(r') = &- \int_{C_i} (G_{2D}(r_i|r')\frac{\partial\Phi(r_i)}{\partial n} - \Phi(r_i)\frac{\partial G_{2D}(r_i|r')}{\partial n})\ \mathrm{d}C_i \\ &- \int_{C_e} (G_{2D}(r_e|r')\frac{\partial\Phi(r_e)}{\partial n} - \Phi(r_e)\frac{\partial G_{2D}(r_e|r')}{\partial n})\ \mathrm{d}C_e.\end{aligned} \tag{4.4.4}$$

These results show that the Kirchhoff-Helmholtz integral can be applied to two-dimensional problems as well, given that the corresponding Green function is known.

4.5 The Kirchhoff-Helmholtz integral for infinite plates

For thin plates in bending vibration, for which Eq. (3.2.35) is valid, the structural velocity can be assumed not to change along the coordinate normal to the plate surface. In other words, the normal surface velocity is more or less equal to that of the neutral layer. Bending wave propagation therefore poses a two-dimensional problem, for which Green's function has been derived in Section 4.1. The desired integral formulation requires the derivative of Green's function with respect to the contour normal n

$$\frac{\partial}{\partial n}G_{2D}(r|r') = \frac{j}{4}k_B H_1^{(2)}(k_B|r-r'|)\cos(\alpha), \tag{4.5.1}$$

where α is the angle between n and the vector from the considered field point to the boundary contour position, depicted in Fig. 4.6. If the field of the normal velocity $\Phi(r,\omega) = v(r,\omega)$ is considered, inserting Eqs. (4.1.23) and (4.5.1) into Eq. (4.4.3) yields an explicit formulation of the Kirchhoff-Helmholtz integral for the infinite plate:

$$\begin{gathered}v(r',\omega) = \\ \frac{j}{4}\int_{C_i}\left\{H_0^{(2)}(k_B|r-r'|)\frac{\partial}{\partial n}v(r,\omega) + v(r,\omega)k_B H_1^{(2)}(k_B|r-r'|)\cos(\alpha)\right\}\mathrm{d}C_i.\end{gathered} \tag{4.5.2}$$

In practice, the boundary contour C_i has to be divided into N segments, wherefore Eq. (4.5.2) will be approximated by the sum

$$\begin{gathered}v(r',\omega) = \\ \frac{j}{4}\sum_{m=1}^{N}\left\{H_0^{(2)}(k_B|r_m-r'|)\frac{\partial}{\partial n}v(r_m,\omega) + v(r_m,\omega)k_B H_1^{(2)}(k_B|r_m-r'|)\cos(\alpha)\right\}\Delta C_i.\end{gathered} \tag{4.5.3}$$

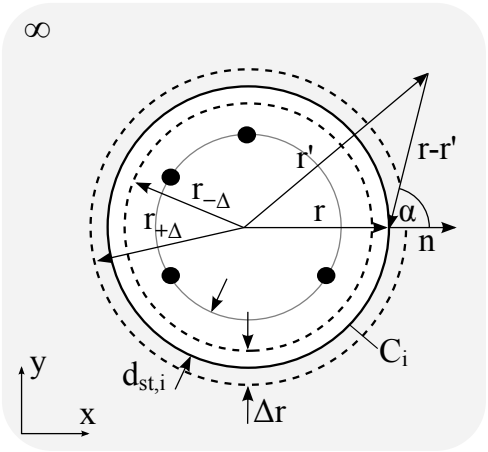

Figure 4.6: Geometry of the Kirchhoff-Helmholtz integral for an infinite plate; — boundary contour; - - auxiliary contour; • normal point force; extrapolatable plate area.

The corresponding geometry used in this thesis is depicted in Fig. 4.6. The required gradient of the field in the direction of the contour normal n is obtained by approximation through the difference quotient

$$\frac{\partial}{\partial n} v(r,\omega) \approx \frac{\Delta v(r,\omega)}{\Delta r} = \frac{v(r_{+\Delta},\omega) - v(r_{-\Delta},\omega)}{r_{+\Delta} - r_{-\Delta}}. \tag{4.5.4}$$

The procedure of KHI is straightforward. The normal velocity has to be sampled along the actual boundary contour of radius r and along two auxiliary contours of radius $r_{+\Delta}$ and $r_{-\Delta}$, respectively. The field along the boundary is thus obtained directly, at a distance $d_{st,i}$ from the sources, while the corresponding gradient of the field is obtained through Eq. (4.5.4), depending on the boundary contour distance

$$\Delta r = r_{+\Delta} - r_{-\Delta}. \tag{4.5.5}$$

The integral can then be evaluated directly without greater numerical difficulty. It is important to note that KHI does not require polar coordinates or circular contours but can be performed with any type of geometry. The circular geometry is reasonable, however, and best suited to compare KHI with NSBSH.

4.6 The Kirchhoff-Helmholtz integral for finite plates

Analogous to Section 4.5, the explicit formulation of the Kirchhoff-Helmholtz integral for the finite plate is given as

$$\begin{aligned} v(r',\omega) = \\ \frac{j}{4}\int_{C_i}\left\{H_0^{(2)}(k_B|r_i-r'|)\frac{\partial}{\partial n}v(r_i,\omega)+v(r_i,\omega)k_B H_1^{(2)}(k_B|r_i-r'|)\cos(\alpha)\right\}\mathrm{d}C_i \\ +\frac{j}{4}\int_{C_e}\left\{H_0^{(2)}(k_B|r_e-r'|)\frac{\partial}{\partial n}v(r_e,\omega)+v(r_e,\omega)k_B H_1^{(2)}(k_B|r_e-r'|)\cos(\beta)\right\}\mathrm{d}C_e, \end{aligned} \tag{4.6.1}$$

in which α and β are the angles between the boundary contour normals and the vectors from the considered field point to the boundary contour positions, as depicted in Fig. 4.7. This expression will also be evaluated by a sum in practice:

$$v(r',\omega) = \frac{j}{4}\sum_{m=1}^{N_i} f_{i,m}\Delta C_i + \frac{j}{4}\sum_{m=1}^{N_e} f_{e,m}\Delta C_e, \tag{4.6.2}$$

with

$$f_{i,m} = H_0^{(2)}(k_B|r_{i,m}-r'|)\frac{\partial}{\partial n}v(r_{i,m},\omega)+v(r_{i,m},\omega)k_B H_1^{(2)}(k_B|r_{i,m}-r'|)\cos(\alpha), \tag{4.6.3}$$

$$f_{e,m} = H_0^{(2)}(k_B|r_{e,m}-r'|)\frac{\partial}{\partial n}v(r_{e,m},\omega)+v(r_{e,m},\omega)k_B H_1^{(2)}(k_B|r_{e,m}-r'|)\cos(\beta), \tag{4.6.4}$$

in which N_i and N_e represent the number of sampling points along the inner and outer contours C_i and C_e, respectively. In analogy to Section 4.5, the gradients can be approximated by difference quotients

$$\frac{\partial}{\partial n}v(r_i,\omega) \approx \frac{v(r_{i+\Delta},\omega)-v(r_{i-\Delta},\omega)}{r_{i+\Delta}-r_{i-\Delta}}, \tag{4.6.5}$$

$$\frac{\partial}{\partial n}v(r_e,\omega) \approx \frac{v(r_{e-\Delta},\omega)-v(r_{e+\Delta},\omega)}{r_{e+\Delta}-r_{e-\Delta}}. \tag{4.6.6}$$

As seen in Fig. 4.7, the corresponding geometry can be chosen conformal to the geometry of the plate, with a distance $d_{st,e}$ between plate edge and outer boundary contour. This is the main advantage over NSBSH, although the measurement effort is even higher. Six contours have to be sampled. Obviously, the effort for calculation is doubled, compared to the infinite plate, because two integrals have to be evaluated. Otherwise, the numerical procedure is identical.

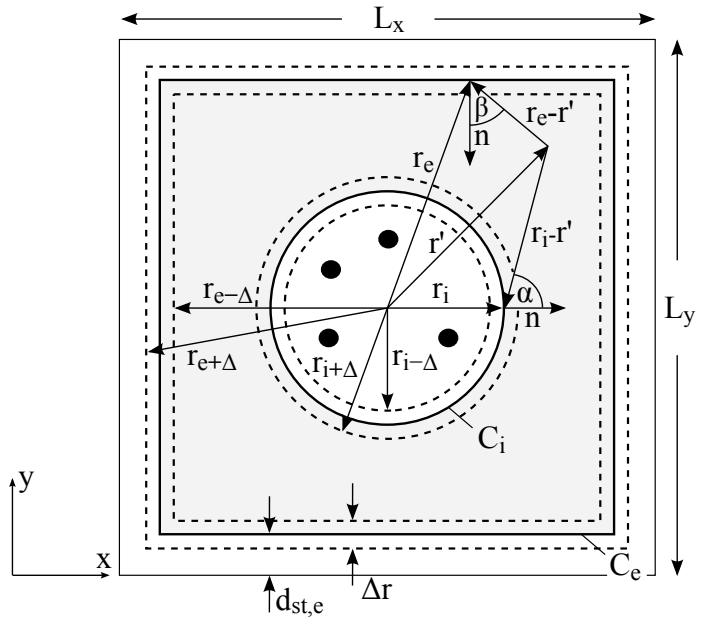

Figure 4.7: Geometry of the Kirchhoff-Helmholtz integral for a finite plate; — boundary contour; - - auxiliary contour; • normal point force; extrapolatable plate area.

4.7 A boundary element approach

As is understood from the preceding sections, the KHI-approach requires a significant amount of measurement effort. Multiple contours have to be sampled in a geometrically rigorous manner because both the velocity response and the gradient of the velocity response have to be determined by measurement. Naturally, this is something the engineer would rather avoid, especially if a scanning system for automated positioning and measurement is not at hand. How this can be avoided is a question inherently addressed by the *Boundary Element Method* (BEM) [71].

In the field of acoustics, the Boundary Element Method usually seeks to solve a discretized system of Kirchhoff-Helmholtz integral equations for the boundary of a given domain and uses the resulting solution to calculate the field within the domain. BEM is also widely applied in structural acoustics. Since the subject of BEM in itself is not central to this thesis, a thorough examination of BEM-approaches for bending wave vibration exceeds the scope of this thesis. Nevertheless, a few basic considerations and practical evaluations shall be made in this regard, which will provide an outlook on future research possibilities. In order to show how a BEM-approach can be used in conjunction with the KHI-formulations discussed above, the idealized case of an infinite plate is considered once more. It is important to note that the following shows a very rudimentary way of im-

plementing BEM in a structural acoustics setting. This is permitted because the considered scenario and its underlying physical model is simple: strictly outgoing wave propagation in polar coordinates in an isotropic homogenous medium, considered in the frequency domain. As a consequence, the mathematical model required to solve the problem is simple, allowing application of BEM in a most straightforward manner. The numerical intricacies that usually come with BEM are therefore not addressed in this thesis.

The boundary contour C_0, replacing the contour C_i in Fig. 4.6, can be divided into M equal segments, i.e. *boundary elements*, each being represented by a so-called *collocation point* that is located at the center of the segment m. If a sufficient number of boundary elements are used, the integral over the contour is approximately given by the sum of the elements. From Section 4.2 it is recalled that the Kirchhoff-Helmholtz integral can also be used to recalculate the field at any point on the boundary. Therefore, for the ith point on the boundary, the Kirchhoff-Helmholtz integral for an infinite plate can be written as

$$\frac{1}{2}v_i = -\sum_{m=1}^{N}\left(G_{im}\frac{\partial v_m}{\partial n} - v_m\frac{\partial G_{im}}{\partial n}\right)\Delta C_0. \tag{4.7.1}$$

By defining matrices of dimension $M \times M$ for the contributing Green functions and their normal derivatives

$$\mathbf{G} = \begin{bmatrix} G_{11} & G_{12} & \cdots & G_{1N} \\ G_{21} & G_{22} & & \vdots \\ \vdots & & \ddots & \vdots \\ G_{N1} & \cdots & \cdots & G_{NN} \end{bmatrix}, \tag{4.7.2}$$

$$\mathbf{G_g} = \begin{bmatrix} \frac{\partial G_{11}}{\partial n} & \frac{\partial G_{12}}{\partial n} & \cdots & \frac{\partial G_{1N}}{\partial n} \\ \frac{\partial G_{21}}{\partial n} & \frac{\partial G_{22}}{\partial n} & & \vdots \\ \vdots & & \ddots & \vdots \\ \frac{\partial G_{N1}}{\partial n} & \cdots & \cdots & \frac{\partial G_{NN}}{\partial n} \end{bmatrix}, \tag{4.7.3}$$

as well as column vectors of length N for the velocity and its normal derivative at any collocation point

$$\mathbf{v} = \begin{bmatrix} v_1 \\ v_2 \\ \vdots \\ v_N \end{bmatrix}, \tag{4.7.4}$$

$$\mathbf{v_g} = \begin{bmatrix} \frac{\partial v_1}{\partial n} \\ \frac{\partial v_2}{\partial n} \\ \vdots \\ \frac{\partial v_N}{\partial n} \end{bmatrix}, \tag{4.7.5}$$

the complete system of equations required to calculate the field at all collocation points according to Eq. (4.7.1) can be written as

$$\frac{1}{2}\mathbf{v} = (\mathbf{G_g v} - \mathbf{G v_g})\,\Delta C_0. \tag{4.7.6}$$

Using matrix inversion, the system can be solved for the gradient of the plate response along C_0

$$\mathbf{v_g} = (\mathbf{G}\Delta C_0)^{-1}(\frac{1}{2}\mathbf{v} - \mathbf{G_g v}\Delta C_0). \tag{4.7.7}$$

In this way, all information required for KHI is obtained by performing discrete measurement along one boundary contour instead of three. Obviously, BEM is a numerical way of performing KHI, which is why it can be regarded as indirect KHI just as well.

5
Numerical evaluation

In this chapter, the methods proposed in the two preceding chapters are validated and investigated through a set of simulations. Save for two special cases, the simulated scenarios correspond to the experimental setups discussed in Chapter 6. An infinite acrylic plate as well as a free and a simply supported plate excited by point forces are considered. The main focus is laid on the reconstruction of both the continuous spatial wave field and the response spectrum at a specific field point from fictitious response data. The approaches of NSBSH, KHI and KHI-based BEM are thereby compared directly. The simulations are mostly performed using contaminated input data in order to test numerical sensitivity. The influence of relevant measurement parameters, i.e. the number of sampling points, the standoff distance and the amount of noise, is investigated through parameter studies.

5.1 Noise modeling

Even under ideal conditions, the quantities to be determined by measurement fluctuate by a certain amount due to physical effects afflicted with statistical uncertainty. These fluctuations are called random error and are commonly referred to as noise. The measurement hardware, usually consisting of sensors, cables, input connectors and A/D- converters, inevitably generates mechanical-thermal and electrical-thermal noise. Random error is to be distinguished from systematic error which is a predictable inaccuracy in the measurement system, e.g. the miscalibration of a sensor or the phase mismatch of sensors. In practice, even the systematic error may be difficult to evaluate. An example is the positioning of the sensors, which may not be completely accurate. If the data acquisition requires measurements taken at many different positions, as is the case in this thesis, a quasi-random error is introduced additionally.

Because extrapolation procedures can be numerically sensitive, their evaluation has to include the inevitable effect of measurement noise. Inherent noise phenom-

ena exhibit Gaussian probability density distributions. This is reflected in similar models for the simulation of noise used to evaluate inverse methods in structural vibration [6, 72]. In this thesis, accordingly, input data is simulated as

$$v_{\text{noise}} = v_{\text{exact}}\ \Delta v\ \mathrm{e}^{j\Delta\phi}, \tag{5.1.1}$$

with the accurate velocity value v_{exact} and the Guassian random real numbers

$$\Delta v = 1 \pm \sigma_v, \tag{5.1.2}$$

$$\Delta\phi = 0 \pm \sigma_\phi, \tag{5.1.3}$$

with the standard deviations σ_v in percent of the velocity magnitude (percent of meters per second) and σ_ϕ in radians. In the text, the values of σ_ϕ will be given in degrees of phase, however. The model therefore comprises multiplicative noise on the magnitude and additive noise on the phase of the velocity response.

By considering the level difference between contaminated and accurate input data along a simulated measurement contour

$$\Delta L_{v,\text{input}}(x) = 10\log\Big|\frac{v_{\text{noise}}(x)}{v_{\text{exact}}(x)}\Big|^2, \tag{5.1.4}$$

Fig. 5.1 gives a reference for the resulting contamination in absolute terms.

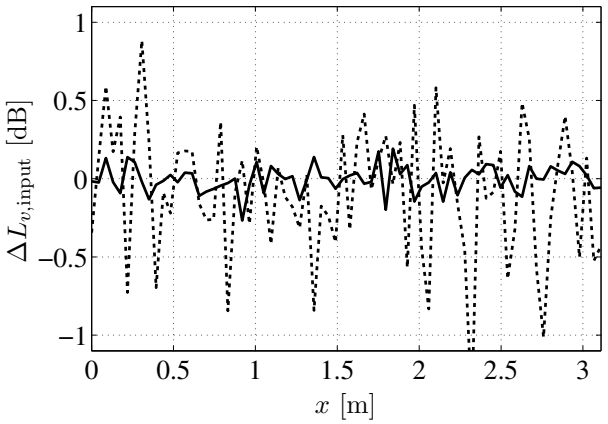

Figure 5.1: Example for the simulated level difference between contaminated and accurate velocity; — $\sigma_v = 1\,\%$, $\sigma_\phi = 1\,°$; · · · $\sigma_v = 5\,\%$, $\sigma_\phi = 5\,°$.

The solid curve represents an example for the resulting level difference when the standard deviations for magnitude and phase are chosen $\sigma_v = 1\,\%$ and $\sigma_\phi = 1\,°$, which is the default noise included for any of the shown results in this chapter. The dotted line results from the values $\sigma_v = 5\,\%$ and $\sigma_\phi = 5\,°$, which is the maximum contamination that is used in the parameter studies in Section 5.6.3. It is seen that the former leads to really slight deviations $-0.2\,\text{dB} < \Delta L_{v,\text{input}}(x) < 0.2\,\text{dB}$, while the latter causes $-1\,\text{dB} < \Delta L_{v,\text{input}}(x) < 1\,\text{dB}$ almost without exception. The noise artefacts simulated in this chapter are therefore mostly small.

5.2 Error quantity definition

The *reconstruction error* is considered to be the deviation of the reconstructed velocity response from the true response. In the case of an infinite plate, the true response is obtained by the analytical solution given in Appendix D.1. In the case of the simply supported plate, the true response is obtained by the analytical solution given in Appendix D.3, whereas the true response of the free plate is assumed to be the solution obtained by FEM-analysis according to Appendix D.4. The reconstruction error is considered in terms of the level difference

$$\Delta L_v(x,y,\omega) = 10\log\Big|\frac{v_{\mathrm{rec}}(x,y,\omega)}{v_{\mathrm{sol}}(x,y,\omega)}\Big|^2, \tag{5.2.1}$$

where v_{sol} is the true velocity response and v_{rec} is the reconstructed velocity response. ΔL_v indicates the over- or underprediction of the true velocity at a specific point on the plate in decibels.

Part of the reconstruction error is a systematic computational error that occurs despite using uncorrupted input data. This will be referred to as *computational reconstruction error*. It is noted that in practice the different sources of error cannot be simply separated. It is difficult to evaluate different contributions to the total reconstruction error. If not differentiated specifically, in this thesis the term *reconstruction error* always refers to the total reconstruction error that is the result of all impairments.

A more general prediction of the reconstruction error is considered by means of the level difference of the spatially averaged square velocity

$$\Delta L_{\overline{v}}(\omega) = 10\log\Big|\frac{\overline{v^2_{\mathrm{rec}}(\omega)}}{\overline{v^2_{\mathrm{sol}}(\omega)}}\Big|, \tag{5.2.2}$$

with the mean square velocity

$$\overline{v^2(\omega)} = \frac{1}{N}\sum_{i=1}^{N} v_i^2(x,y,\omega). \tag{5.2.3}$$

The definition $\Delta L_{\overline{v}}(\omega)$ stems from the definition of the logarithmic radiation efficiency σ,

$$10\log\sigma = 10\log\frac{P(\omega)}{\rho_0 c S\overline{v^2(\omega)}} \tag{5.2.4}$$

that relates the radiated acoustic sound power P normalized by the characteristic acoustic impedance and the product of surface area and mean square velocity of the structure. $\Delta L_{\overline{v}}(\omega)$ therefore represents the level difference that would result if the radiation efficiency had been calculated using extrapolated instead of directly measured normal velocities.

5.3 Plate parameters

The material parameters of the simulated plates are chosen such that they correspond to the plates used in the experimental evaluation. The infinite case is investigated in the form of an acrylic plate whose material parameters are given in Table 5.1. For both the free and the simply suported finite case, an aluminum plate is chosen. The parameters of the aluminum plate are given in Table 5.2.

Table 5.1: Acrylic plate properties

thickness [m]	density [kg/m^3]	Young's modulus [N/m^2]	loss factor	Poisson's ratio
0.02	1150	$3.5{\cdot}10^9$	0.06	0.375

Table 5.2: Aluminum plate properties

thickness [m]	density [kg/m^3]	Young's modulus [N/m^2]	loss factor	Poisson's ratio	length [m]	width [m]
0.005	2810	$72{\cdot}10^9$	0.0001	0.31	1	1

5.4 Frequency representation

In many instances it is desirable to analyze acoustic spectra in terms of frequency. For airborne sound problems, frequency is a familiar quantity which can easily be related to the physics involved. Wave propagation is only marginally affected by changes in the medium. Given structure-borne sound problems, wave propagation is greatly affected by the material properties and the geometry of the structure. At any given frequency, plates of different material and thickness may exhibit a very different bending wavelength, wherefore a comparison in terms of frequency is not especially meaningful. In this thesis, spectra are therefore generally displayed in terms of the *number of bending wavelengths per unit meter* because the bending wavelength incorporates all the crucial physical parameters. In order to have a reference, Fig. 5.2 relates this quantity to the bending wavenumber and the frequency for the structures in question. For convenience, "number of bending wavelengths per unit meter" is abbreviated with "BWPM" in the text. In the figures with spectral plots, its dimension is labeled "[1]" because it constitutes a dimensionless quantity.

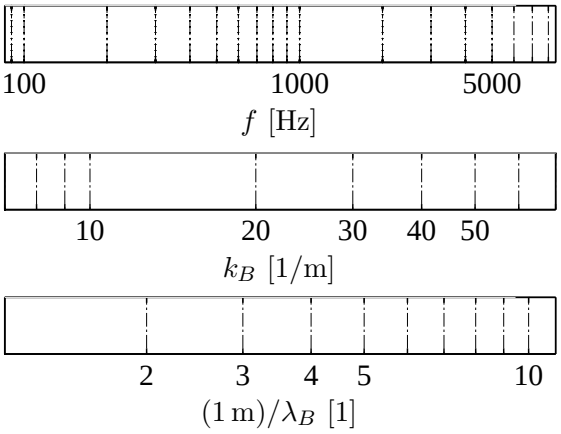

(a) acrylic plate, simple bending theory

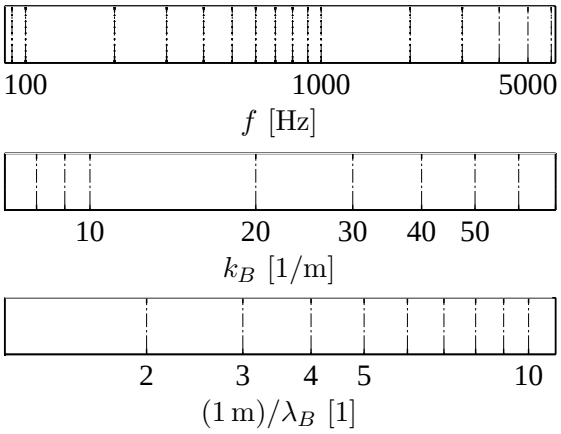

(b) acrylic plate, corrected bending theory

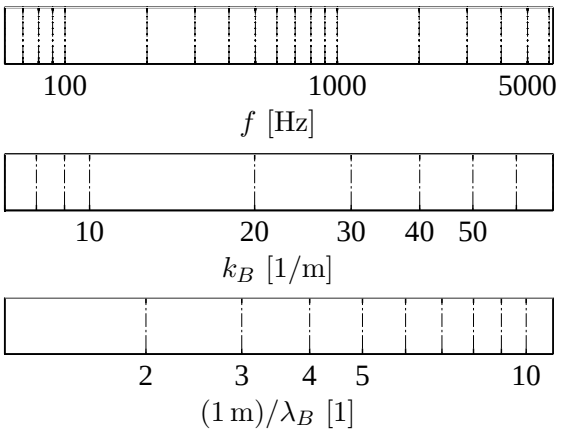

(c) aluminum plate, simple bending theory

Figure 5.2: Relation between frequency, bending wavenumber and bending wavelengths per unit meter in the considered frequency range.

5.5 Reference values

The following reference values are used in the calculation of the levels given in this thesis.

velocity	v_0=5·10^{-8} m/s
force	F_0=1·10^{-6} N
mechanical mobility	Y_0=5·10^{-2} m/Ns

5.6 Infinite plate

5.6.1 Simulation scenario

Following the geometry depicted in Figs. 3.3 and 4.6, the scenario under consideration consists of a fictitious source of normal point forces that act on an infinite acrylic plate. The driving forces differ in magnitude and phase but do not vary with frequency. The material parameters of the plate are given in Table 5.1. By applying a polar coordinate system, a circular contour of radius $r_0 = 0.16\,\mathrm{m}$ can be imagined to connect the excitation points. The default measurement parameters used in the simulations are listed in Table 5.3: the number of sampling points N along each hologram contour, the amount of noise through incorrect magnitude and phase σ_v and σ_ϕ, the standoff distances $d_{\mathrm{st},1}$, $d_{\mathrm{st},2}$, $d_{\mathrm{st,i}}$ and the contour distance Δr according to Figs. 3.3 and 4.6. Deviations from these parameters are explicitly declared in the captions of the corresponding figures. Standoff distances for NSBSH are initially chosen just less than a quarter of the wavelength that is found for the highest frequency considered, thus lying within the assumed near-field region. Input data is obtained by sampling the simulated plate response with $N = 48$ points along each hologram contour. For the considered frequencies the number is well above the limit dictated by Eq. (3.2.35). The total number of utilized sampling points for NSBSH is $N_{\mathrm{tot}} = 2N$ since two contour lines are required. For KHI, $N_{\mathrm{tot}} = 3N$. One contour determines the velocity, and two auxiliary contours are used to determine the corresponding normal gradient. The BEM-approach requires only a single contour to be measured, and therefore $N_{\mathrm{tot}} = N$.

Each sampled plate response is corrupted by very slight random error according to Section 5.1, whereby the values are assumed to fluctuate with the standard deviations $\sigma_v = 1\,\%$ and $\sigma_\phi = 1^\circ$ by default. The computations utilize the analytical solution to the problem of a thin infinite plate excited by normal point forces, given in Appendix D.1.

Table 5.3: Default simulation parameters for the infinite plate

	N	σ_v [%]	σ_ϕ [°]	$d_{\mathrm{st,1}}$ [m]	$d_{\mathrm{st,2}}$ [m]	$d_{\mathrm{st,i}}$ [m]	Δr [m]
NSBSH	48	1	1	0.015	0.03		
KHI	48	1	1			0.05	0.015
BEM	48	1	1			0.05	

5.6.2 Continuous spatial field reconstruction

First, the spatial reconstruction of a continuous field for the rather high frequency $f = 6820\,\mathrm{Hz}$, corresponding to BWPM = 10, is simulated. Figure 5.3 shows the continuous reconstruction of the real part of the spatial velocity field by means of the NSBSH-, KHI- and BEM-method compared to the analytical solution. With NSBSH and KHI, the characteristics and the strength of the field are accurately reconstructed, verifying the theory introduced for infinite plates. With BEM, the field strength is clearly underpredicted. The blank plate area in the plot is the field within r_0, beyond which propagation is invalid. For KHI and BEM which require sampling in the far-field, the blank plate area is larger than for NSBSH, naturally.

Fig. 5.3 is not well-suited to estimate the true accuracy of the procedure. From an engineering point of view, logarithmic quantities are preferred over linear quantities as they tend to be more revealing for data sets that cover a large range of magnitude. Therefore, in order to assess the reconstruction error, the level difference ΔL_v between reconstructed response and analytical solution is considered.

Fig. 5.4 shows the numerical error inherent in the implementation of the theory for infinite plates, given very slight noise contamination. In the case of NSBSH and KHI, the error most notably increases for those parts of the wave field that have a vanishing response. The BEM-method, on the other hand, fails because the number of sampling points N is too small. As is seen in Fig. 5.4d, increasing N to a large number lets the extrapolated solution converge.

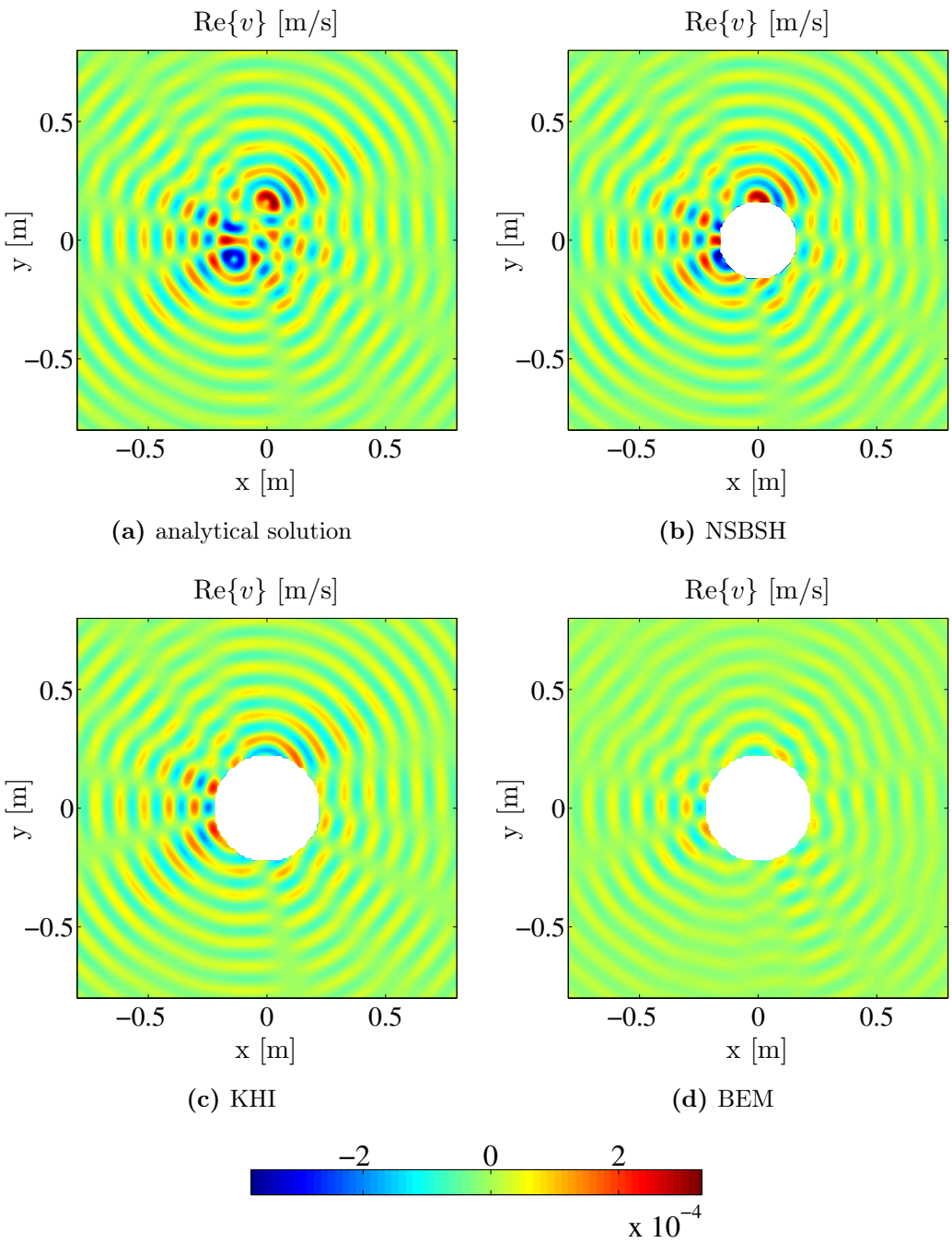

(a) analytical solution **(b)** NSBSH **(c)** KHI **(d)** BEM

Figure 5.3: Comparison of extrapolation methods on an infinite plate: simulated bending wave field, $f = 6820\,\mathrm{Hz}$ ($(1\,\mathrm{m})/\lambda_B = 10$).

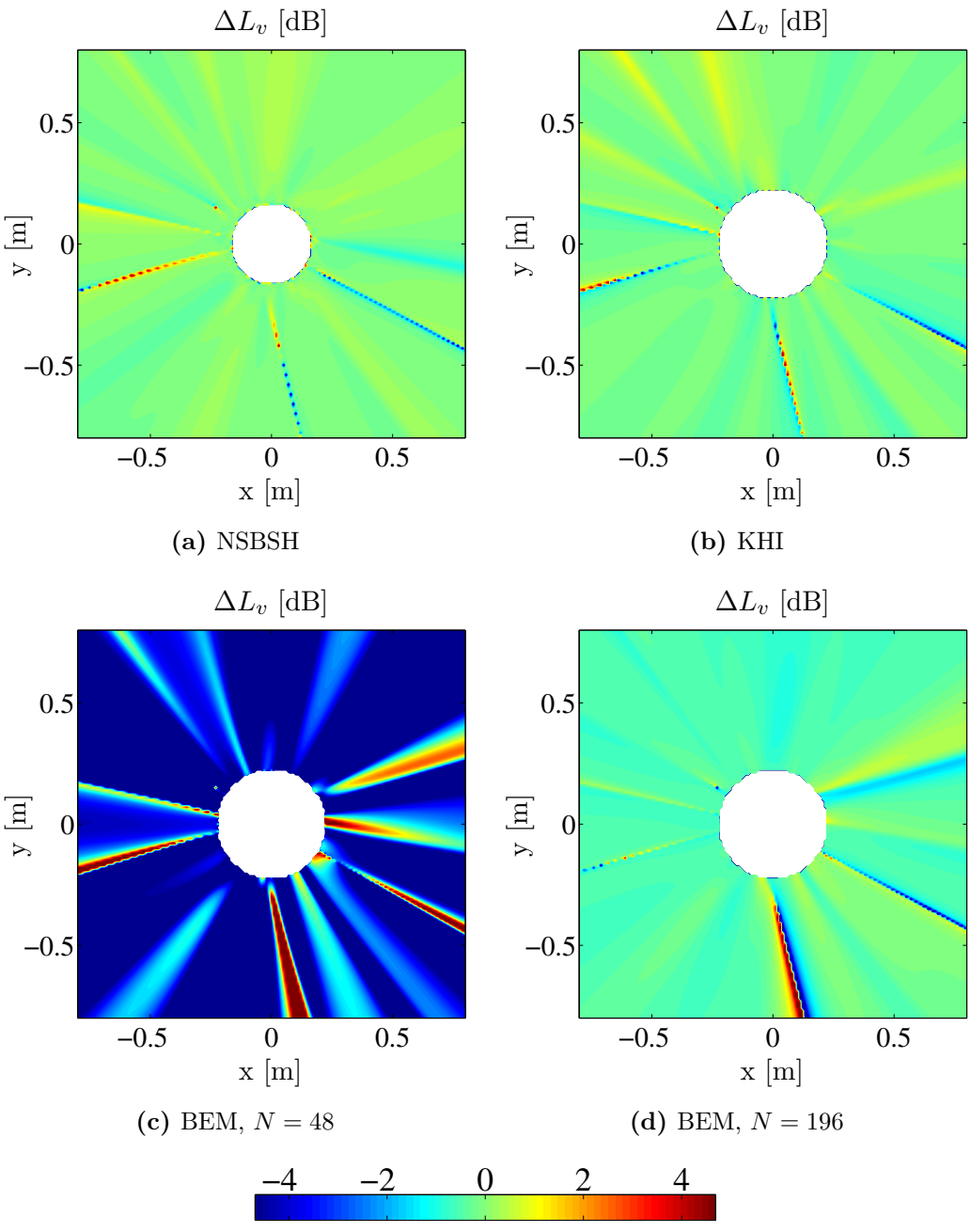

(a) NSBSH **(b)** KHI

(c) BEM, $N = 48$ **(d)** BEM, $N = 196$

Figure 5.4: Comparison of extrapolation methods on an infinite plate: simulated reconstruction error, $f = 6820\,\mathrm{Hz}$ $((1\,\mathrm{m})/\lambda_B = 10)$.

5.6.3 Spectral reconstruction and parameter studies

As a second step in the numerical evaluation, the reconstruction of response spectra at two arbitrary positions in the near- and far-field is simulated. The near-field position is one of the force positions. The far-field position is located at a distance of 0.8 m in radial direction. Reconstruction is performed while varying those measurement parameters that would be of immediate interest in practice: the number of sampling points, the standoff distance and the accuracy of the measured input data, i.e. the contamination by noise.

The first result adresses the supposed main attraction of NSBSH: the possibility to reconstruct the field at the source. Figure 5.5 compares backward-propagated spectra obtained through different possible implementations of NSBSH, as discussed in Chapter 3: straightforward reconstruction, wavenumber-filtered reconstruction and reconstruction based on a simplified formulation that neglects the near-field terms. It is apparent that backward-propagation is a very sensitive procedure. Even though measurement is taken at a close distance of only 0.03 m to the source, with just a little measurement noise of 1 %, straightforward reconstruction already displays over- and undershooting and therefore deviations up to 3 dB or more. It is not difficult to imagine that the reconstruction will fare much worse if these parameters are increased. The reason for this behavior is an overamplification of high wavenumber content, mostly determined by the highest order of the Hankel functions used in the mathematical formulation. The more sampling points, the higher the order of the functions involved and thus the more severe the problem. In this example, $N = 48$ sampling points per contour are used, which is more than twice the required amount.

As discussed in Section 3.9.1, this situation might be improved by applying a wavenumber-filter. The sensitivity to both measurement noise and standoff distance is thus significantly decreased. At low frequencies there is a uniform underprediction of the spectrum due to the choice of the filter parameters. The effect of different cut-off values for the filter is shown in Fig. 5.6. While a "generous" filter is helpful in preserving the low wavenumber-content that is important at low frequencies, it will allow overshooting at higher frequencies. Vice versa, an "aggressive" filter prevents overshooting at higher frequencies, but cuts too much of the low wavenumber-content. For this reason the filter cut-off should be chosen differently for different frequency regions. Accepting the underprediction at the low end of the spectrum, the cut-off value

$$n_c = 1.3 \cdot k_B r_{\max} = 2.6 \cdot \pi r_{\max}/\lambda_B \tag{5.6.1}$$

and the filter slope

$$\alpha = 0.1 \tag{5.6.2}$$

were found to give convenient results for an infinite plate in the considered frequency region. Ultimately, this amounts to a rather sharp filter whose width is

oriented by Eq. (3.3.12), with $r_{\max}$ being the radius of the largest hologram contour. The filter parameters were found empirically by comparing the results for different values of n_c and α at different frequencies in a couple of cases.

Using the simplified formulation for NSBSH stabilizes the results as well, although the correct spectrum is significantly overpredicted throughout. It will be seen that in practice the results for simplified backward-propagation are markedly different. It is noted that both wavenumber-filtering and the simplified formulation for NSBSH are only discussed in conjunction with backward-propagation. They are ineffective for (and rather detrimental to) propagation toward the far-field.

Figure 5.7 illustrates the effect of the number of sampling points N on the reconstruction error associated with forward-propagation, i.e. reconstruction of the far-field. NSBSH is thereby compared to the Kirchhoff-Helmholtz integral-based methods discussed in Chapter 4. The results for three different numbers N are plotted over the required number of sampling points N_{crit} according to the spatial Nyquist criterion, given by Eq. (3.3.12). For NSBSH and the direct KHI-approach, N_{crit} does indeed give a good estimate on how many sampling points to use. The curves indicate that accuracy is improved if more than N_{crit} sampling points are used. For the BEM-approach the number is not nearly enough, as is also seen in Section 5.6.2. It has to be noted that the BEM-implementation was kept most basic. Better results might be expected if a more sophisticated numerical implementation is chosen. In general, NSBSH is superior at reconstructing the low end of the spectrum. This is to be expected, seeing that the KHI-approach neglects the near-field that is spatially extended at low frequencies.

Figure 5.8 shows how the extrapolation methods handle varying amounts of measurement noise. NSBSH and KHI accept noise in about the same way, although NSBSH is more negatively afflicted if noise increases. BEM appears to be almost oblivious to these small increments in noise contamination. The magnitude of systematic error is relatively large to begin with, so that the additional random error does not change the result significantly. It is remarked that the simulated noise contaminations do not necessarily represent realistic situations. Under unfavorable practical conditions, even 5 % error in amplitude and in phase may be considered slight. As seen with backward-propagation, this can be enough to sink an inverse procedure, however.

In Fig. 5.9, different values for the standoff distance, i.e. the distance between hologram or boundary contour and source, are compared. Unlike backward-propagation, forward-propagation through NSBSH is basically unaffected by increasing standoff distances. The KHI-reconstruction improves with increasing distance from the source, as input data increasingly constitutes a pure far-field. The same should apply for the BEM-reconstruction, but the tendencies are hard to make out due to the larger systematic error.

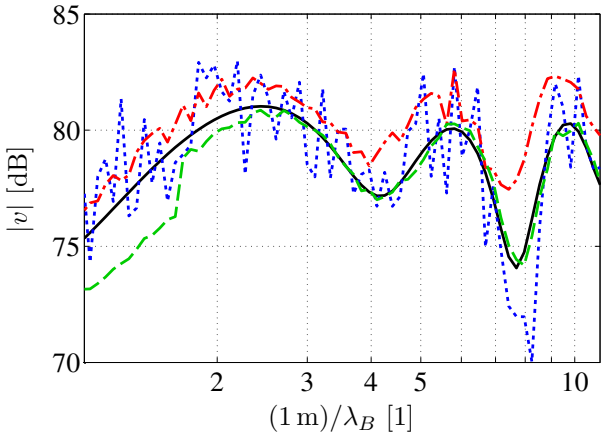

Figure 5.5: NSBSH, simulated backward-propagation on an infinite plate; $N = 48$, $d_{\mathrm{st},2} = 0.03\,\mathrm{m}$; ━━ analytical solution; ╍╍ wavenumber-filtered; ╍·╍ simplified formulation; ┅┅ straightforward implementation.

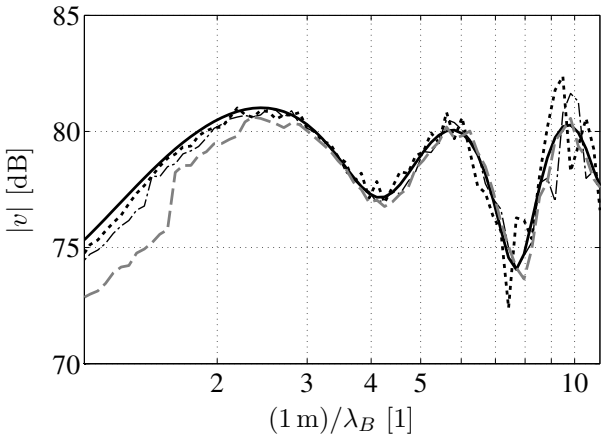

Figure 5.6: NSBSH, simulated backward-propagation on an infinite plate using different filter-cut-off values; ━━ analytical solution; ╍╍ $n_c = 1.3 \cdot k_B r_2$; ╍·╍ $n_c = 2 \cdot k_B r_2$; ┅┅ $n_c = 3 \cdot k_B r_2$.

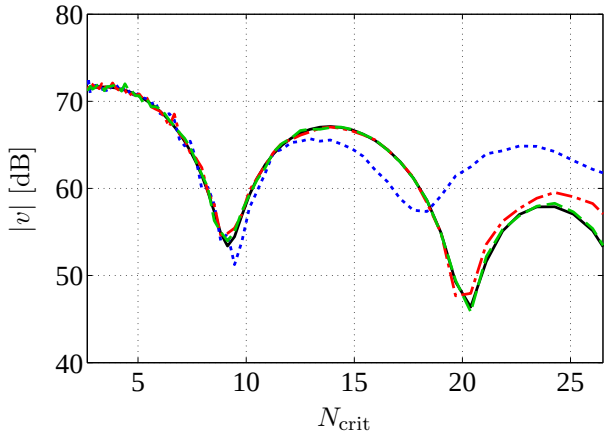

(a) NSBSH, $d_{\mathrm{st},2} = 0.03\,\mathrm{m}$

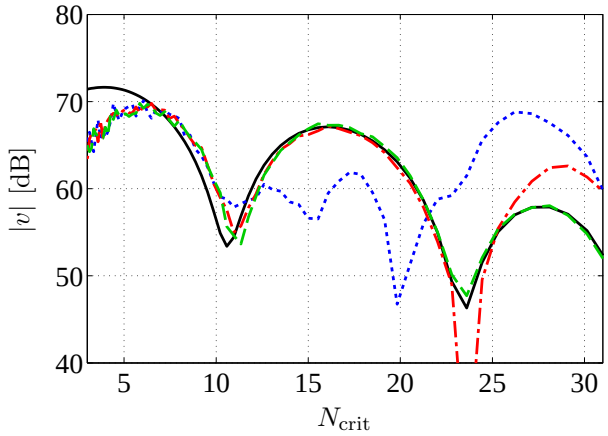

(b) KHI, $d_{\mathrm{st},0} = 0.05\,\mathrm{m}$

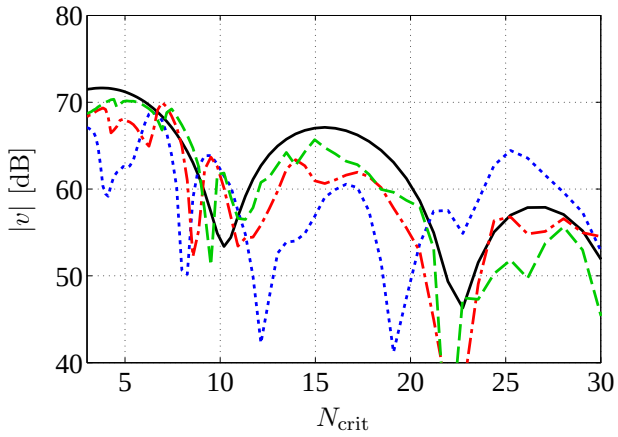

(c) BEM, $d_{\mathrm{st},0} = 0.05\,\mathrm{m}$

Figure 5.7: Comparison of extrapolation methods on an infinite plate: simulated reconstruction of a response spectrum for a varying number of sampling points; — analytical solution; - - $N = 48$; -·- $N = 24$; ···· $N = 12$.

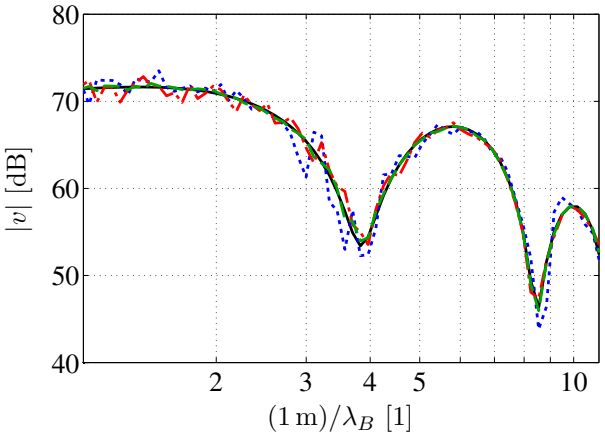

(a) NSBSH, $d_{\mathrm{st},2} = 0.03\,\mathrm{m}$

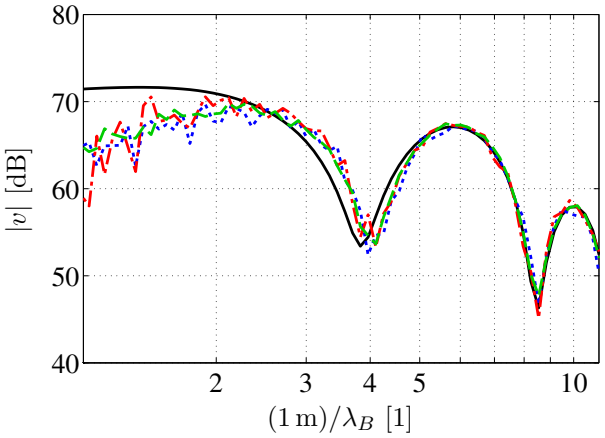

(b) KHI, $d_{\mathrm{st},0} = 0.05\,\mathrm{m}$

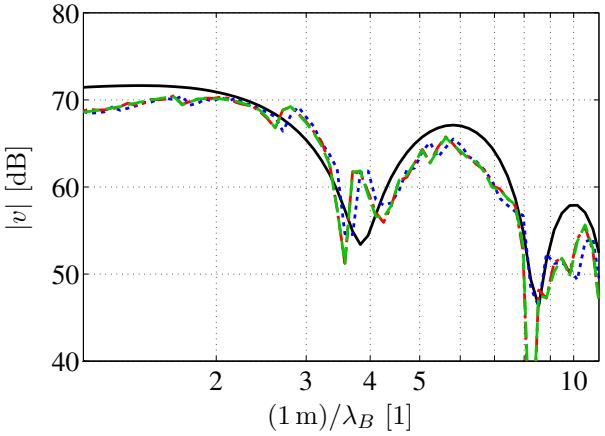

(c) BEM, $d_{\mathrm{st},0} = 0.05\,\mathrm{m}$

Figure 5.8: Comparison of extrapolation methods on an infinite plate: simulated reconstruction of a response spectrum for a varying amount of noise contamination; ━ analytical solution; ╍ $\sigma_v = 1\,\%$, $\sigma_\phi = 1\,°$; ┅ $\sigma_v = 3\,\%$, $\sigma_\phi = 3\,°$; ┈ $\sigma_v = 5\,\%$, $\sigma_\phi = 5\,°$.

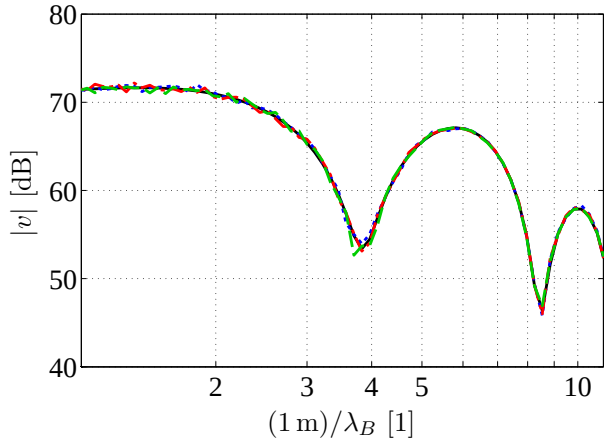

(a) NSBSH

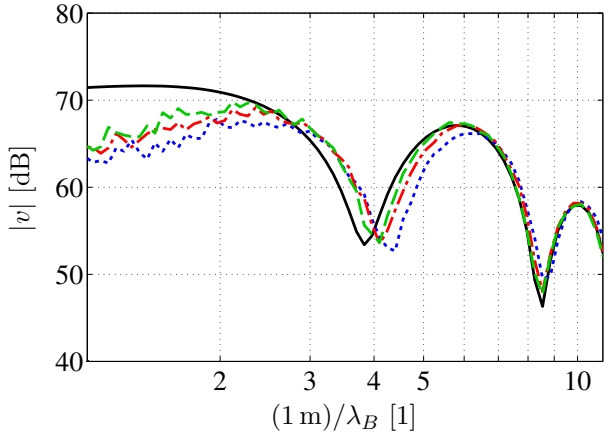

(b) KHI

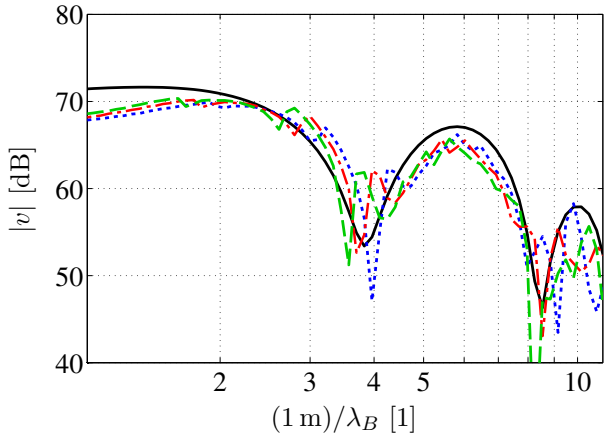

(c) BEM

Figure 5.9: Comparison of extrapolation methods on an infinite plate: simulated reconstruction of a response spectrum for varying standoff distances;
— analytical solution;
NSBSH: ····· $d_{\mathrm{st,2}} = 0.03\,\mathrm{m}$, -·-·- $d_{\mathrm{st,2}} = 0.045\,\mathrm{m}$, – – $d_{\mathrm{st,2}} = 0.06\,\mathrm{m}$;
KHI/BEM: ····· $d_{\mathrm{st,i}} = 0.03\,\mathrm{m}$, -·-·- $d_{\mathrm{st,i}} = 0.045\,\mathrm{m}$, – – $d_{\mathrm{st,i}} = 0.06\,\mathrm{m}$.

5.7 A quick look at the effect of structural discontinuities

If there is one restriction that keeps the theory discussed in this thesis from being practical, it is the requirement of homogenity and isotropy in the structure. In many engineering applications, plate structures have, by intention or not, discontinuities such as stiffeners, welding seams or holes. Any of these will lead to reflection and wave conversion to some extent, which of course is not accounted for by the free-field propagation functions utilized in this thesis. It is therefore obvious that extrapolation by NSBSH and KHI must fail when structural discontinuities are presented. Nevertheless, it is not quite clear how or to which extent. An engineer might ask whether slight impedance differences, e.g. small obtrusions in the plate, can be tolerated as long as the resulting reconstruction error remains negligible. In order to comment on the severity of the restriction, the case of an infinite plate with discontinuities will be briefly examined.

The infinite plate discussed in Section 5.6.2 will now be simulated to be stiffened in x-direction. Four small beams of the same material are connected to the plate at a distance of 0.4 m. The beam width is identical to the thickness of the plate, and the height is 2.5 times the thickness of the plate. The physical model that is used to calculate the plate responses is obtained by using a simplified force substitution approach, presented in [73]. Since the model considers coupling at discrete points only, the distance between the coupling points along each beam was chosen smaller than $\lambda_B/4$ in order to approximate a line connection. The utilized equations for the plate response are given in Appendix D.2.

The results in Fig. 5.10 feature the magnitude of the normal velocity instead of the real part. The magnitude represents the actual vibratory response that would be determined by sensors in practice and is better suited to analyze the field distribution of a plate with discontinuities. The obtained results are very clear. Even with these arguably slight discontinuities, the methods are doomed to fail completely. It is seen that the true response is quite intricate. The section enclosed by the inner beams exhibits the highest magnitude because the excitation points lie within that section. The adjacent sections are characterized by a significantly weaker but modal field due to the insulating effect of the stiffeners. Outside these sections, the field vanishes. The extrapolation fails to resolve any of this. A higher magnitude along the inner section of the plate is predicted because this is where the measurements yield the largest values, but nothing else is.

It must be concluded that any repeated obstruction, even a slight one, will render the extrapolation methods unusable. A slight damage or a small punctuation may not affect the results too much (in fact, the plates used for the experimental evaluation are a little battered), but any significant discontinuity will mean that NSBSH or KHI in their considered form cannot be used.

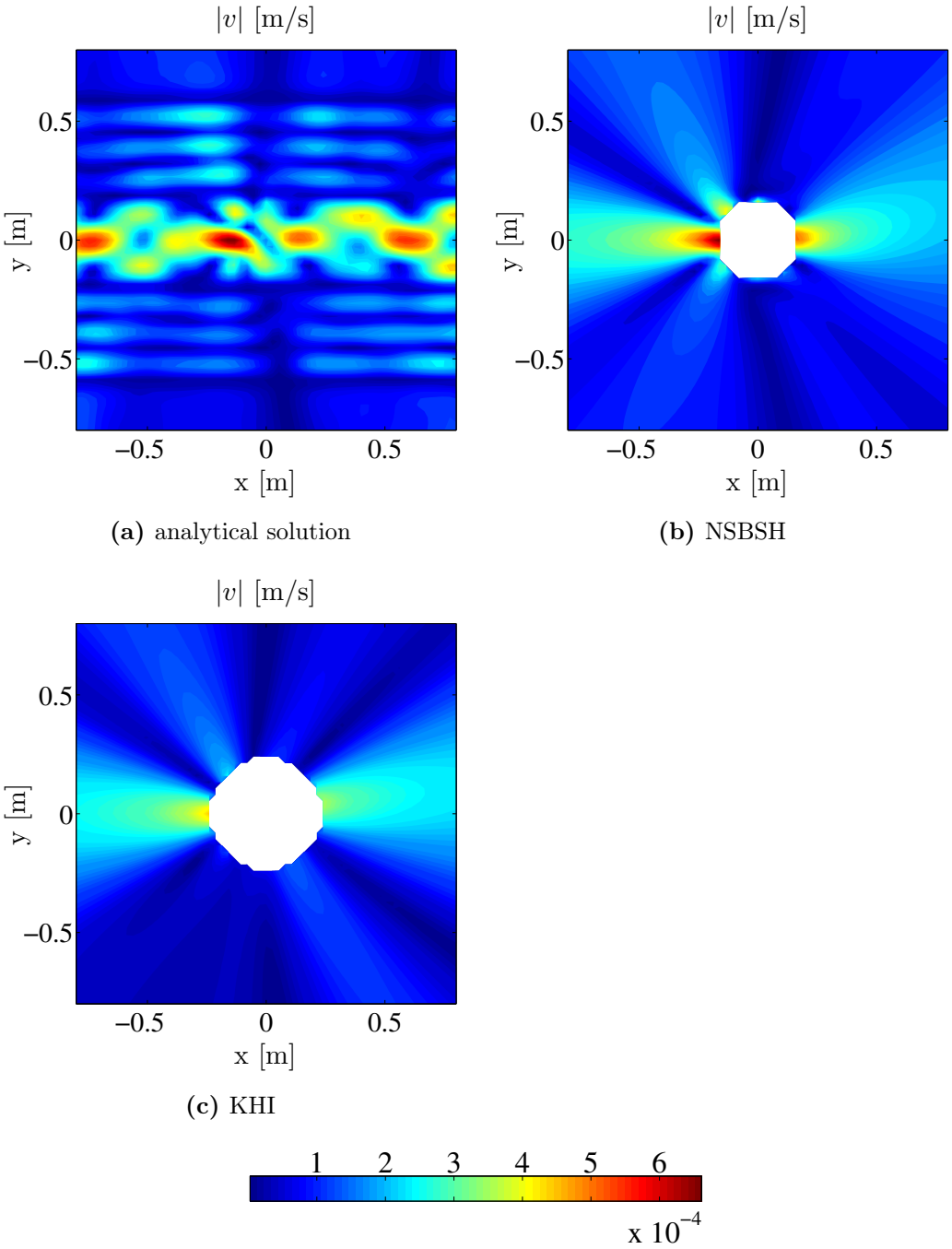

(a) analytical solution

(b) NSBSH

(c) KHI

Figure 5.10: Comparison of extrapolation methods on a stiffened infinite plate: simulated bending wave field, $f = 1233\,\mathrm{Hz}$ ($(1\,\mathrm{m})/\lambda_B = 4.2$).

5.8 Free plate

5.8.1 Simulation scenario

Corresponding to the geometry in Figs. 3.4 and 4.7, the scenario under consideration consists of a fictitious source of normal point forces that act on a square aluminum plate. The plate exhibits a free boundary condition, i.e. vanishing force and moment, all around. By applying a polar coordinate system, a circular contour of radius $r_S = 0.08\,\mathrm{m}$ can be imagined to connect the force positions. The forces differ in magnitude and phase but do not vary with frequency. The material parameters of the plate are given in Table 5.2. For both NSBSH and KHI the number of sampling points used along the inner and outer hologram or boundary contour is referred to as N_i and N_e. The simulated measurement parameters are listed in Table 5.4. Those parameters that determine the distances of the measurement contours are depicted in Figs. 3.4 and 4.7. The required plate response data is obtained by an FEM-solution to the problem of a completely free plate excited by a set of normal point forces.

Table 5.4: Simulation parameters for the free/simply supported plate

	N_i	N_e	σ_v [%]	σ_ϕ [°]	$d_{\mathrm{st},1}$ [m]	$d_{\mathrm{st},2}$ [m]	$d_{\mathrm{st},3,\mathrm{min}}$ [m]	$d_{\mathrm{st},4,\mathrm{min}}$ [m]
NSBSH	36	72	1	1	0.005	0.02	0.005	0.02
KHI	36	100	1	1				

	$d_{\mathrm{st,i}}$ [m]	$d_{\mathrm{st,e}}$ [m]	Δr [m]
NSBSH			
KHI	0.04	0.04	0.02

5.8.2 Continuous field reconstruction

First, the spatial reconstruction of a continuous field for $f = 439\,\mathrm{Hz}$ (BWPM = 3) is simulated. Fig. 5.11 shows the continuous reconstruction of the spatial field by means of NSBSH and KHI compared to the FEM-solution. While the real part of the normal velocity was used to show the propagation of waves in an infinte plate in Section 5.6.2, the magnitude is chosen when finite plates are considered. Although the magnitude cannot show the phase relations within a modal pattern, i.e. whether the mode shapes bend in positive or negative normal direction, it has a clear physical meaning because it represents the actual vibratory response that is

determined by sensors in practice. NSBSH allows measurement in the near-field, hence the smaller "restricted" area at the center of the plate. Apparently, the field is reconstructed very well where it can be reconstructed. Unfortunately, the restriction to hologram contours in polar coordinates means that the field cannot be reconstructed toward the corners of the plate. A conformal geometry would not pose a problem for the KHI-method if there was no strong near-field at the edges of the plate. This is exactly the case, however, and so the reconstruction by means of KHI fails. At this frequency, the chosen distance from the plate edge $d_{\mathrm{st,e}}$ is not enough to warrant the far-field assumption, resulting in a severely overpredicted magnitude. In order to get reasonable results one would have to move further away from the plate edges, thereby obliterating the main advantage of KHI vs. NSBSH in this scenario.

The situation changes if high frequencies, e.g. $f = 3123\,\mathrm{Hz}$ (BWPM = 8), shown in Fig. 5.12, are considered. Now the response calculated via KHI shows a very good agreement with the true response, while NSBSH leads to a complete blow-up close to the inner hologram contours and a worse result in general. Focusing on the upper right part of the field in Fig. 5.12b, it is observed that the reconstructed field pattern is inaccurate and that the magnitude of the "antinodes"[1] tends to be too high. The blow-up is a numerical but systematic effect. It was found that if the inner and outer boundary contours are separated by a distance d_{span} that approaches $3\,\lambda_{\mathrm{B}}$, the calculations closest to the inner contour escalate. It has to be noted that this value has been concluded empirically and therefore must not hold up if the simulation parameters are changed significantly. The error can occur for very different condition numbers and despite uncontaminated input data but is strongly related to the parameter d_{span} that informs the system of equations of course. The error can be removed by choosing a sharper wavenumber-filter for the inner field points, as seen in Fig. 5.12c. Using a cut-off value that is now differentiated,

$$n_c = \begin{cases} 1.3 \cdot k_B r_{\max}, & \sqrt{x^2+y^2} \leq 0.16\,\mathrm{m} \\ 0.9 \cdot k_B r_{\max}, & \sqrt{x^2+y^2} > 0.16\,\mathrm{m} \end{cases}, \tag{5.8.1}$$

the results are stabilized. This kind of filtering is still simplistic and would probably need to be investigated further if the method was extended to deal with more complicated scenarios.

It is concluded that NSBSH on finite plates inherits instabilities at high frequencies or for large geometrical dimensions, which requires further stabilization measures compared to the simpler infinite case. Problematic behavior at high frequencies is not surprising for inverse procedures of this sort. If the plate response is dominated by modes, equidistantly sampled responses are not independent anymore. This has also proven problematic in FR-techniques, e.g. [74]. Looking at

[1] It is acknowledged that the terms "node" and "antinode" are usually only used given pure modes or standing waves. Here, they shall also refer to peaks or lows if the field is not purely modal.

the corresponding reconstruction error across the plate, shown in Fig. 5.13, two further observations are made. It is confirmed that the greatest error tendentially occurs where the smallest responses have to be predicted. It is also seen that at high frequencies NSBSH is obviously prone to higher error in general. This is not a consequence of numerical instability because the condition number does not depend on the measured responses. Also, it will be seen that the simply supported plate shows much less reconstruction error at the same frequency. This is an error in the physical model. The Hankel functions that were derived as eigenfunctions for the governing differential equation can be likened to decaying cosine or sine functions. It was merely assumed that a superposition of these functions can be used to represent solutions for plates in polar coordinates in general. However, it is known that sine functions do not represent suitable eigenfunctions that can be summed up to build an analytical solution for a plate with free boundary conditions. For this reason the assumption is just not very good. The assumed physical model is only an approximation, and in the case of free boundaries the approximation does not come too close, obviously. On the other hand, the error seems to come from a shifted field rather than from absolute miscalculation, wherefore the results from extrapolation may still be considered very tolerable.

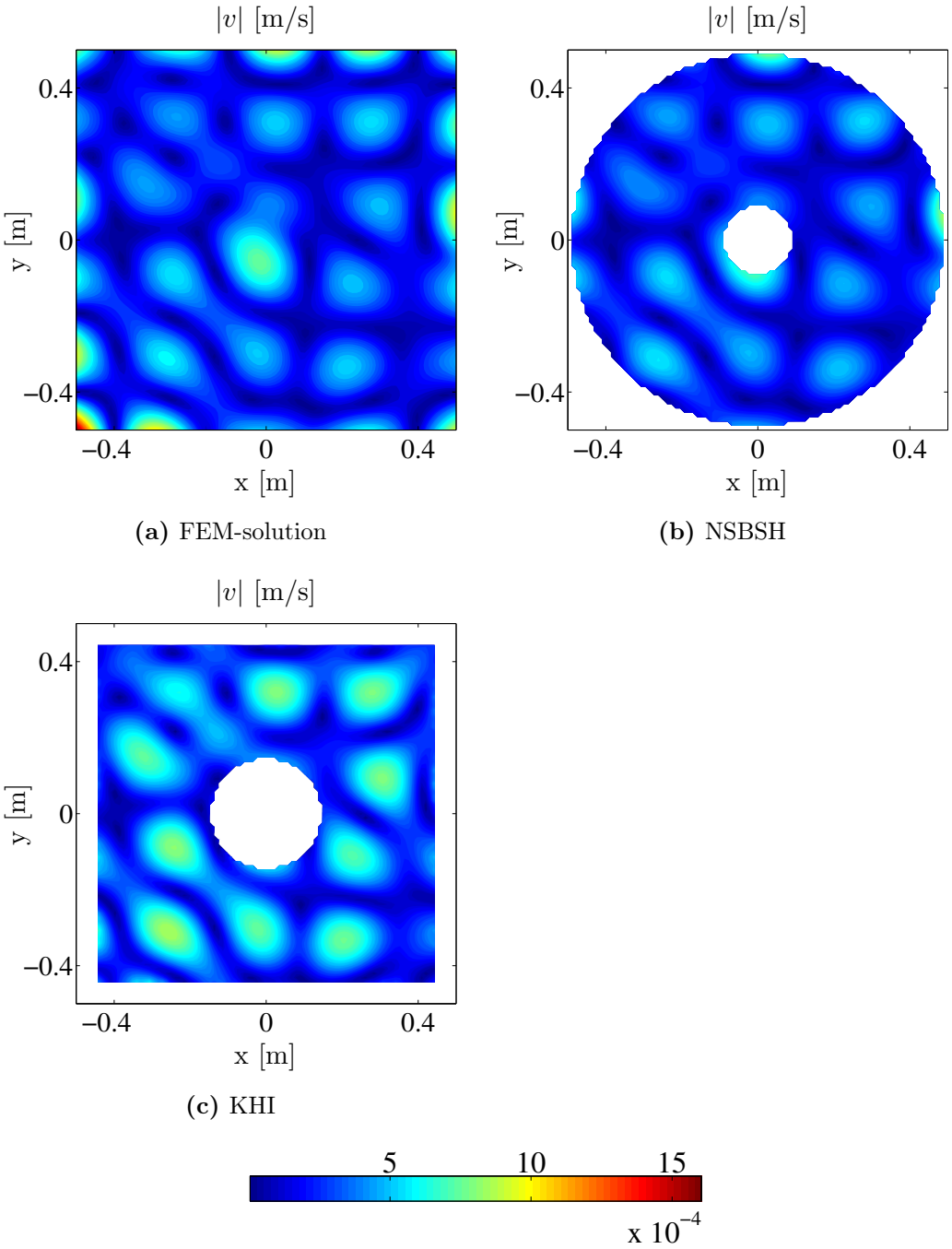

(a) FEM-solution

(b) NSBSH

(c) KHI

Figure 5.11: Comparison of extrapolation methods on a free plate: simulated bending wave field, $f = 439\,\mathrm{Hz}$ ($(1\,\mathrm{m})/\lambda_B = 3$).

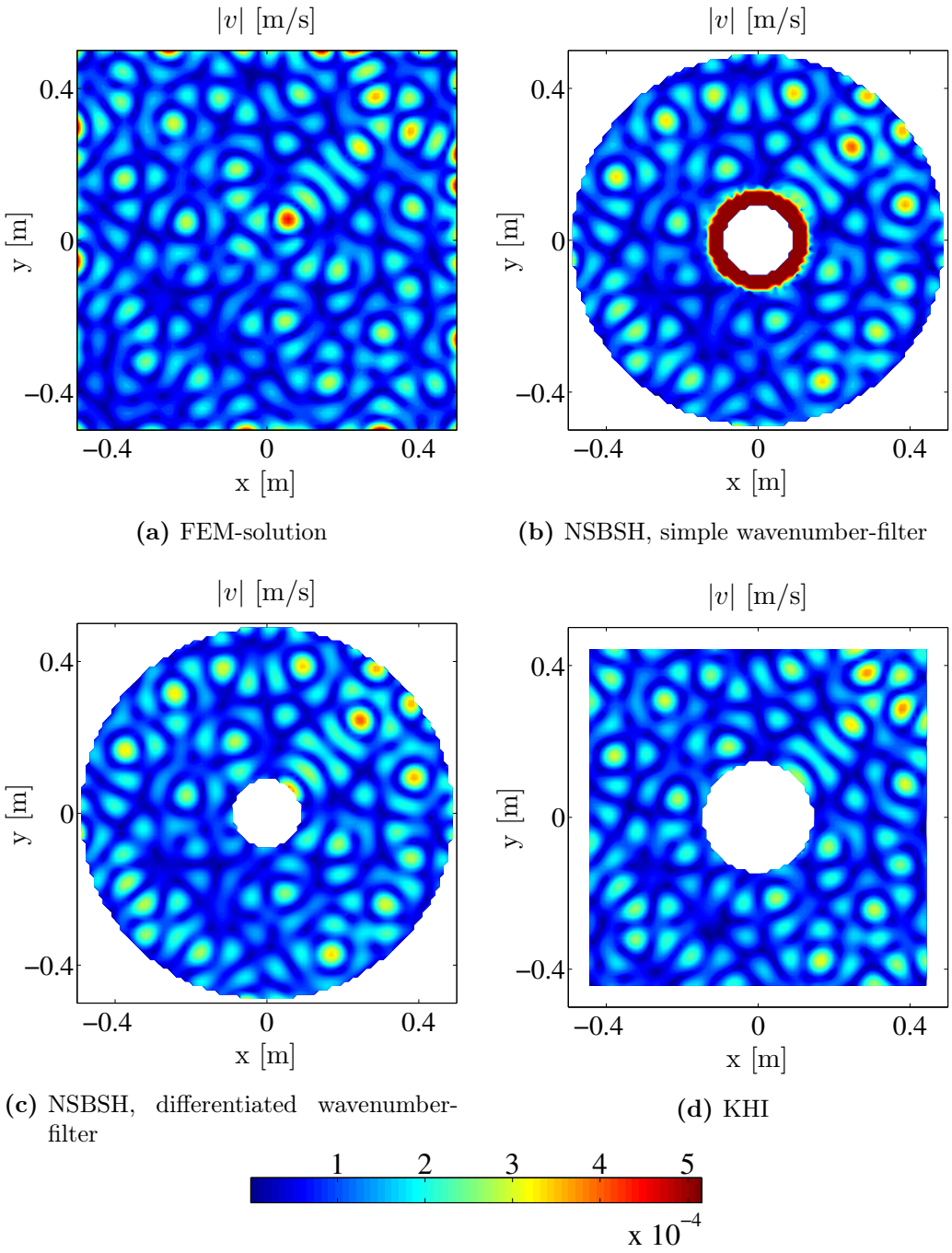

(a) FEM-solution

(b) NSBSH, simple wavenumber-filter

(c) NSBSH, differentiated wavenumber-filter

(d) KHI

Figure 5.12: Comparison of extrapolation methods on a free plate: simulated bending wave field, $f = 3123\,\mathrm{Hz}$ ($(1\,\mathrm{m})/\lambda_B = 8$).

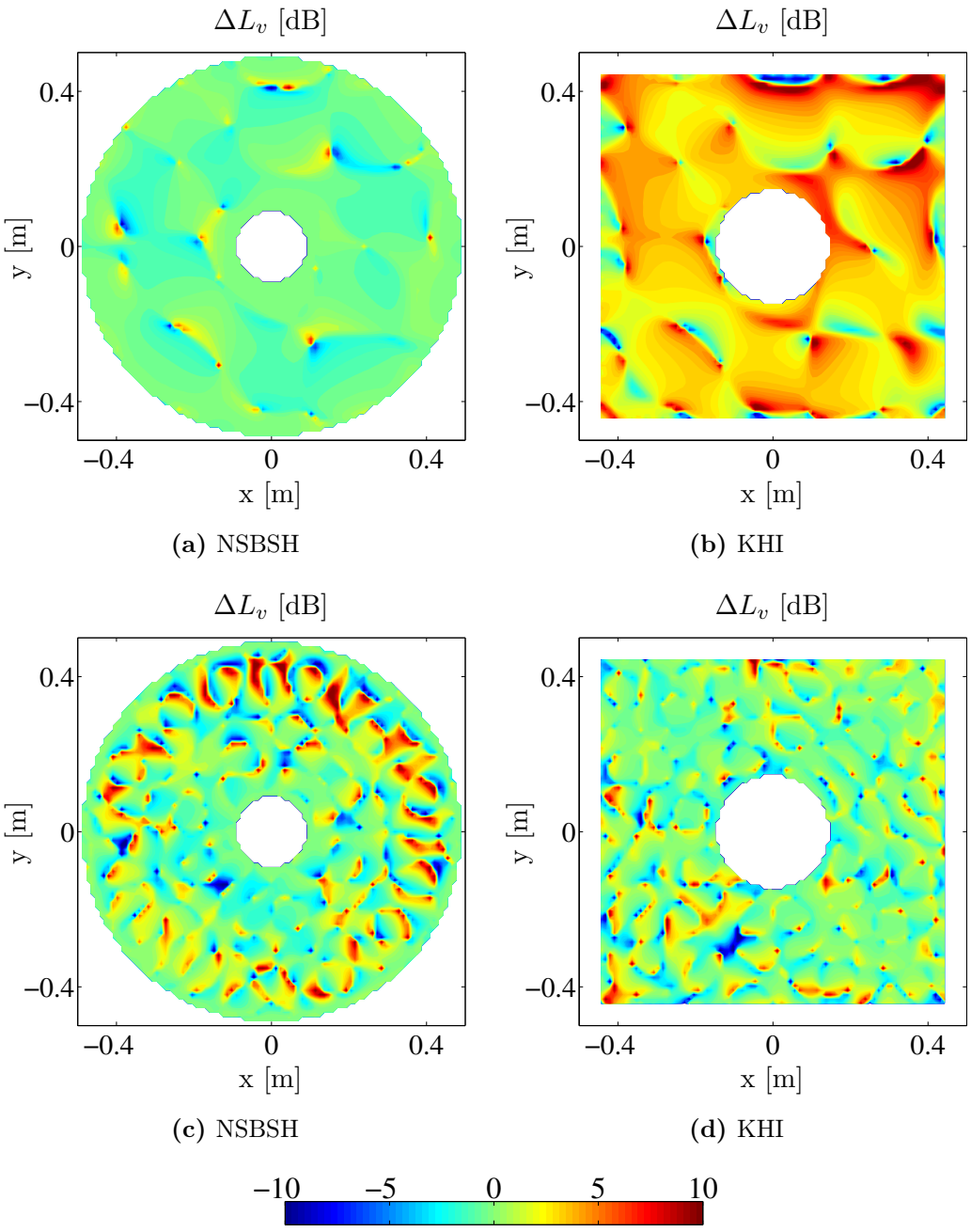

Figure 5.13: Comparison of extrapolation methods on a free plate: simulated reconstruction error; a), b) $f = 439\,\mathrm{Hz}$; c), d) $f = 3123\,\mathrm{Hz}$.

5.8.3 Spectral reconstruction

In many instances the acoustic engineer will be primarily interested in the response spectrum at a specific location first and foremost. Exemplarily, the reconstruction of a spectrum is performed at the position $x = 0\,\mathrm{m}$, $y = 0.3\,\mathrm{m}$. The results obtained through NSBSH and KHI are compared in Fig. 5.14, in which the findings in the previous section are confirmed. At lower frequencies the KHI-method consistently overpredicts the plate response because the supposed measurement contours are effectively placed within the near-field region. Deviations can amount to 5 dB or even more. Comparing the distance from the edge $d_{\mathrm{st,e}} = 0.04\,\mathrm{m}$ to the number of bending wavelengths per unit meter BWPM ≈ 4 at which the overprediction subsides, indicates that the critical distance for far-field conditions is $d_{\mathrm{st,e}} \approx \lambda_B/7$. To be safe, the measurement contours should therefore be placed at a distance of at least $\lambda_B/6$ from the discontinuities (the plate edges or the points of excitation) generating the near-field. This is less than the distance assumed from literature discussed in Section 3.7.

Dealing with low frequencies is the strong suit of NSBSH. Because it includes the near-field, the results are especially accurate in the lower frequency range. It is seen that NSBSH can work well despite ill-conditioning, at least given a low amount of measurment noise. Most importantly, it is seen that it can be used for spectral reconstruction despite relying on approximative functions that form the physical model. It does not fall apart at high frequencies. In practice, the problems discussed in Section 5.8.2 should lead to larger reconstruction errors, given higher uncertainties in the measurement.

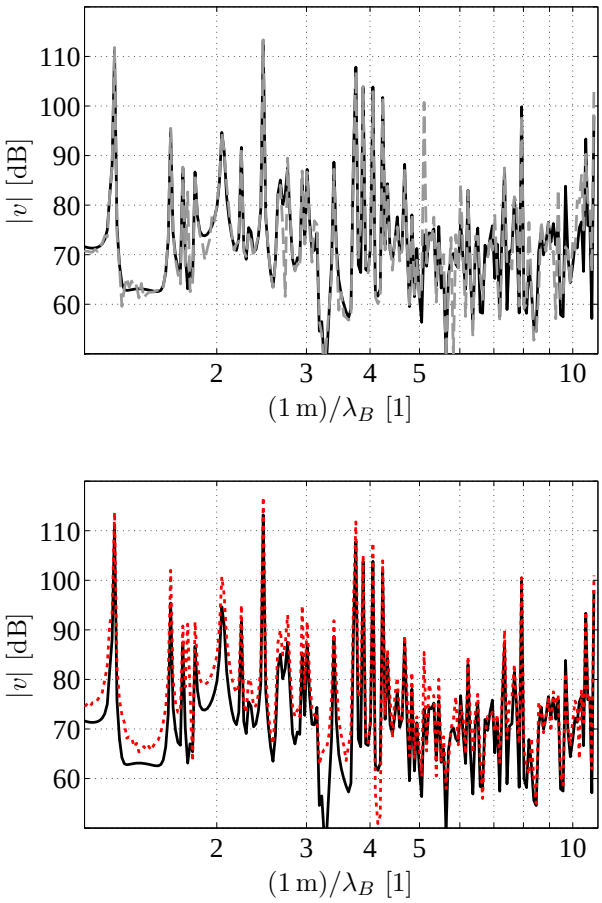

(a) NSBSH

(b) KHI

Figure 5.14: Comparison of extrapolation methods on a free plate: simulated reconstruction of a response spectrum; ━━ FEM-solution; ╌╌ NSBSH; ┅┅ KHI.

5.9 Simply supported plate

5.9.1 Simulation scenario

The simulated scenario for the simply supported plate is identical to that of the free plate described in Section 5.8.1, except for the boundary condition. Now a "simple support" is imposed all around, meaning that there is zero velocity and moment along the four edges. Since there is a well-known analytical solution to the problem, given in Appendix D.3, no FEM-computation is necessary in order to calculate the required input data.

5.9.2 Continuous field reconstruction

The frequency $f = 439\,\text{Hz}$ (BWPM = 3) is considered once more. In Fig. 5.15 the analytical solution for the corresponding normal velocity field is compared to the reconstruction via NSBSH and KHI, while the resulting error is displayed in Fig. 5.17. In this scenario, KHI works just as well as NSBSH, disregarding the general difference of the extrapolatable area. The simply supported boundary condition prohibits the existence of a structural near-field, and as a consequence the outer measurement contours are necessarily located in the far-field. In the case of finite plates, NSBSH does not require the existence of a near-field so much as it can utilize it. Either way, the reconstruction error obtained through NSBSH is found to be significantly smaller than for the free plate. The sine-like Hankel functions are very well suited to describe this boundary condition, and thus the physical model for wave propagation is very accurate.

The problems of NSBSH at high frequencies, reported in Section 5.8.2, were found for the simply supported plate as well. The instabilities are thus confirmed to be rooted in the model used for extrapolation since they do not vanish by changing to a "friendlier" boundary condition. Luckily, they can therefore be eliminated in the same way.

5.9.3 Spectral reconstruction

Analogous to Section 5.8.3, the reconstruction of a response spectrum is presented in Fig. 5.18. Here, the position x=0 m, y=0.25 m is considered. In terms of accuracy, NSBSH remains the superior method. Because of the simply supported boundary condition, KHI comes very close nevertheless. It is seen that KHI has more trouble predicting the exact magnitude of velocity at low levels. A reconstruction error of 5 dB or more is not a rare sight, especially at low frequencies. Besides that, both methods work similarly well.

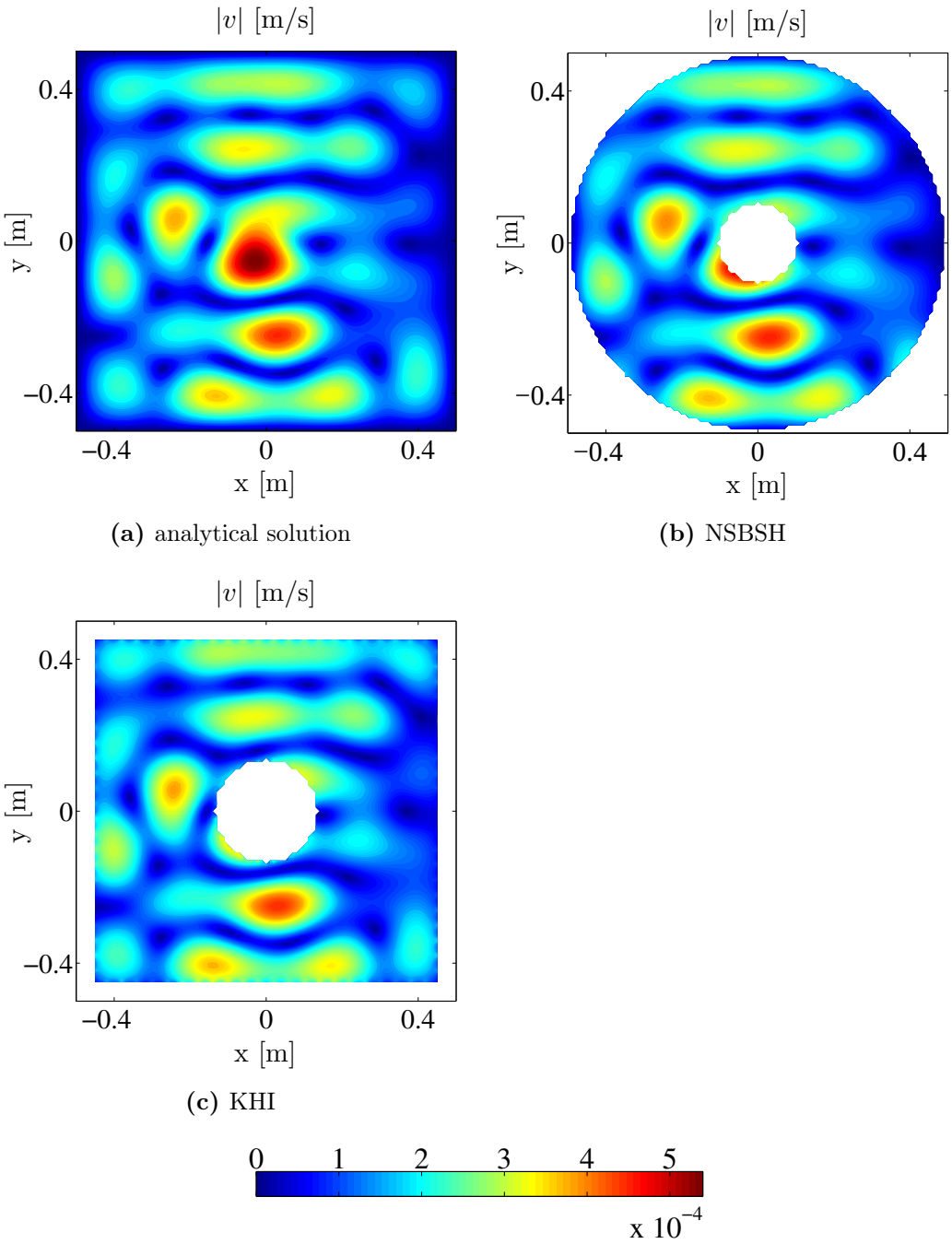

(a) analytical solution

(b) NSBSH

(c) KHI

Figure 5.15: Comparison of extrapolation methods on a simply supported plate: simulated bending wave field, $f = 439\,\mathrm{Hz}$ ($(1\,\mathrm{m})/\lambda_B = 3$).

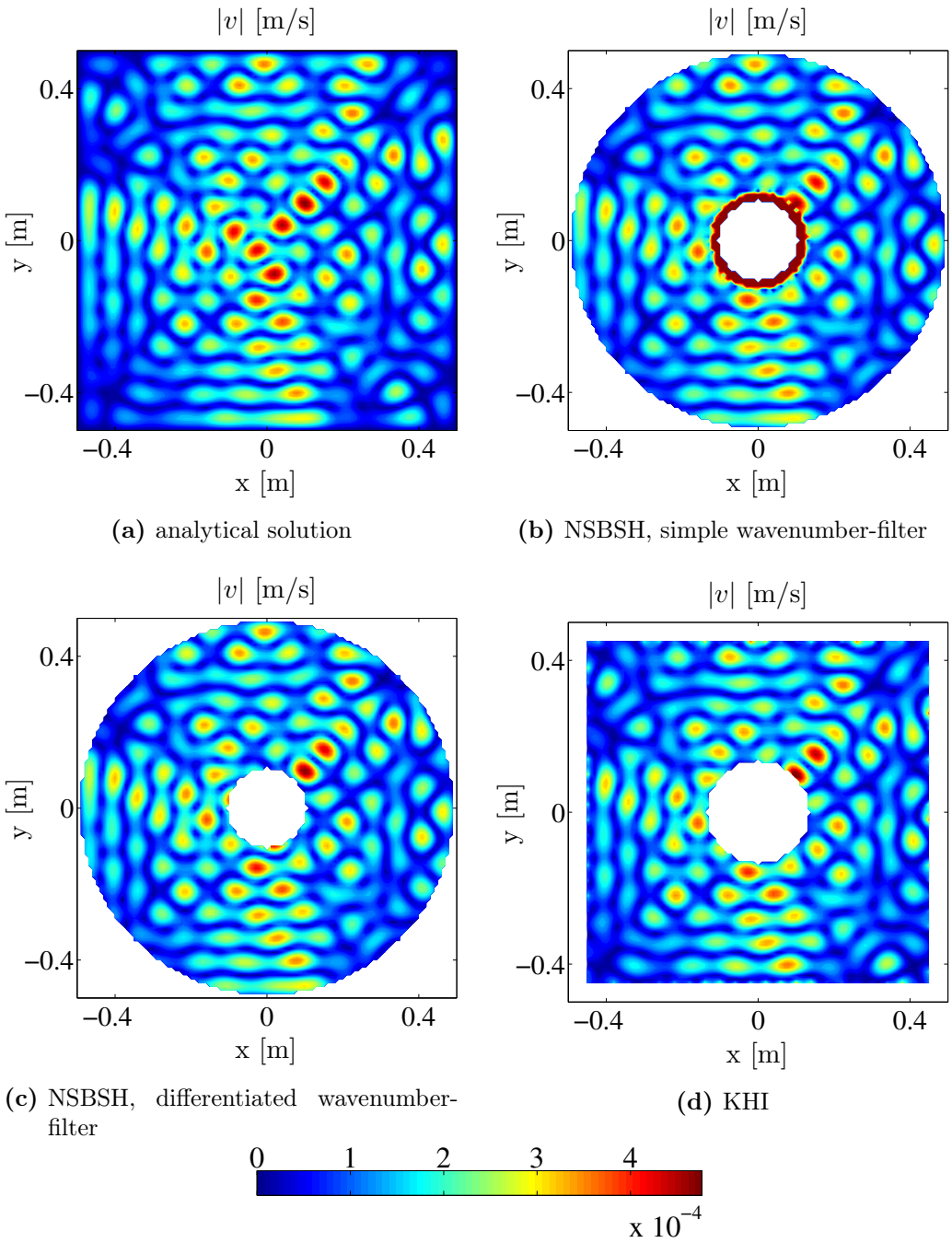

(a) analytical solution

(b) NSBSH, simple wavenumber-filter

(c) NSBSH, differentiated wavenumber-filter

(d) KHI

Figure 5.16: Comparison of extrapolation methods on a simply supported plate: simulated bending wave field, $f = 3123\,\mathrm{Hz}$ ($(1\,\mathrm{m})/\lambda_B = 8$).

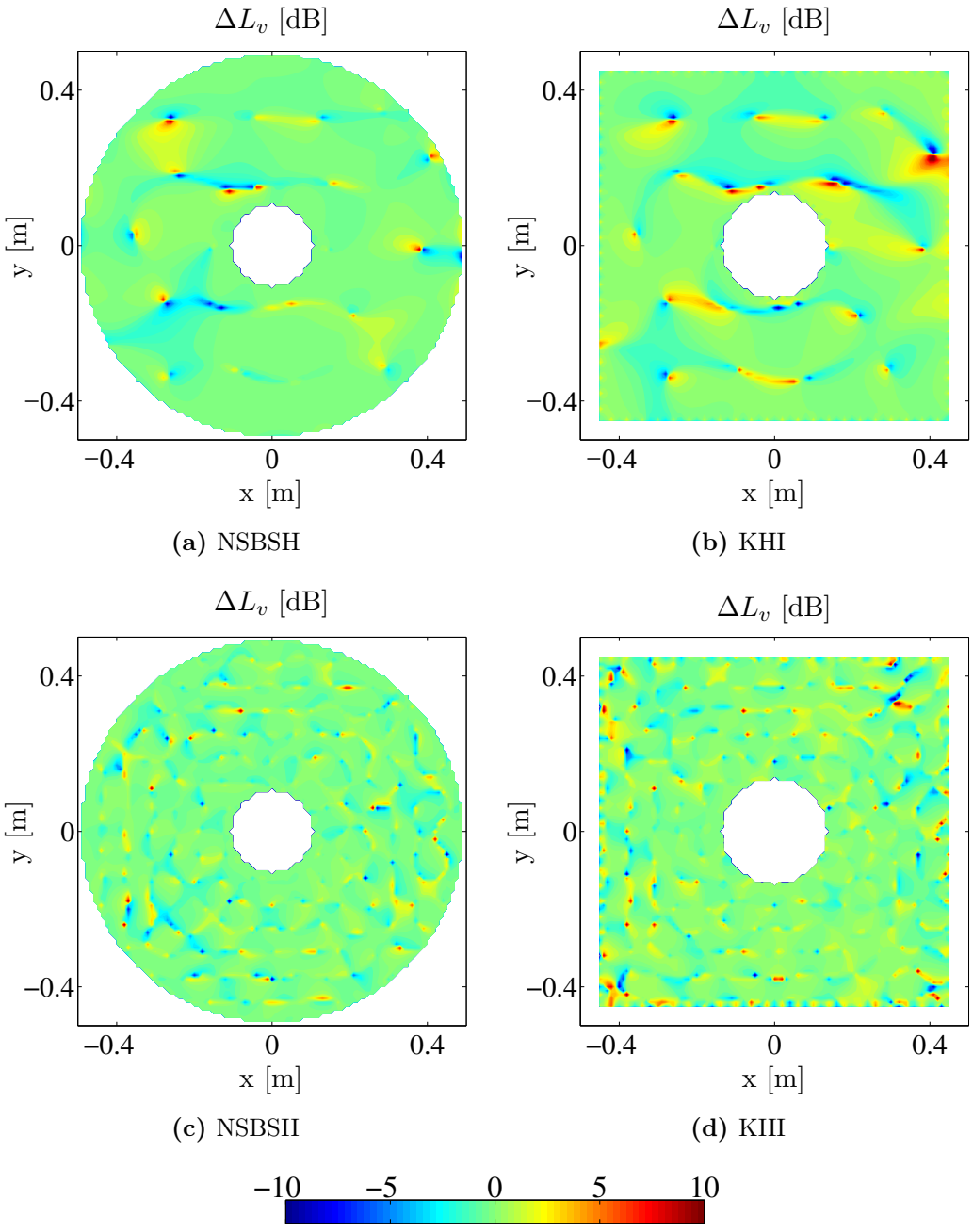

Figure 5.17: Comparison of extrapolation methods on a simply supported plate: simulated reconstruction error; a), b) $f = 439\,\mathrm{Hz}$; c), d) $f = 3123\,\mathrm{Hz}$.

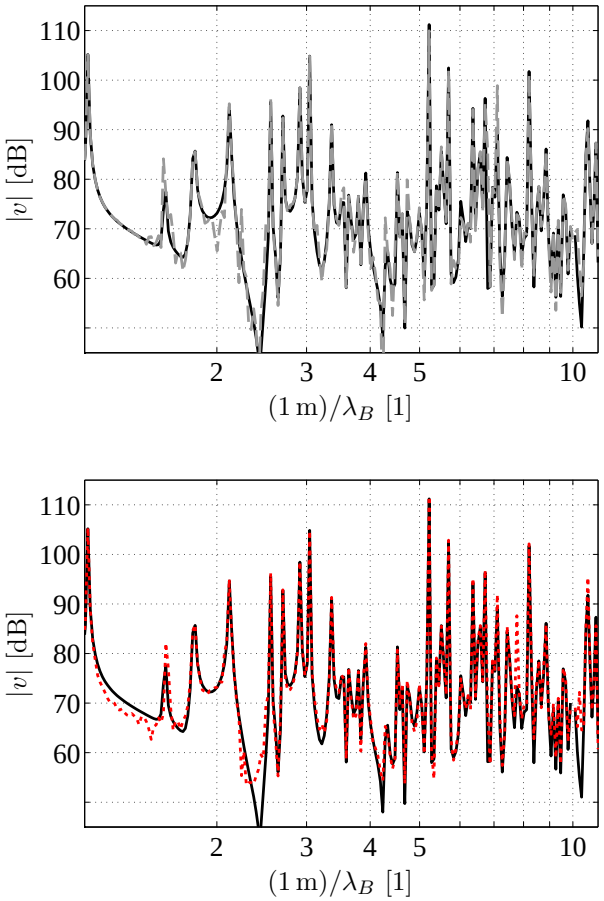

(a) NSBSH

(b) KHI

Figure 5.18: Comparison of extrapolation methods on a simply supported plate: simulated reconstruction of a response spectrum; ——— direct measurement; – – – NSBSH; ····· KHI.

5.10 A quick look at arbitrary geometry and mixed boundary conditions

The finite plates considered so far have been highly symmetric as far as geometry and boundary conditions are concerned, but the presented theory does not require such structural symmetry. In fact, symmetric plates are not necessarily easier to deal with. They lead to highly symmetrical mode shapes at the eigenfrequencies, which in turn may lead to ill-conditioned matrices in NSBSH where the sampling points are aligned symmetrically and spaced equidistantly. In order to demonstrate that both methods can handle irregularly shaped plates, Fig. 5.19 presents a FEM-based simulation for a semi-skewed plate with mixed boundary conditions.

The edges leading in x-direction are clamped, while the edges in y-direction remain free. Three arbitrary point forces are applied within the blank circular area in the center. Both methods, within their confines, reproduce the true field very well. It can be seen that the radius of the inner hologram contours for NSBSH had to be slightly increased in order to maximize the extrapolatable area. Still, a substantial area of the plate remains "out of reach" for NSBSH.

In the case of KHI, the only downside is that it is a little more complex to implement the calculation of the Kirchhoff-Helmholtz integral due to the angles involved. In practice, this would correspond to a more difficult arrangement of the measurement points. It is easy to see that a laser scanning system becomes a necessity if complicated contours have to be sampled in a reasonable amount of time.

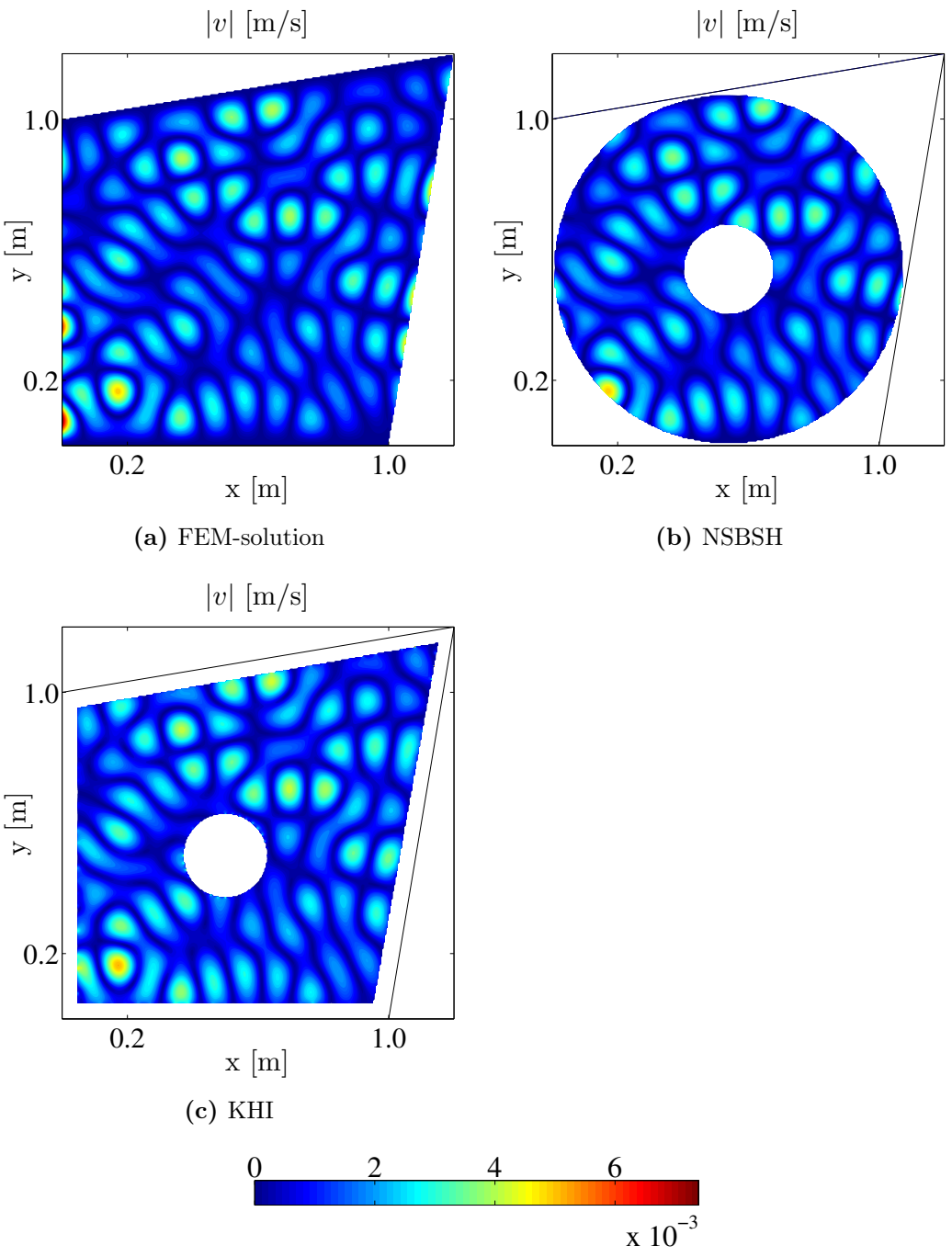

(a) FEM-solution

(b) NSBSH

(c) KHI

Figure 5.19: Comparison of extrapolation methods on a plate with arbitrary geometry and mixed boundary conditions,
$f = 1530\,\mathrm{Hz}$ $((1\,\mathrm{m})/\lambda_B = 5.6)$.

5.11 Conclusions

The developed theory was clearly confirmed. The extrapolation of a stationary bending wave field can be performed using the presented approaches adapted from the airborne sound domain.

It was demonstrated that the structural near-field can indeed be included if the Fourier transform-based holographic method NSBSH is applied. Doing so comes with costs, however. Besides the limitations imposed by theory, the method requires substantial numerical stabilization. The utilized filter and regularization parameters were found from empirical analysis of the results. The cut-off value for the filter $n_c = 1.3 \cdot k_B r_{\max}$ was thus found to give quite good initial results overall, while a constant regularization parameter $\lambda = 1.5 \cdot 10^{-3}$ was found to be suitable. A serious issue was encountered in the case of finite plates, for when the distance between inner and outer hologram contour approaches $3 \cdot \lambda_B$. The results near the inner contour blow up completely, which appears to be a systematic issue, not necessarily correlated with high condition numbers. The error was found to be removed if a sharper wavenumber filter with the cut-off value $n_c = 0.9 \cdot k_B r_{\max}$ was used within the affected plate area. This behavior suggests that a more refined stabilization strategy might leave room for improvement and would probably be required if the method was extended to deal with more sophisticated scenarios. Regardless of numerical aspects, the utilized propagation functions were shown to be a good fit for the simply supported boundary condition but were found to be rather approximative when it comes to the free boundaries. With the latter, continuous reconstruction of the spatial field exhibits a significant reconstruction error at high frequencies, probably due to a spatial shift of the calculated field compared to the true solution. The error is not that noticeable in the spectral reconstruction, however.

True backward-propagation toward the source, only possible in the infinite case to begin with, was found to work only with very small standoff distances, which suggests that it might not be worth the trouble in practice.

The Kirchhoff-Helmholtz integral-based far-field method KHI was found to perform very reliably overall. In general the simulations suggest that the corresponding measurements should be taken at a distance of $\lambda_B/6$ from structural discontinuities for the near-field-related reconstruction error to vanish. The BEM that was implemented for the infinite case proved to be the least accurate of the presented methods. In order to obtain results that truly converge to those of NSBSH and KHI, the number of sampling points per contour has to be quadrupled in comparison. Both NSBSH and KHI were shown to become accurate if the number of sampling points per contour is chosen a bit higher than the value dictated by the spatial Nyquist criterion.

The results suggest the arguably obvious: The far-field approach should be favored when dealing with high frequencies or boundary conditions devoid of near-fields, and the near-field approach vice versa.

6
Experimental evaluation

In this chapter, the proposed methods are validated through a set of experiments that mirror the scenarios considered in Chapter 5: an infinite plate and plates with free and simply supported boundary conditions, excited by stationary point forces. Array-type measurements from either accelerometers or laser vibrometers are used to reconstruct the continuous bending wave field as well as response spectra. The author has used some of the results for NSBSH on infinite plates in a previous publication [38]. The accompanying discussion also comments on the feasibility of the methods. The chapter concludes with a summarizing comparison of the theoretical and practical reconstruction error, allowing a conclusion regarding the overall accuracy that can be expected in practice.

6.1 Infinite plate

6.1.1 Setup

The procedures presented for infinite plates are validated by three experiments, using a large acrylic plate. They will be referred to as *experiment A*, *B* and *C*. In each experiment a different type of excitation is applied, referred to as *source A*, *B* and *C*. Acrylic exhibits fairly high structural damping compared to common industrial materials like steel or aluminum, which makes it better suited to approximate the condition of a structure-borne free-field. In order to further this condition, the plate is bedded on foam and embedded in sand along its edges, so that the given discontinuity in terms of the mechanic impedance difference is reduced. The plate is shown in Fig. 6.2, and its material properties are given in Table 5.1. While it is impossible to fully satisfy the condition of infinity in practice, a reasonable approximation may be sufficient. Figure 6.1 therefore compares the measured point mobility at the center of the plate to the analytical value for an equivalent infinite plate, which is known to be independent of frequency. As is to

be expected, the approximation is less successful at low frequencies, at which the modal behavior is not significantly affected by structural damping. The resulting unwanted peaks subside quite quickly as the frequency increases, giving way to a substantial part of the spectrum for which the plate can be assumed to be infinite. At high frequencies the mobility deviates from theory again because the mechanical system is affected by the measurement setup: an accelerometer mounted through wax and a shaker that is adding its full mass to the plate, as seen in Fig. 6.2f. The plate can therefore be considered to be reasonably "infinite". It is noted that this condition will be increasingly violated toward the edges of the plate, which is why the investigation will be restricted to the central plate area.

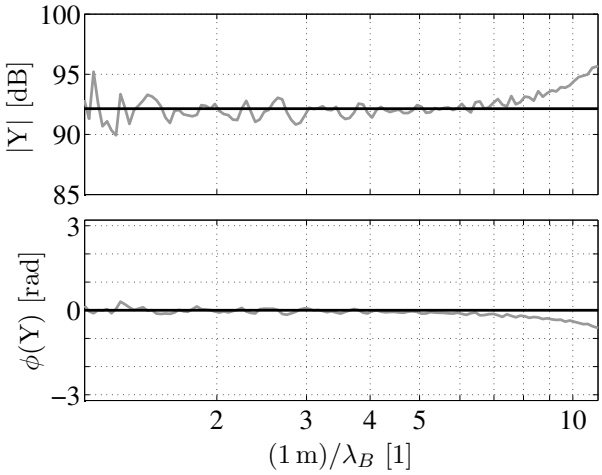

Figure 6.1: Point mobility at the center of the acrylic plate; ——— analytical solution; ——— measurement.

The different source types used in the experiments are shown in Fig. 6.2. Source type A consists of a shaker mounted off-center onto a circular structure with four feet, fed by random noise. Force transducers are used as feet, small enough in dimension as to exert point excitation for the frequency region under consideration. The source is simply set up on the plate without any kind of rigid connection. In order to simulate a scenario with higher structure-borne sound power, source B represents a modification of source A. Two shakers are mounted onto the same structure. In order to increase structure-borne sound transmission, the force sensors are glued to the plate using two-component adhesive, thereby establishing a reasonably rigid connection. Source C simulates a source with diverse driving forces. It is comprised of two pairs of shakers, rigidly connected to the plate using two-component adhesive. Each shaker pair is fed by distinct band passed random noise, and each shaker is driven by a separate amplifier. In this way the plate is subjected to four clearly differentiated excitations. The resulting driving forces in all experiments are displayed in Fig. 6.3.

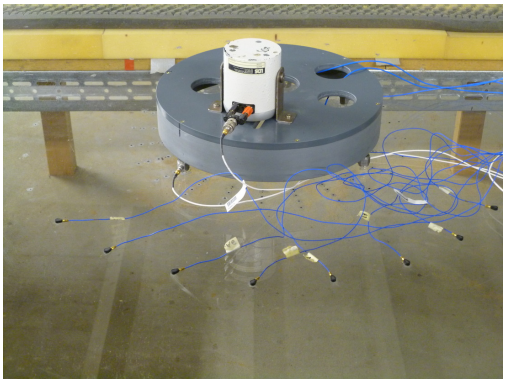

(a) experiment A: source and far-field measurement positions

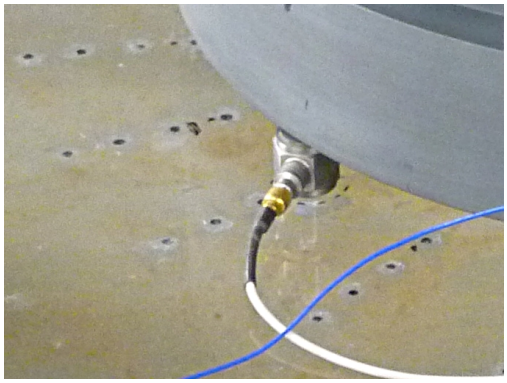

(b) experiment A: near-field measurement positions

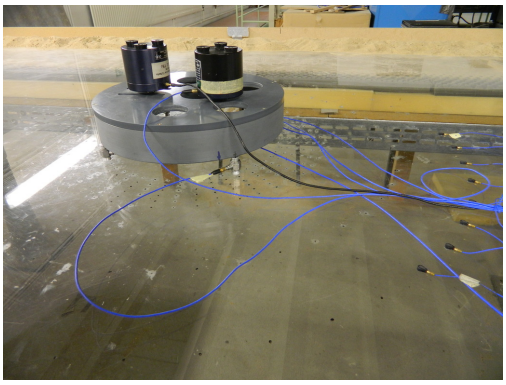

(c) experiment B: source and far-field measurement positions

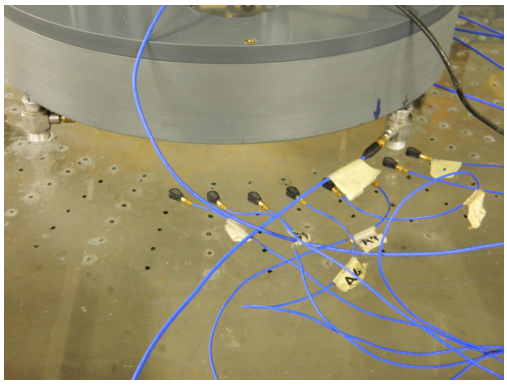

(d) experiment B: accelerometers, source mounting;

(e) experiment C: source and acrylic plate setup

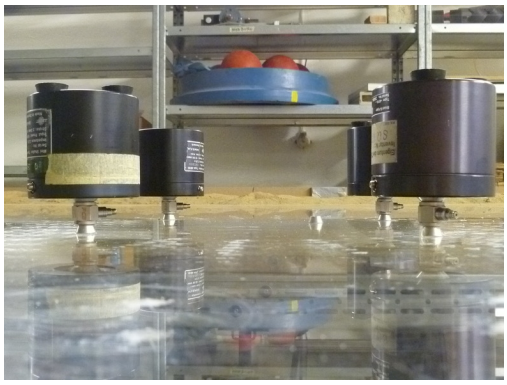

(f) experiment C: source mounting

Figure 6.2: Infinite plate experiments: detail views of the measurement setups.

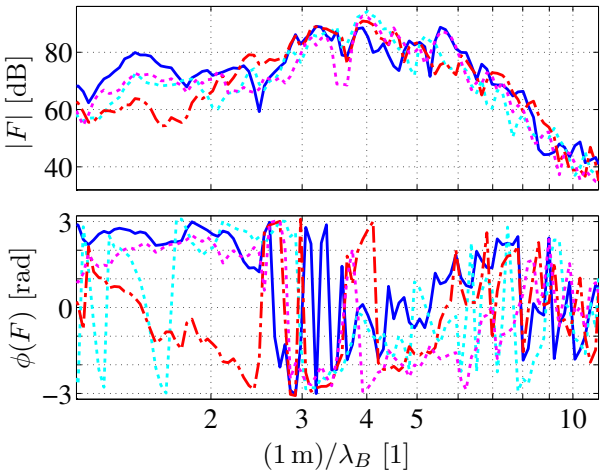

(a) experiment A

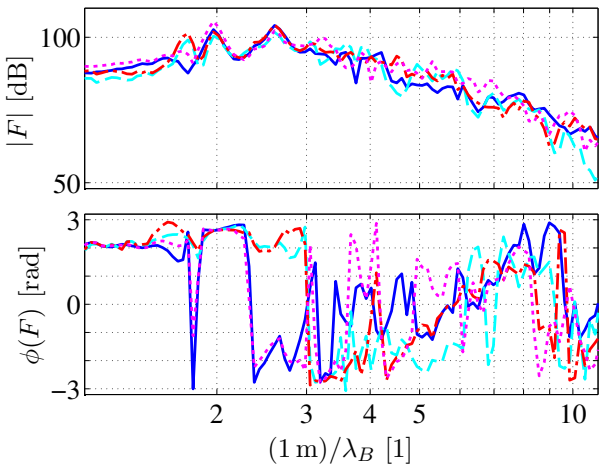

(b) experiment B

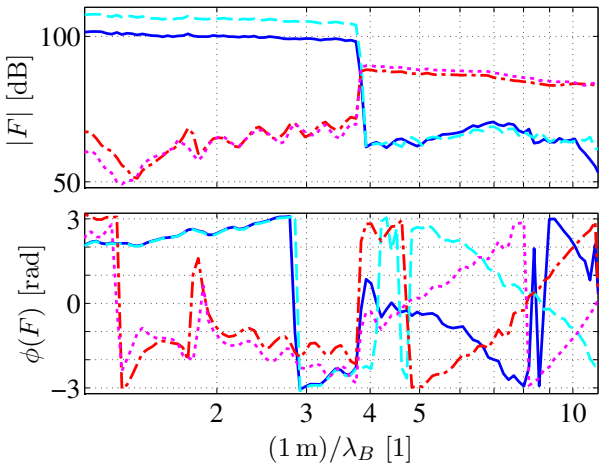

(c) experiment C

Figure 6.3: Forces applied to the infinite plate.

The required spatial velocity distributions are obtained by accelerometer measurement. As depicted in Fig. 6.4, two contours with twenty-four sampling points in the assumed near-field are used to perform NSBSH. Three far-field contours are sampled in order to perform KHI. Only one such contour is required for the BEM-approach. For KHI and BEM, twenty-four sampling points per contour are used in experiment C, while experiment B is performed with both twenty-four and forty-eight points per contour for comparison. In all cases, an additional fixed reference point is used to calculate phase information by means of the respective cross spectra. An overview of the default measurement parameters is given in Table 6.1. Deviations from these parameters are explicitly given in the captions of the corresponding figures.

Table 6.1: Default measurement parameters for the infinite plate

	N	$d_{\mathrm{st},1}$ [m]	$d_{\mathrm{st},2}$ [m]	$d_{\mathrm{st,i}}$ [m]	Δr [m]
NSBSH	24	0.015	0.03		
KHI	24			0.045	0.03
BEM	24			0.045	

6.1.2 Spectral reconstruction

The experimental evaluation for the infinite plate consists of the reconstruction of velocity response spectra at arbitrary positions in the near- and far-field of the source, shown in Fig. 6.4. The letters A, B and C denote experiment A, B and C, respectively. In order to sample the measurement contours, a number of miniature accelerometers are used, as shown in Fig. 6.2d. Given the setup of the plate, positioning each sensor manually is somewhat inconvenient and time consuming. It is for this reason that continuous spatial field reconstruction is not evaluated in the infinite plate experiments. In order to reproduce the wave field clearly at intermediate or high frequencies, a dense grid of response positions is required. Without a suitable laser scanning system to be be installed either above or below the "sandbox", sampling such a grid would become very inconvenient. Instead, it is chosen to investigate a few isolated response positions only. It is noted that the chosen far-field positions are not located very far from the sources, so that that the free-field condition can be assumed in good faith.

Each backward-propagated near-field spectrum is reconstructed by using the complete formulation of NSBSH as well as its simplified formulation. While in experiment A the corresponding measurement contours are located in the very near-field only, experiments B and C allow to compare the results for increasing standoff distances. The results obtained by using the complete formulation are pre-

sented in Fig. 6.5. For each experiment the reconstruction works very well as long as the hologram contours are located in the very near-field, i.e. within a distance of approximately $\lambda_B/4$. It is observed that larger standoff distances will lead to an unstable reconstruction across the whole spectrum, not just at high frequencies. As seen in Fig. 6.6, the situation can be remedied by using the simplified formulation of NSBSH. In spite of increasing standoff distances, backward-propagation remains stable and accurate. This leads to the first and somewhat ironic conclusion regarding NSBSH in practice: The omission of explicit near-field influences is a key factor in achieving a reliable result when propagating backward toward the source. The typical accelerometer noise floor shown in Fig. 6.5 confirms that the signal-to-noise ratio is sufficient for the most part. In experiment A it falls 10 dB below the response at the low and high end of the considered spectrum, which means that the procedure might have run into trouble had the excitation been weaker.

In terms of stability, the situation is different if forward-propagation through NSBSH is attempted. As can be concluded from Fig. 6.7, the reconstruction of a far-field spectrum does not need to be based on measurement in the near-field. For the most part the spectra are predicted quite correctly, regardless of the standoff distance. The results only differ at low frequencies. This does not seem surprising, given the modal behavior of the plate, which is expected to lead to better or worse results, depending on the response position. If the simplified formulation is used, as shown in Fig. 6.8, quite interestingly even these differences are eradicated.

In contrast, the corresponding results obtained by using the pure far-field approaches for experiment B and C are shown in Fig. 6.9. The first thing to note is that the straightforward use of KHI fares better than the BEM-approach in general. BEM shows a clear tendency to underpredict the response levels, but especially at higher frequencies it may underpredict the correct response by up to 10 dB, if not more. Doubling the number of sampling points improves the BEM-results significantly, while the improvement for KHI is marginal. Doing so means that the overall amount of sampling points N_{tot} used for BEM equals that of NSBSH in the end. The BEM-results may be brought to closely resemble the KHI-results by using even more sampling points, although that would counter the initial promise of reduced measurement effort. On the other hand, it is still much more convenient to sample a single contour instead of three. Regardless, the deviations at high frequencies show that BEM is the least accurate of the presented methods. In the end, the results from the infinite plate experiments show that choosing a purely far-field-based approach like KHI can give results that are almost identical to the near-field approach presented by NSBSH.

It must be noted that every experimentally obtained spectrum shown in this thesis has been frequency-averaged in order to improve the readability of the curves. Initially, FFT-analysis was performed for 3201 spectral lines in a frequency range up to 10 kHz, with spectral averaging over a period of thirty seconds. The resulting spectra were then averaged down to 120 spectral lines in the last step of processing

in order to improve the readability of the curves. The difference between initial and averaged spectrum is shown and discussed in Section 6.2.3.

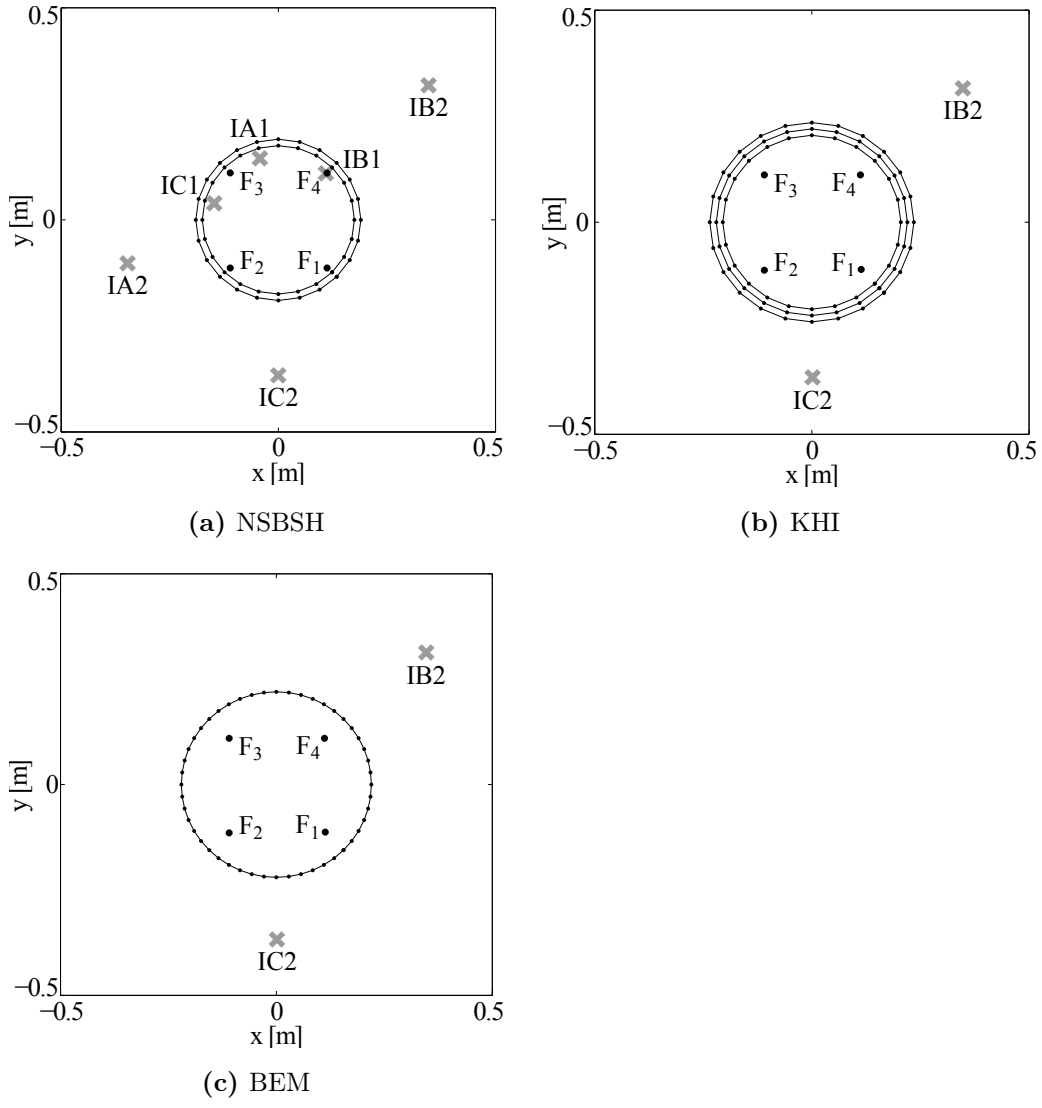

(a) NSBSH

(b) KHI

(c) BEM

Figure 6.4: Measurement geometry, reconstruction points and force positions on the infinite plate; • force excitation; • accelerometer position; × reconstruction point.

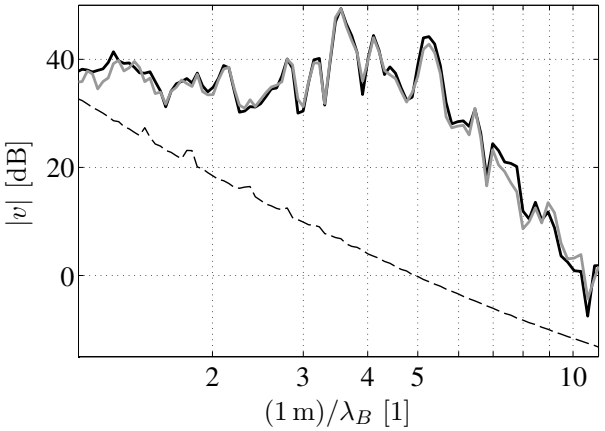

(a) measurement IA1

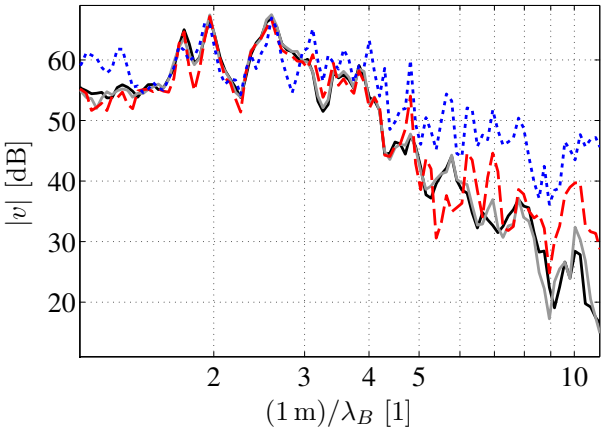

(b) measurement IB1

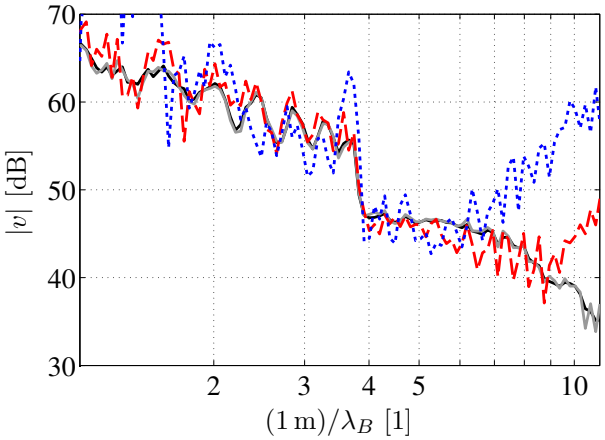

(c) measurement IC1

Figure 6.5: NSBSH, backward-propagation on an infinite plate for varying stand-off distances; – – mean accelerometer noise floor; ——— direct measurement; reconstruction:
——— $d_{\mathrm{st},1}$=0.015 m, – – $d_{\mathrm{st},1}$=0.03 m, · · · $d_{\mathrm{st},1}$=0.045 m.

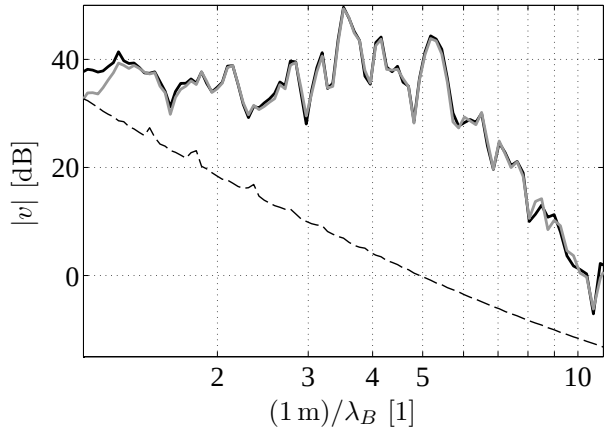

(a) measurement IA1

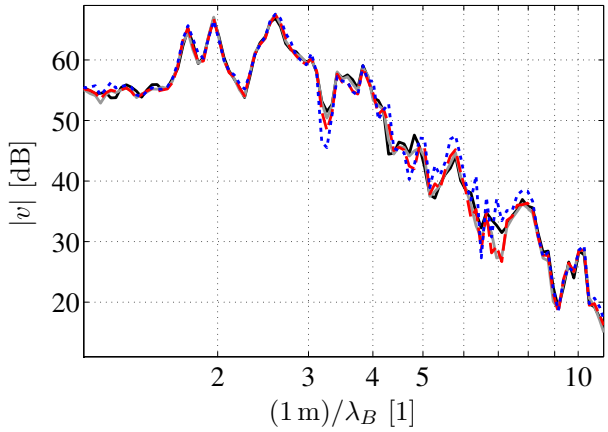

(b) measurement IB1

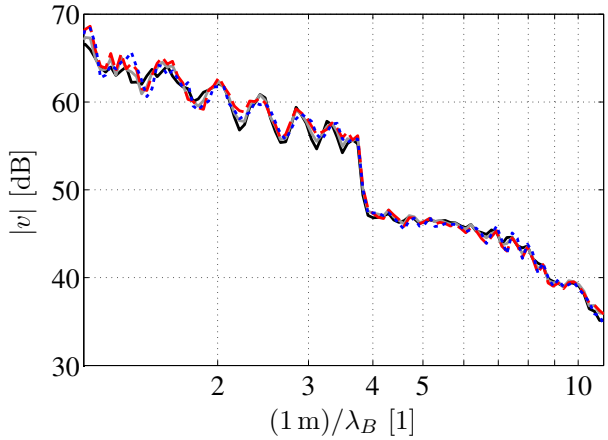

(c) measurement IC1

Figure 6.6: Simplified NSBSH: backward-propagation on an infinite plate for varying standoff distances; — — mean accelerometer noise floor; ——— direct measurement; reconstruction: ——— $d_{\mathrm{st},1}$=0.015 m, — — $d_{\mathrm{st},1}$=0.03 m; ····· $d_{\mathrm{st},1}$=0.045 m.

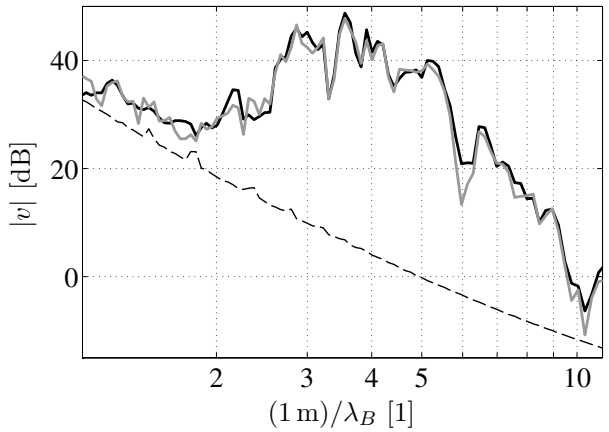

(a) measurement IA2

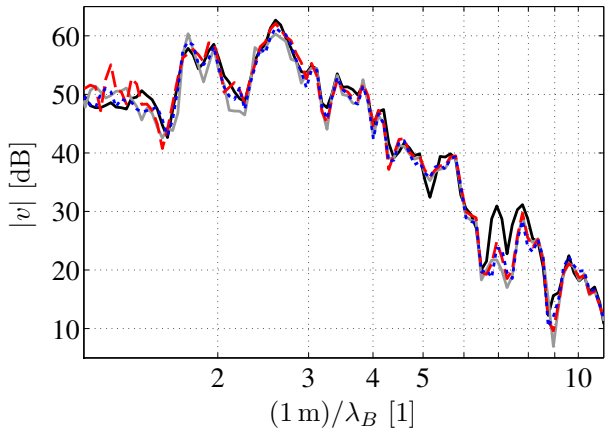

(b) measurement IB2

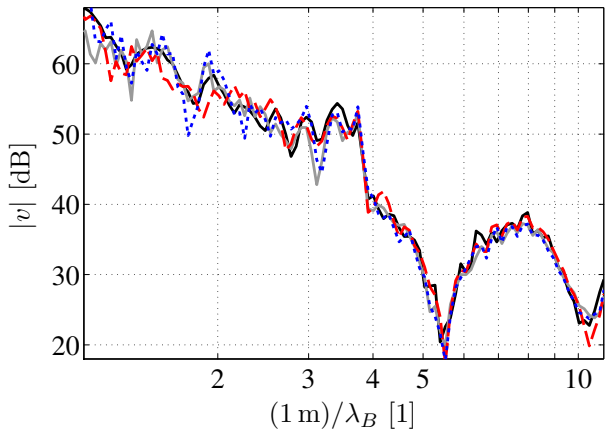

(c) measurement IC2

Figure 6.7: NSBSH: forward-propagation on an infinite plate for varying standoff distances; ——— direct measurement; reconstruction: ——— $d_{\mathrm{st},1}$=0.015 m, – – – $d_{\mathrm{st},1}$=0.03 m, ····· $d_{\mathrm{st},1}$=0.045 m.

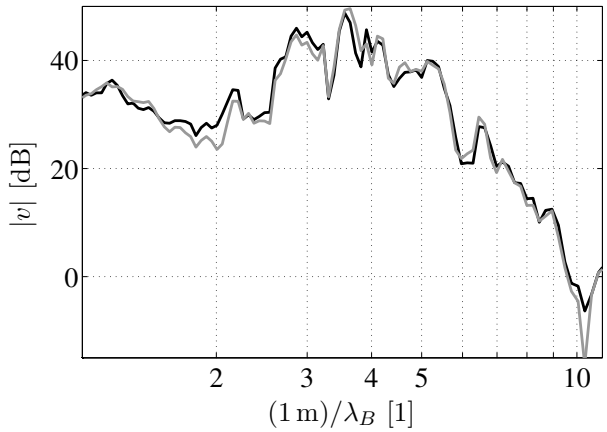

(a) measurement IA2

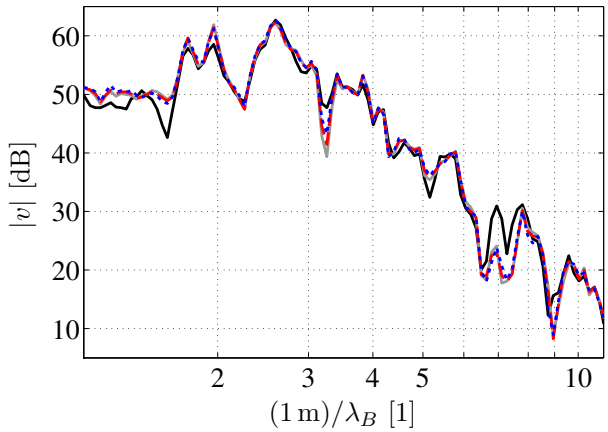

(b) measurement IB2

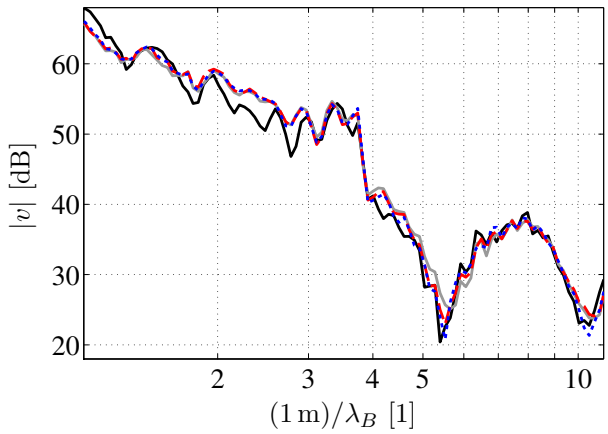

(c) measurement IC2

Figure 6.8: Simplified NSBSH: forward-propagation on an infinite plate for varying standoff distances; ——— direct measurement; reconstruction: ——— $d_{\mathrm{st},1}$=0.015 m, – – – $d_{\mathrm{st},1}$=0.03 m, · · · · $d_{\mathrm{st},1}$=0.045 m.

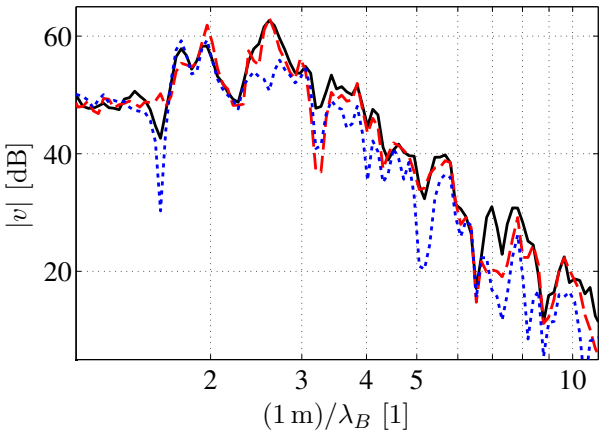

(a) measurement IB2 ($N = 24$)

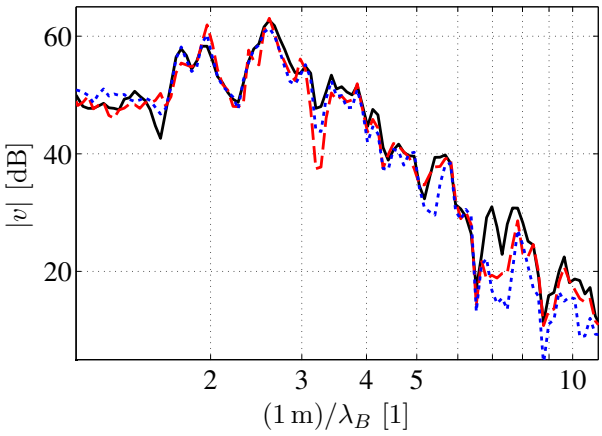

(b) measurement IB2 ($N = 48$)

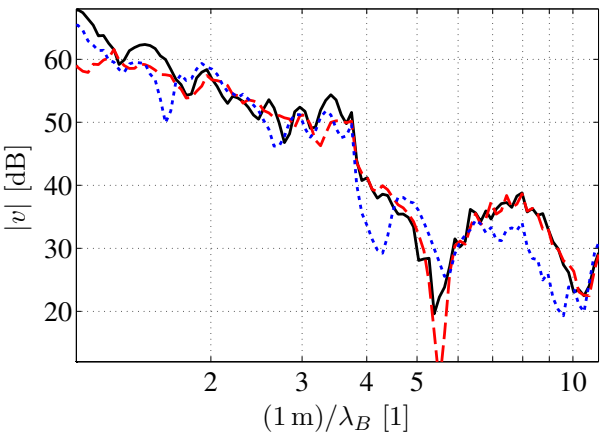

(c) measurement IC2 ($N = 24$)

Figure 6.9: Comparison of KHI and BEM on an infinite plate; ━━ direct measurement; ▬ ▬ KHI; ┅┅ BEM.

6.2 Free plate

6.2.1 Setup

A free and a simply supported aluminum plate are used to test the procedures suggested for finite plates. Aside from their boundary condition, both plates are identical, with the material properties already given in Table 5.2. The free plate is unmodified except for two drillings that are used to suspend the structure, which is shown in Fig. 6.11a. The source consists of a pair of shakers that are mounted to the plate off-center through a circular plug, with a force transducer inserted in-between. The shaker assembly and mounting can be seen in Fig. 6.11b and Fig. 6.11f. Each shaker is being fed with white noise in the considered frequency range. The resulting excitation forces are plotted in Fig. 6.10. It is seen that the force levels drop above BWPM=6, and that they are quite similar in magnitude and in phase.

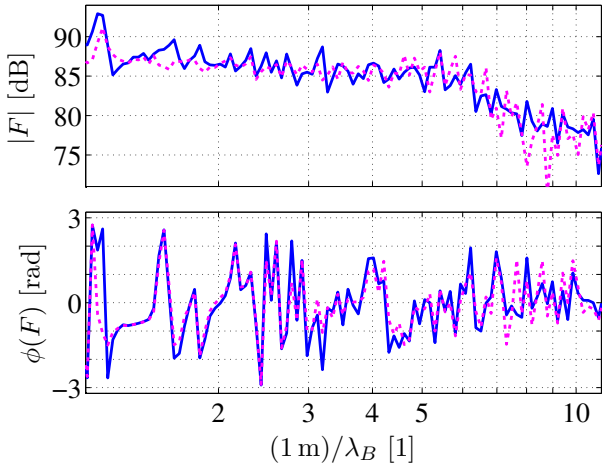

Figure 6.10: Forces applied to the free plate.

A positioning system is used to move a laser vibrometer that acts as the primary velocity sensor, while a second laser is aimed at a fixed reference position. The resulting cross spectra provide phase information for the actual velocity responses. The geometries of the utilized measurement contours are depicted in Fig. 6.12, and the measurement parameters are given in Table 6.2. The aging spindle motors that drive the positioning system were found to cause a certain positioning error that accumulated after prolonged measurement. By splitting up the measurement campaign and repeatedly starting from the home position this is pretty much kept in check, wherefore the accuracy of the measurements can ultimately be assumed to suffice.

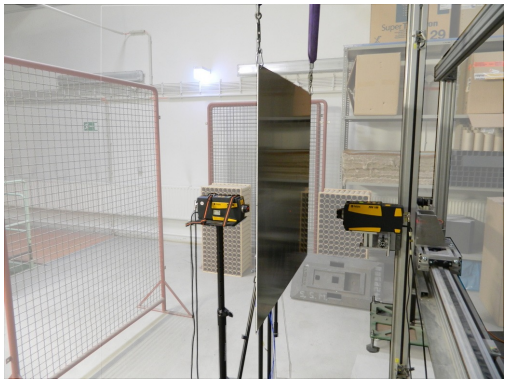

(a) free plate: positioning system with laser vibrometers

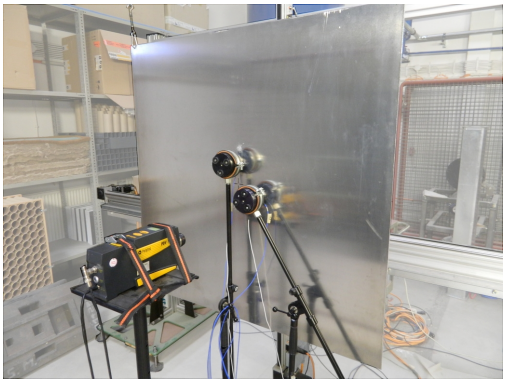

(b) free plate: source arrangement

(c) simply supported plate: positioning system with laser vibrometers

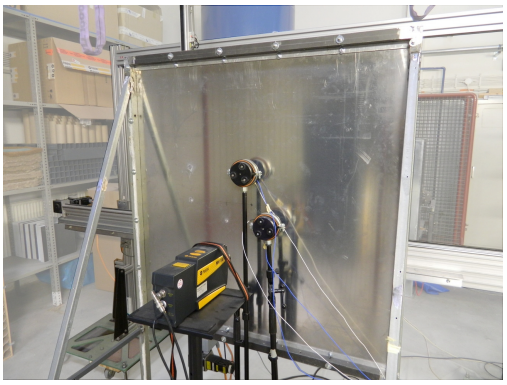

(d) simply supported plate: source arrangement

(e) simply supported plate: boundary condition

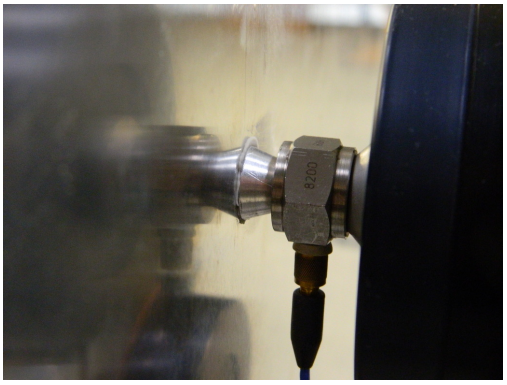

(f) source mounting

Figure 6.11: Finite plate experiments: detail views of the measurement setups.

Table 6.2: Measurement parameters for the free plate

	N_i	N_e	$d_{\mathrm{st},1}$ [m]	$d_{\mathrm{st},2}$ [m]	$d_{\mathrm{st},3,\mathrm{min}}$ [m]	$d_{\mathrm{st},4,\mathrm{min}}$ [m]	$d_{\mathrm{st,i}}$ [m]	$d_{\mathrm{st,e}}$ [m]	Δr [m]
NSBSH	36	72	0.015	0.025	0.005	0.02			
KHI	36	92					0.025	0.033	0.012

6.2.2 Spatial field reconstruction

The measurement positions that are used to perform NSBSH and KHI are depicted in Fig. 6.12. While the hologram contours for NSBSH must remain circular, the boundary contours for KHI can be chosen conformal to the plate geometry. In the finite case, KHI requires six contours to be sampled, while NSBSH requires four. The number of sampling points is also given in Table 6.2, along with the other relevant measurement parameters. The outer boundary contours for KHI are clearly moved inward, in the hope of escaping the structural near-field that is expected at the free edges. As a reference for the reconstructed field, the true response field is obtained by direct measurement at $25 \cdot 25 = 625$ sampling points across the surface. The points are equidistant in both x- and y-direction, forming a rectangular grid, as depicted in Fig. 6.12.

Examples for the resulting reconstruction of the normal velocity magnitude are shown in Figs. 6.13 and 6.14, whereby the former shows the eleventh eigenmode of the plate. The results confirm the tendencies found in Section 5.8.2: KHI overpredicts the field at low frequencies and is accurate at high frequencies. Either way, the shape of the modal patterns is reconstructed correctly. Also confirmed are the tendencies found with NSBSH, which pretty much oppose those of KHI. Low frequency resolution is very good. In fact, the reconstruction looks more refined than the direct measurement. This is thanks to the nature of the utilized cylindrical Hankel functions, which are a good fit if circular shapes have to be "built". High frequency reconstruction is a bit more challenged due to the approximative underlying model. More drastic wavenumber-filtering has to be applied to avoid blown-up results near the inner contour lines if the distance between inner and outer hologram contour becomes approximately three times larger than the considered bending wavelength.

The corresponding reconstruction error is shown in Fig. 6.15, and as in the simulations, the highest deviations are usually found where a low magnitude has to be predicted. It is also seen that at high frequencies the reconstruction error becomes large immediately if one tries to reconstruct the field outside the outer hologram contour.

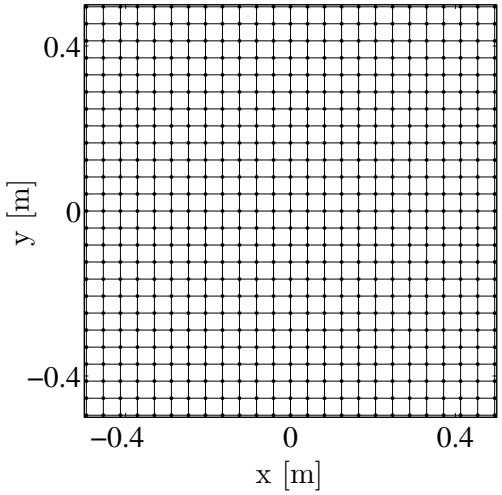

(a) direct measurement

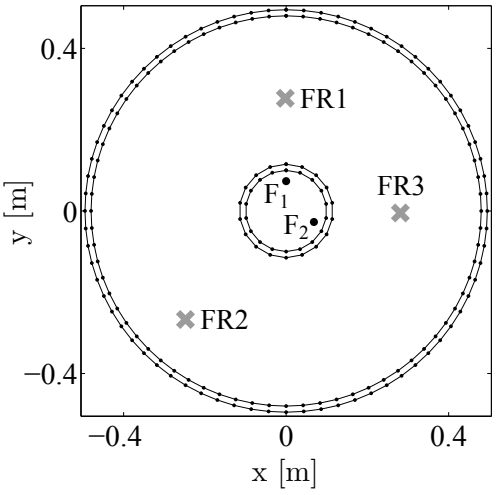

(b) NSBSH

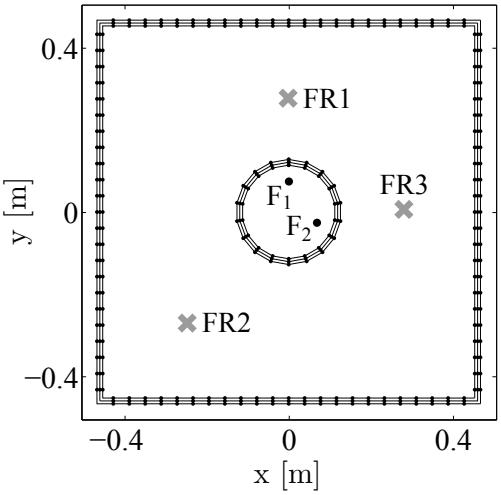

(c) KHI

Figure 6.12: Measurement geometry, reconstruction points and force positions on the free plate; • force excitation; • laser vibrometer position; x reconstruction point.

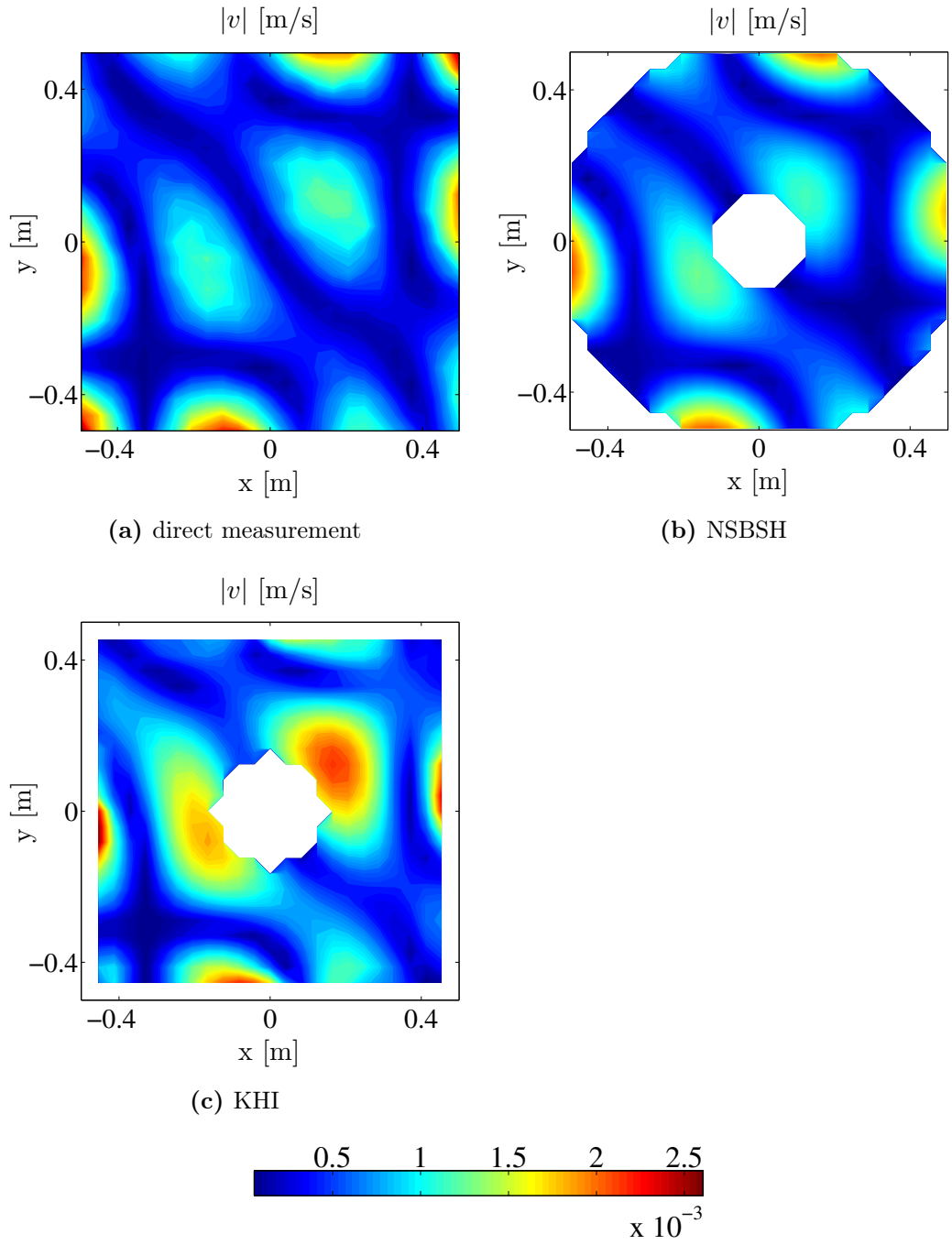

(a) direct measurement

(b) NSBSH

(c) KHI

Figure 6.13: Comparison of extrapolation methods on a free plate: bending wave field, $f = 128\,\mathrm{Hz}$ ($(1\,\mathrm{m})/\lambda_B = 1.6$).

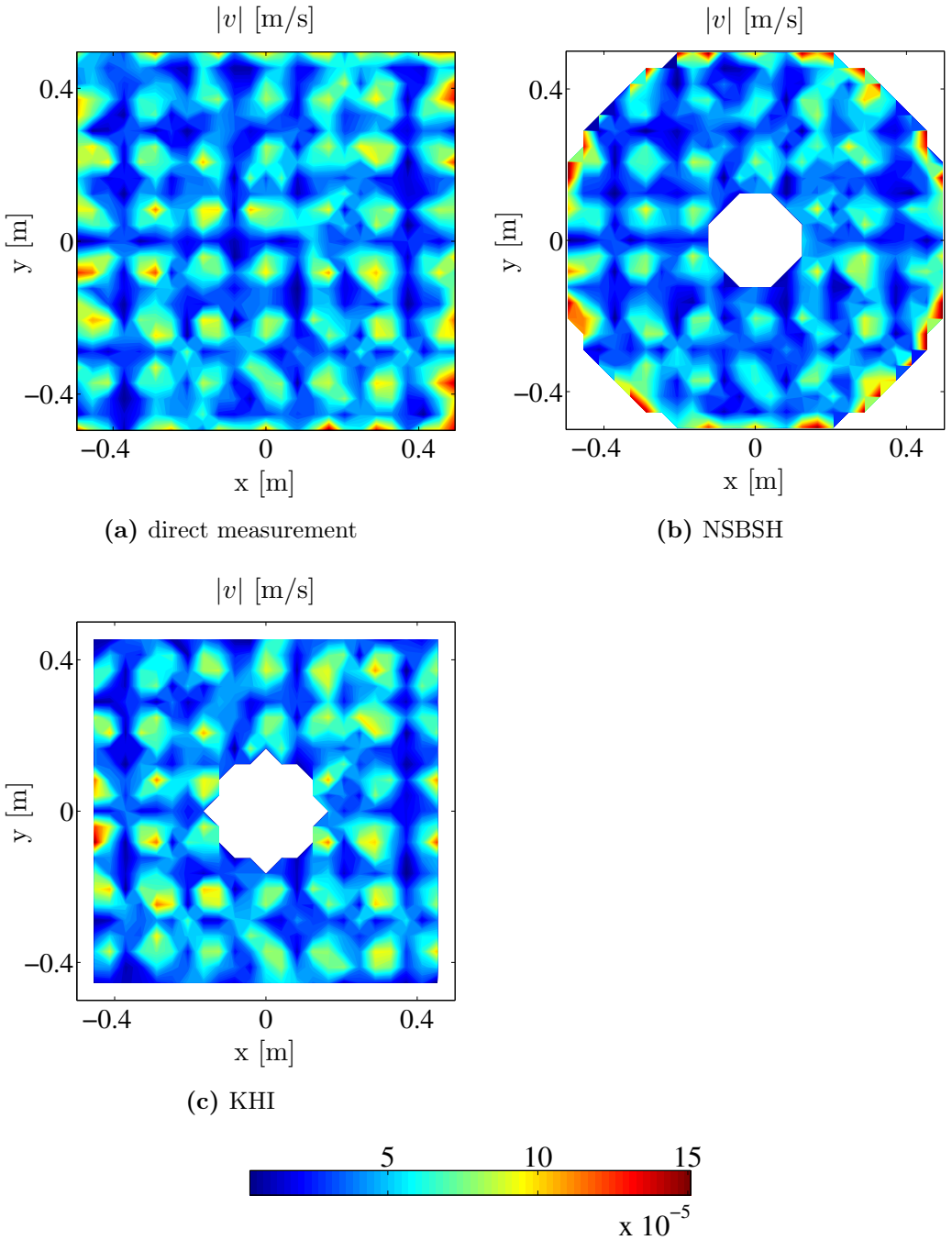

(a) direct measurement

(b) NSBSH

(c) KHI

Figure 6.14: Comparison of extrapolation methods on a free plate: bending wave field, $f = 4265\,\mathrm{Hz}$ ($(1\,\mathrm{m})/\lambda_B = 9.4$).

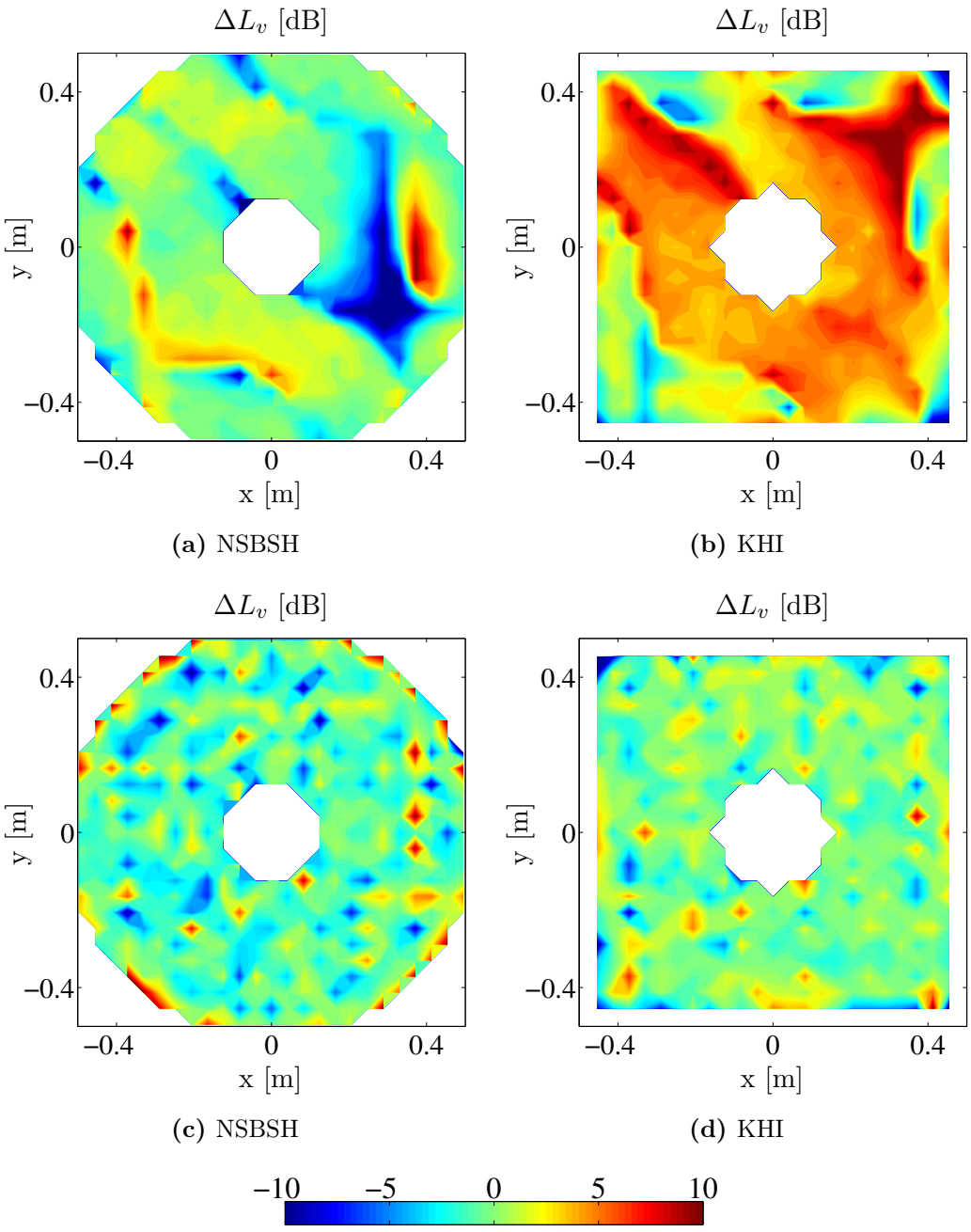

Figure 6.15: Comparison of extrapolation methods on a free plate: reconstruction error; a), b) $f = 128\,\mathrm{Hz}$; c), d) $f = 4265\,\mathrm{Hz}$.

6.2.3 Spectral reconstruction

The assessment of the free plate experiment is completed by reconstructing three arbitrary response spectra, shown in Fig. 6.16, whose positions are indicated in Fig. 6.12. The same tendencies are found with every reconstruction point. The characteristic overprediction by KHI subsides as BWPM ≈ 4.5. Considering the chosen standoff distance from the plate edges $d_{\mathrm{st,e}} = 0.033\,\mathrm{m}$, a critical distance of $d_{\mathrm{st,e}} \approx \lambda_B/6$ is identified, which confirms the findings in Section 5.8.3. In the worst cases, which would be the largest wavelengths considered in the plotted spectrum, the reconstruction error ΔL_v can amount to 10 dB or even more. Acknowledging this as inherent behavior, the reconstruction through KHI can be considered successful. The peaks and valleys in the spectrum are identified correctly and for higher frequencies the reconstruction error is very small overall.

Reassuringly, low frequencies do not pose a problem for NSBSH compared to KHI. Only at the very low end of the spectrum is the curve "not getting it right", but it is also seen that NSBSH is less accurate where the response dips significantly. There is the odd misfire in the center of the spectrum, although this might be attributed to the chosen regularization parameter. For the shown experimental results $\lambda = 5 \cdot 10^{-3}$ is chosen, as opposed to $\lambda = 1.5 \cdot 10^{-3}$ used in the simulations. This means that a more drastic regularization was implemented in practice, which is why the NSBSH-curves tend to underpredict the true spectrum here and there. All in all, the reconstruction works very well, however.

It is very important to acknowledge how these results were achieved, especially in the case of NSBSH. From the spatial distribution of the reconstruction error plotted in Section 6.2.2, one would probably expect to see larger deviations of the reconstructed curve. The dynamic range of the spectrum can be misleading here, since a deviation of 3 dB is not that noticeable if the the graph covers a range of 60 dB. Furthermore, as stated in Section 6.1.2, frequency averaging was applied for both NSBSH and KHI, reducing the number of spectral points from initially 3201 to 120. The averaging certainly mitigates over- and undershooting at adjacent frequencies, and as a result the reconstruction appears much more correct. The effect is shown in Fig. 6.17, in which the influence of the separate processing steps for NSBSH is revealed. The reconstruction position FR1 is taken as the example. Straightforward application of NSBSH is hopeless for all but the highest frequencies. Wavenumber filtering brings the reconstructed levels down for the rest of the spectrum and within a more reasonable range. Tikhonov regularization then mitigates the severe overshooting that plagues the reconstruction. The thereby reconstructed curve follows the tendency of the true curve nicely, but there is still sporadic over- and undershooting. This is finally mitigated through frequency averaging, which cleans up the results. The first important conclusion is that all the processing discussed in Chapter 5 is unconditionally necessary. The second conclusion is that these methods are not well suited for the exact analysis of very specific narrow frequencies in the spectrum.

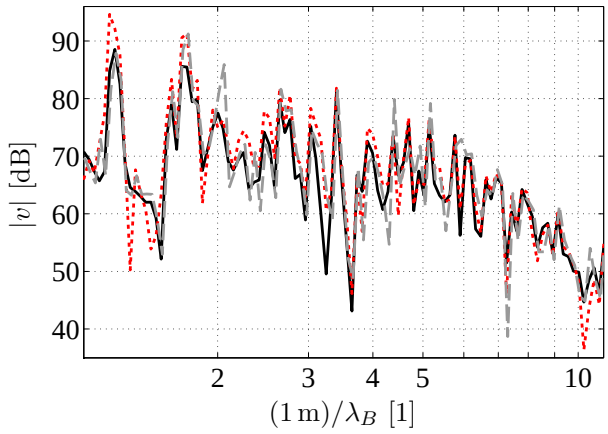

(a) position FR1

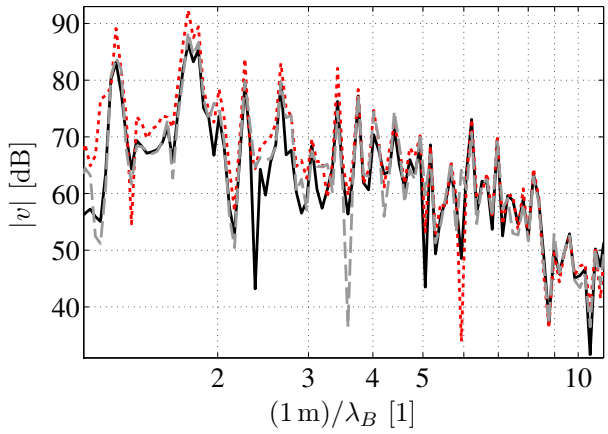

(b) position FR2

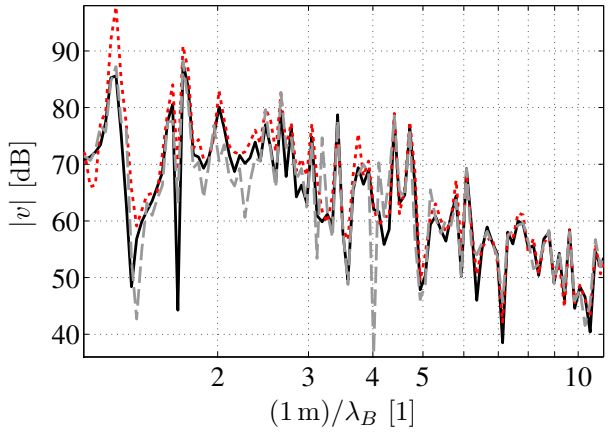

(c) position FR3

Figure 6.16: Comparison of extrapolation methods on a free plate: reconstruction of a response spectrum by means of NSBSH and KHI; ——— direct measurement; – – – NSBSH; ····· KHI.

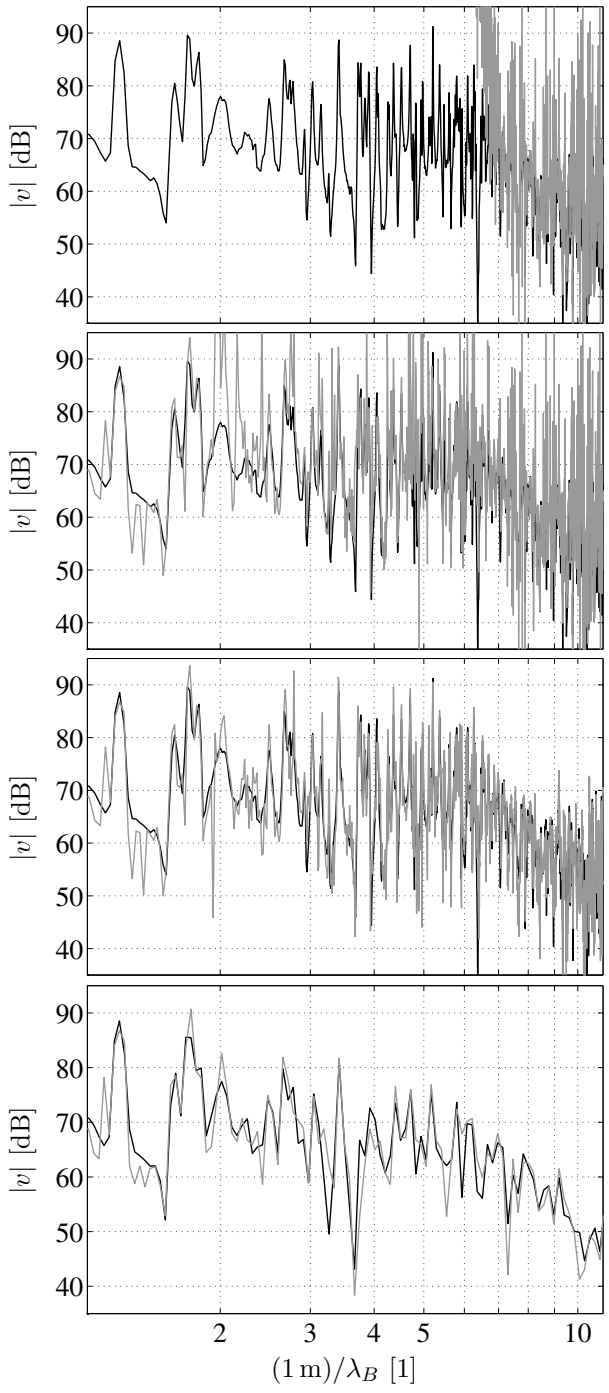

(a) straightforward

(b) wavenumber-filtered

(c) wavenumber-filtered, regularized

(d) wavenumber-filtered, regularized and frequency-averaged

Figure 6.17: Results from the processing steps of numerical stabilization and frequency averaging for NSBSH; free plate, position FR1; — direct measurement; — NSBSH.

6.3 Simply supported plate

6.3.1 Setup

Setting up a simply supported aluminum plate has been detailed in the literature before. It has been shown that the boundary condition can be forced by using angles to bolt the plate to a blade that is mounted on a very heavy foundation [75]. Such a setup seems inconvenient, however, given that there is no need to achieve a completely accurate boundary condition in order to validate the theory. Another approach to a reasonable experimental setup is taken, as shown in Fig. 6.11c-6.11e. A continuous groove is cut close to the edges of the plate, reducing the thickness from 0.005 m to approximately 0.001 m and thus leading to a locally decreased bending stiffness. The edges themselves are screwed to a steel frame. In this way the groove acts like a hinge and the plate area confined by the groove can be considered as simply supported. Naturally this does not present a true simple support. The frame does not behave like a rigid mass, the plate has a groove of finite thickness and there are a limited number of screws that are not tightened identically. The actually imposed boundary condition is probably not the same along all sides of the plate as a result.

The source setup for the simply supported plate is similar to that of the free plate, as can be seen in Fig. 6.11d. The shakers are positioned a bit more toward the center but they are otherwise connected and driven in the same way. Due to the enforced boundary condition, the resulting forces differ in magnitude and in phase, as seen in Fig. 6.18.

Because of the construction, the plate is very slightly skewed in comparison to the axis of the positioning system. This means that in practice the plate is not fully symmetrical to the utilized measurement geometries that are depicted in Fig. 6.19. The measurement parameters used in the experiment are given in Table 6.3.

Table 6.3: Measurement parameters for the simply supported plate

	N_i	N_e	$d_{\mathrm{st},1}$ [m]	$d_{\mathrm{st},2}$ [m]	$d_{\mathrm{st},3,\mathrm{min}}$ [m]	$d_{\mathrm{st},4,\mathrm{min}}$ [m]	$d_{\mathrm{st,i}}$ [m]	$d_{\mathrm{st,e}}$ [m]	Δr [m]
NSBSH	36	72	0.015	0.03	0.005	0.02			
KHI	36	92					0.03	0.025	0.01

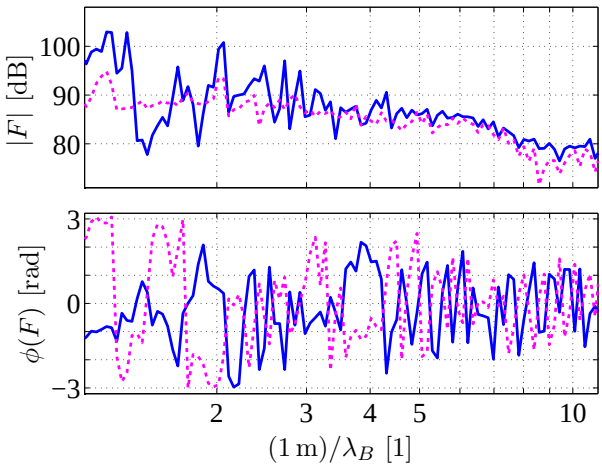

Figure 6.18: Forces applied to the simply supported plate.

6.3.2 Spatial field reconstruction

As Fig. 6.20 proves, the reconstruction of the continuous spatial field at a low frequency works well with both NSBSH and KHI. In the absence of a strong near-field along the edges, even the latter is able to reproduce the magnitude of the field correctly. This tendency has been predicted in Section 5.9.2. The low magnitude determined by the direct measurement positions near the edges suggests that, at least for low frequencies, the simply supported boundary condition was indeed approximated.

Whereas the low-frequency field considered in Section 6.2.2 shows a distinct modal shape that belongs to an eigenfrequency of that plate, the same cannot be said here. The considered frequency does not equal an eigenfrequency of the plate, and also the achieved boundary condition is not exact enough to produce a characteristic modal pattern.

The magnitude of the high-frequency field, shown in Fig. 6.21, is a little over-predicted by KHI, as can also be seen through the level difference in Fig. 6.22. Otherwise, both NSBSH and KHI appear to reconstruct the spatial field correctly.

Another aspect regarding this kind of wave field extrapolation is the obtainable spatial resolution. If far-field conditions can be assumed and if the number of sampling points along the contours is sufficient, then the spatial resolution can be chosen freely. Halving the distance between reconstruction points compared to the direct measurement, results in Figs. 6.20d and 6.21d. For the low frequency this does not make a big difference, except for a nicer looking graphic. For the high frequency we get a much clearer visual representation of the nodal lines, however. It can be concluded that wave field extrapolation, as imagined in this thesis, can improve the visual representation of the wave field. This certainly is a positive side effect.

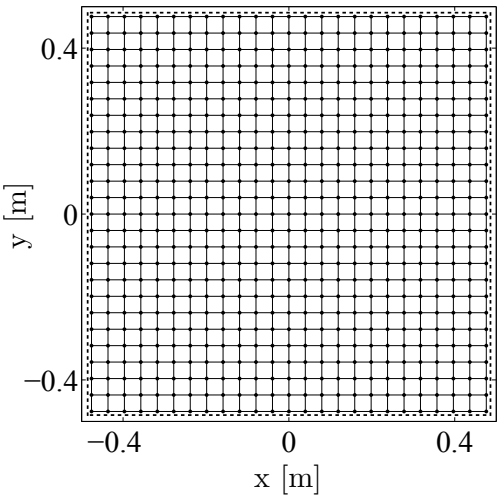

(a) direct measurement

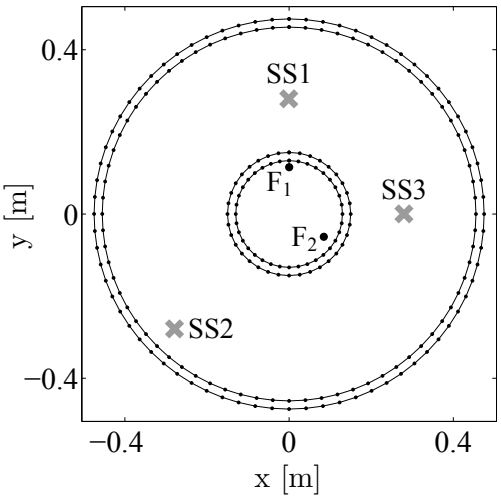

(b) NSBSH

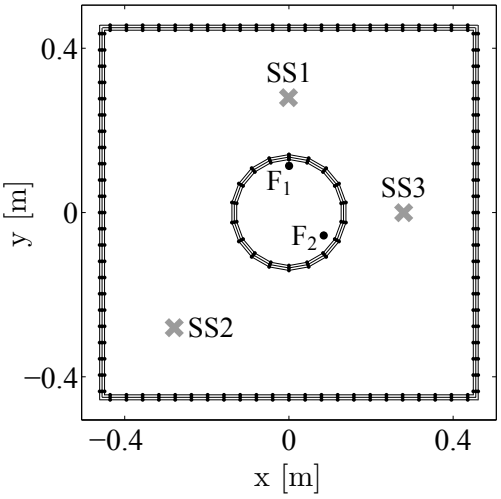

(c) KHI

Figure 6.19: Measurement geometry, reconstruction points and force positions on the simply supported plate; • force excitation; • laser vibrometer position; × reconstruction point; **- -** effective boundary.

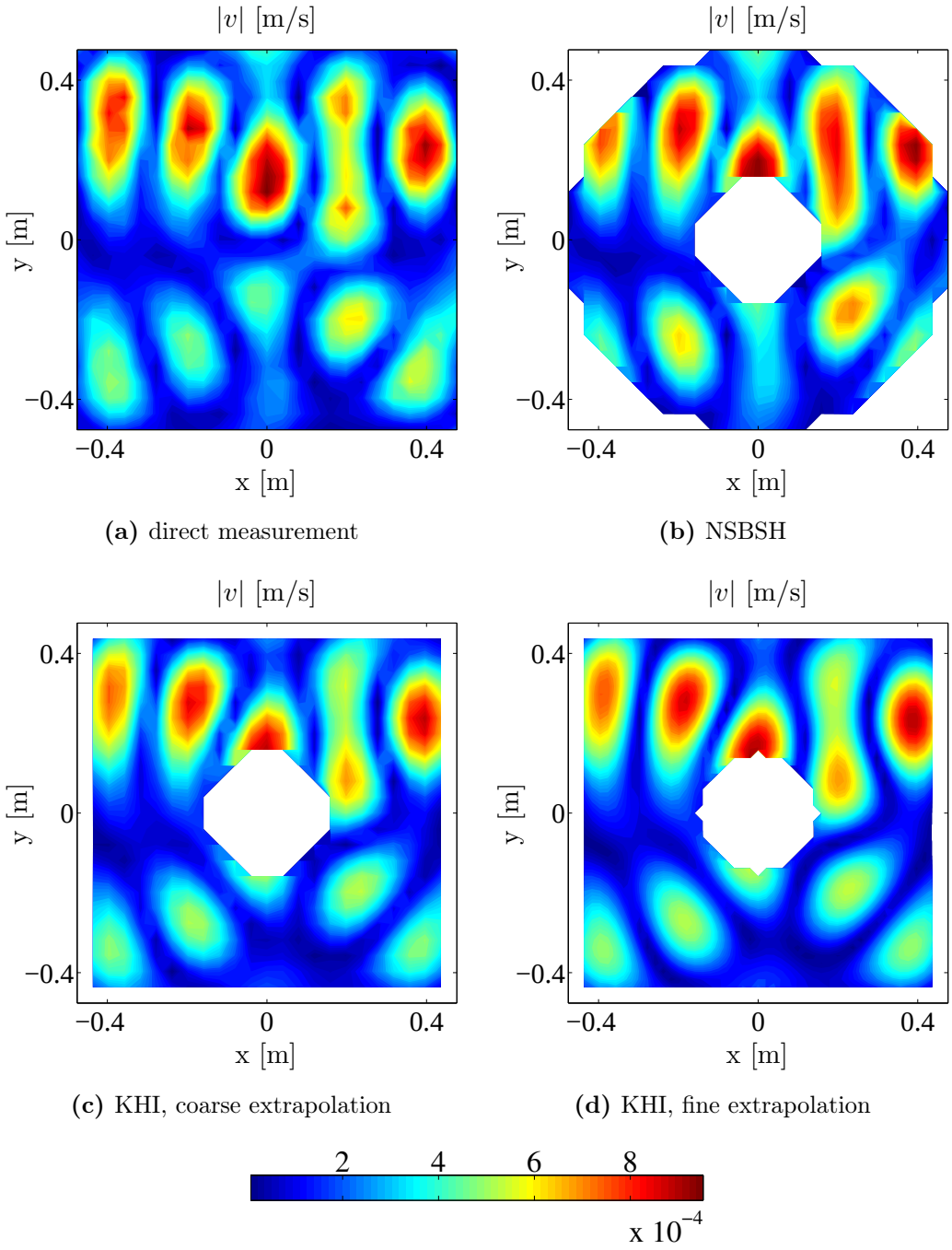

(a) direct measurement

(b) NSBSH

(c) KHI, coarse extrapolation

(d) KHI, fine extrapolation

Figure 6.20: Comparison of extrapolation methods on a simply supported plate: bending wave field, $f = 360\,\mathrm{Hz}$ $((1\,\mathrm{m})/\lambda_B = 2.7)$.

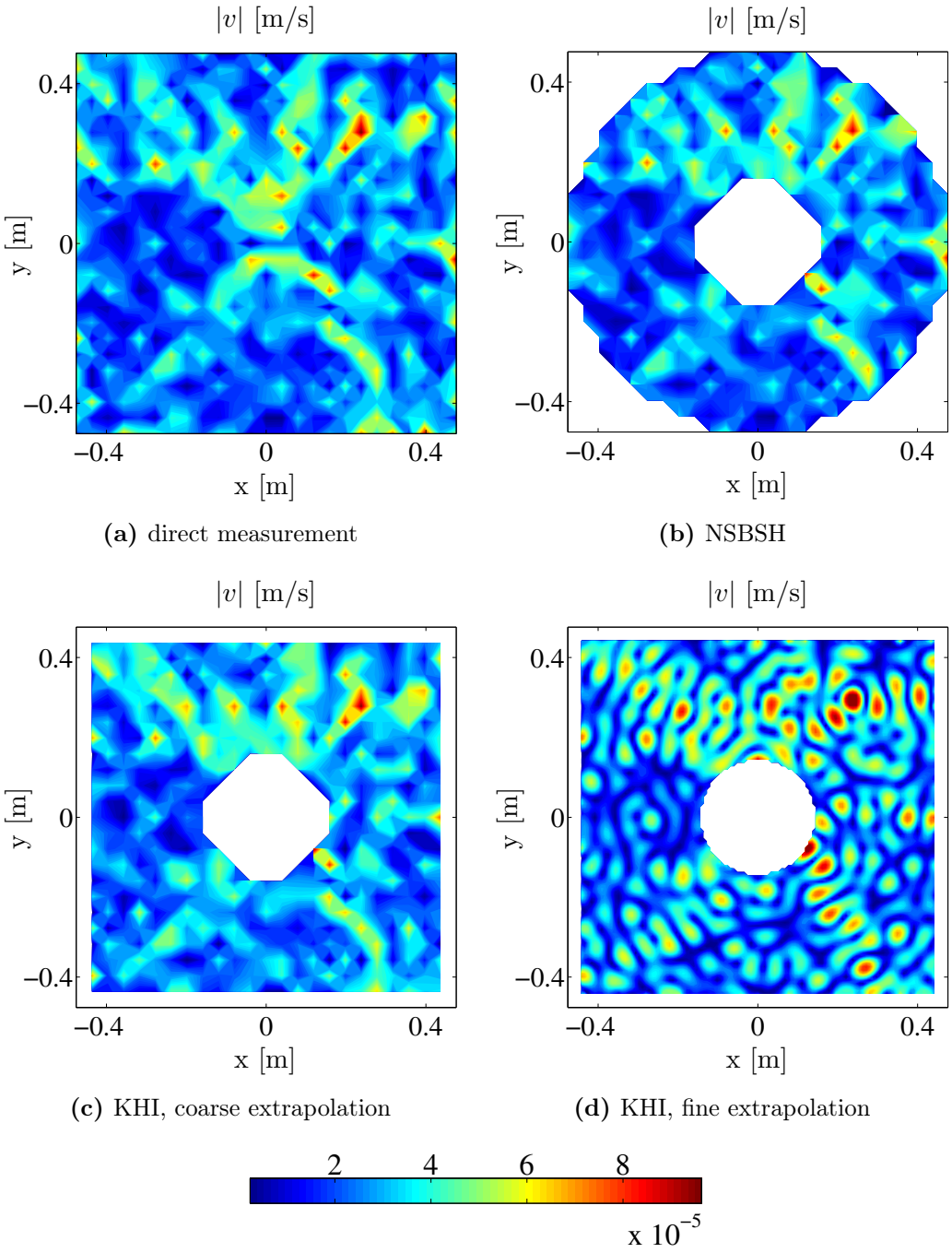

(a) direct measurement

(b) NSBSH

(c) KHI, coarse extrapolation

(d) KHI, fine extrapolation

Figure 6.21: Comparison of extrapolation methods on a simply supported plate: bending wave field, $f = 4494\,\mathrm{Hz}$ ($(1\,\mathrm{m})/\lambda_B = 9.65$).

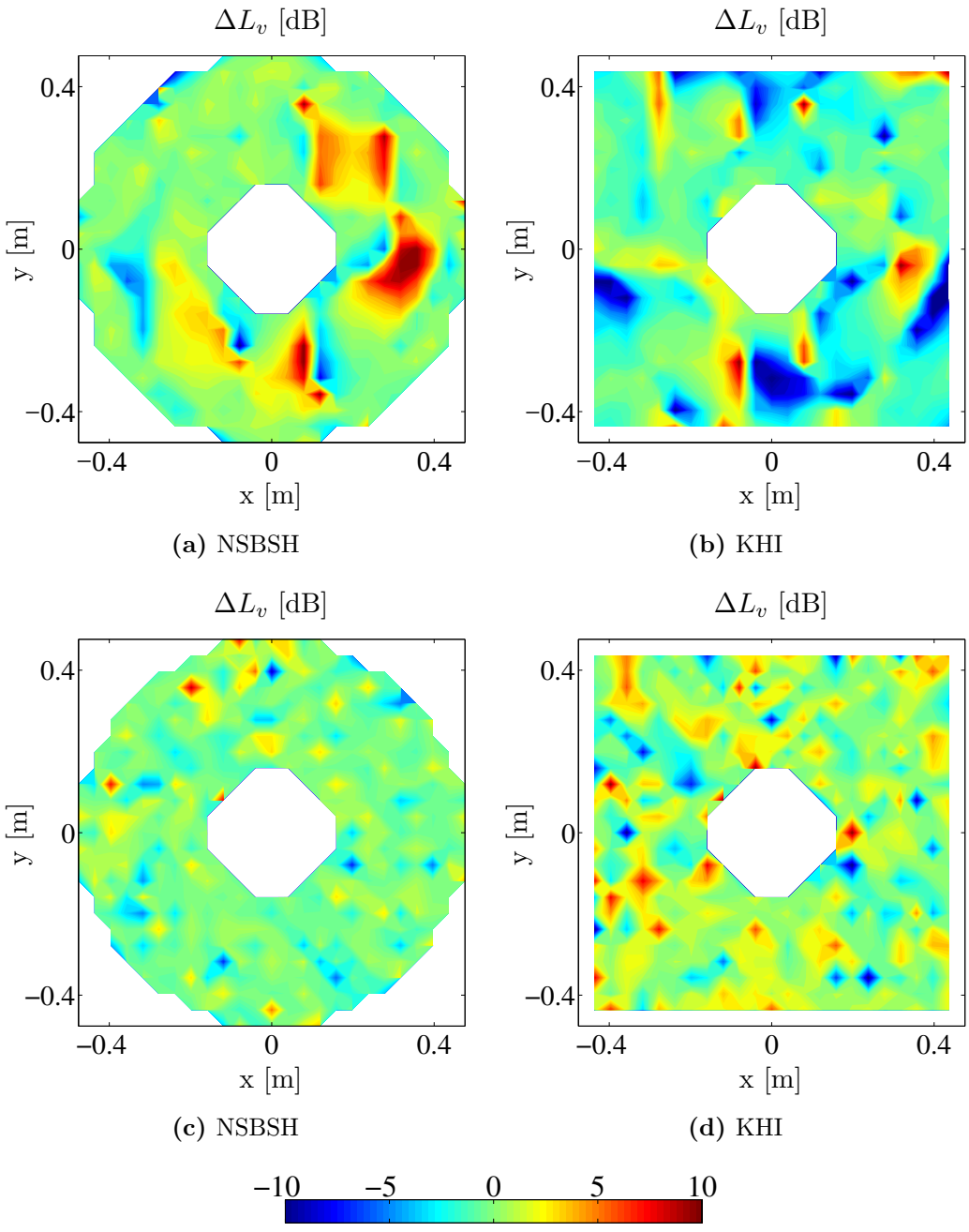

Figure 6.22: Comparison of extrapolation methods on a simply supported plate: reconstruction error; a), b) $f = 360\,\mathrm{Hz}$; c), d) $f = 4494\,\mathrm{Hz}$.

6.3.3 Spectral reconstruction

The results presented in Fig. 6.23 show that both NSBSH and KHI are mostly able to detect the peaks and dips that form the true response spectrum at any given position. In general, NSBSH proves to be more accurate, although it is not save from greatly exaggerating sudden drops in the response occasionally. At position SS2, which is very close to the outer hologram contours, the results for NSBSH are unsurprisingly best. It is noted that the same regularization parameter is used as for the free plate, which may explain these occasional dips of the reconstructed level. It has to be kept in mind that a fixed regularization parameter was used, which means that these miscalculations could probably be avoided if a suitable algorithm for the evaluation of the optimal parameter was used. The empirically chosen constant value provides a rather rudimentary stabilization.

While KHI does not generally overpredict the low end of the spectrum as with the free plate, it is not as accurate as NSBSH. The reconstruction error now mostly appears where level-drops have to be detected. The correct value can occasionally be mispredicted by 10 dB. In fairness, and as stated before, this is less of an issue than mispredicting level peaks. These results indicate that regardless of the attempts to create a near-field-free boundary condition, there happens to be at least some near-field influence at the measurement positions. As a consequence, KHI fares worse, especially at low frequencies. “Worse” is a relative term of course, and it must be said that the overall results are very satisfying for both methods. Certainly these results would be deemed sufficiently accurate in many engineering applications.

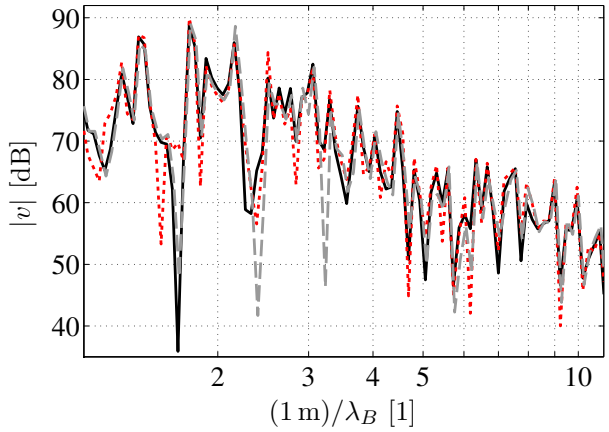

(a) position SS1

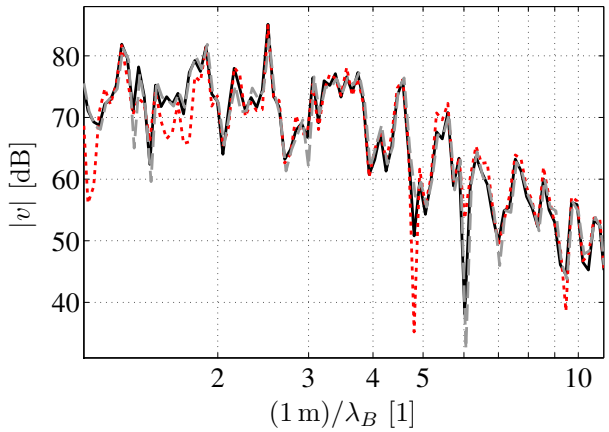

(b) position SS2

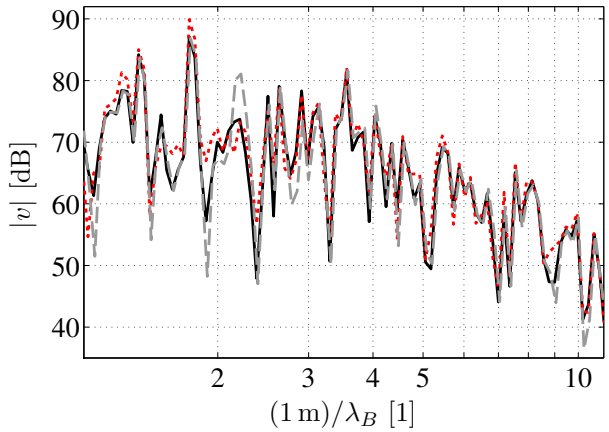

(c) position SS3

Figure 6.23: Comparison of extrapolation methods on a simply supported plate: reconstruction of a response spectrum by means of NSBSH and KHI; ━━ direct measurement; ╌╌ NSBSH; ┅┅ KHI.

6.4 Average reconstruction error

In a final evaluation of the methods, the level difference of the spatially averaged velocity $\Delta L_{\overline{v}}$, defined in Section 5.2, is considered. The spectra of $\Delta L_{\overline{v}}$ are calculated from both experimental results and simulations. The latter are carried out by assuming zero measurement noise, using the positions and forces that were used in the measurements. In this way it is possible to compare the (unavoidable) computational reconstruction error to the total reconstruction error in practice. Since the infinite, free, and simply supported plates considered in this thesis are compared directly, Figs. 6.24 and 6.25 can be seen as a summarization of all the investigations.

In the case of the infinite plate, the level difference observed for NSBSH mostly ranges from $-2\,\mathrm{dB}$ to $+2\,\mathrm{dB}$. The error can be higher at low frequencies, at which the plate was shown to behave more like a finite plate. The corresponding computational reconstruction error, i.e. the reconstruction error that results purely from the implementation of the theory, is insignificant. The curves look markedly different for KHI, where the inherent computational reconstruction error is much higher. Both measurement and simulation have the same tendency, which seems to be dominated by the character of the Hankel functions. Except for a few frequencies with higher deviation, the level difference remains within a range between $-2\,\mathrm{dB}$ and $+2\,\mathrm{dB}$, although the average deviation is visibly larger than for NSBSH, even at high frequencies.

In the case of the free plate, NSBSH shows that it is having a rough time with the highly resonant[1] behavior of the structure, whose boundary conditions do not agree too well with the utilized physical model for wave propagation. The frequent thin peaks that occur for the simulated values of $\Delta L_{\overline{v}}$ become larger with frequency. In comparison, the experimental curve in this frequency region shows a significantly lower and much more stable error thanks to the applied frequency averaging. This is another reminder of what difference the act of frequency averaging has on these results, and that the method is actually not well suited to analyze narrow frequencies in a spectrum. Curiously, even without frequency averaging the experiment fares better than the simulation at high frequencies. Neverthless, the error peaks in the midrange are worrisome and indicate that there are indeed limits as to what analytical basis functions can do even with such simple structures. Save for a narrow low-to-intermediate frequency region, where $\Delta L_{\overline{v}}$ spikes up to $5\,\mathrm{dB}$, the error ranges from $-2\,\mathrm{dB}$ to $+3\,\mathrm{dB}$ in practice, which means that a higher response tends to be calculated mostly. KHI is much more predictable in general: $\Delta L_{\overline{v}}$ decreases in linear fashion with frequency, from approximately $-4\,\mathrm{dB}$ to $-1\,\mathrm{dB}$, until it fluctuates around $0\,\mathrm{dB}$. The experiments seem to fare a

[1] "Resonance" refers to the vibration at modes in the presence of damping. It is acknowledged that vibration at a resonance frequency can only be equated to vibration at an eigenfrequency when damping is very small. So far the presence of damping was implied when "modal behavior" was brought up.

little better than the simulations, which indicates that the simulated near-field and the practically observed near-field at the edges might not be directly comparable. Since both curves clearly show the same reasonable tendency, this is no cause for concern.

It is apparent that the simply supported plate constitutes a "good-natured" structure in comparison to the free plate. The results obtained by NSBSH are even better than for the infinite plate. Except for the high end of the spectrum, the level difference has a range from $-1\,\mathrm{dB}$ to $+1\,\mathrm{dB}$, although the results are obviously better at most frequencies. This is in agreement with the fact that the computational error is small as well. At high frequencies, the level difference increases slightly, and it has to be noted that without frequency averaging this would appear to be more severe. For KHI, $\Delta L_{\overline{v}}$ lies in-between $-2\,\mathrm{dB}$ and $2\,+\mathrm{dB}$ in general.

It can be concluded that both methods were found to be reasonably accurate in all cases, although some results are clearly better than others. The free plate leads to the worst results in general, for the reasons discussed above and in Section 5.8.2. The existence of strong near-fields also leads to the worst results for KHI, naturally. Wether or not one should expect an average reconstruction error of 1 dB or 4 dB at worst, therefore depends on the boundary condition. The less the plate boundary is generating a near-field, the better for KHI. The more the plate boundary allows a sum of expanded Hankel functions as a solution in polar coordinates, the better for NSBSH.

As a reminder it is noted that these results are only suitable to analyze the tendencies of the reconstruction error. Because $\Delta L_{\overline{v}}$ constitutes a spatial average, it is not an indication for the range of the reconstruction error at individual field positions.

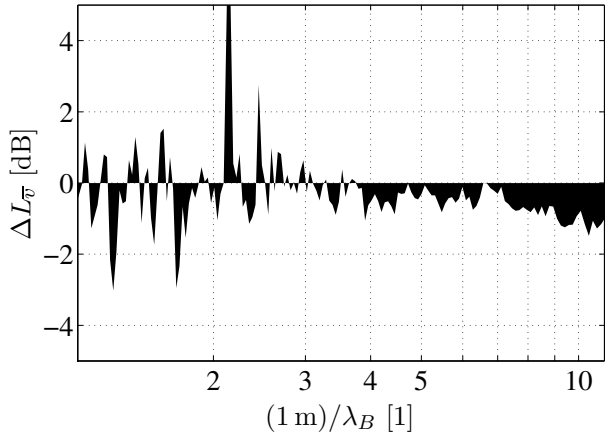

(a) infinite plate

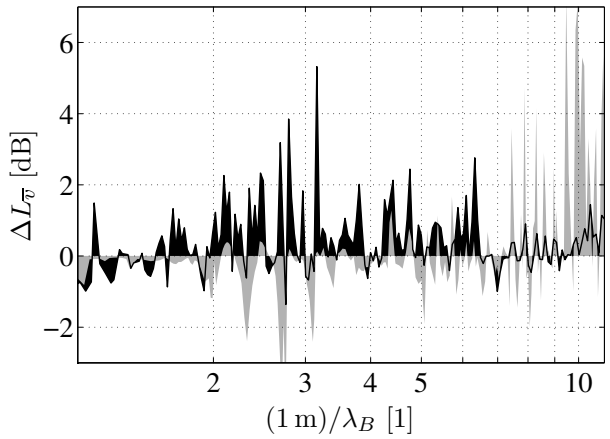

(b) free plate

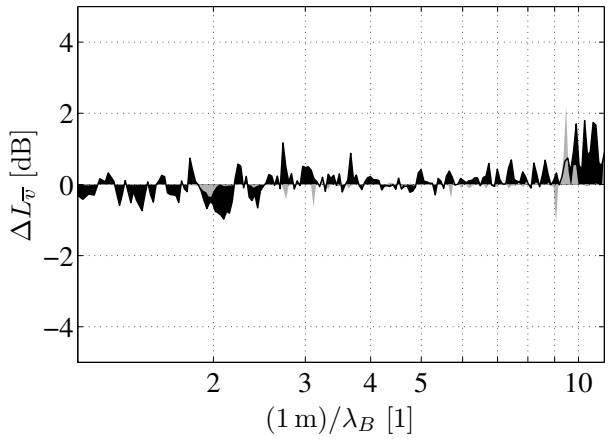

(c) simply supported plate

Figure 6.24: Average reconstruction error, NSBSH;
experimental; computational (uncorrupted input data).

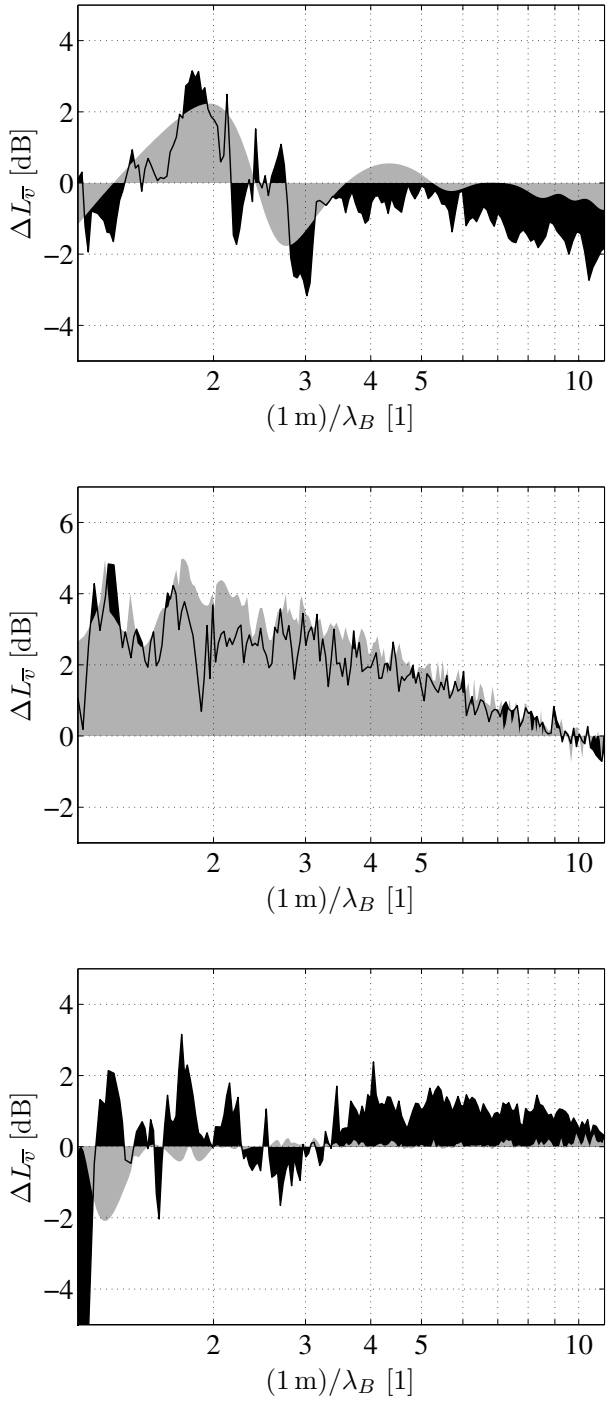

(a) infinite plate

(b) free plate

(c) simply supported plate

Figure 6.25: Average reconstruction error, KHI;
experimental; computational (uncorrupted input data).

6.5 Conclusions

By most accounts, the experiments confirm the results indicated by the simulations, and it can be said that the conclusions drawn in Section 5.11 apply in practice as well. This assumes that the medium of interest is a homogenous and isotropic plate subjected to stationary excitation. In principle, both NSBSH and KHI are able to reconstruct the continuous spatial response as well as response spectra of bending wave fields with good accuracy. However, the former runs into trouble given a structure like the fully free plate because the utilized propagation functions are not particularly suitable eigenfunctions of the problem, while the latter is not very well suited if low frequencies have to be considered.

The obtained results allow a rough quantification of these statements in engineering terms, although they need to be differentiated. The average reconstruction error to be expected with NSBSH for simply supported boundary conditions is $\pm 1\,\mathrm{dB}$, for infinite conditions $\pm 2\,\mathrm{dB}$, and for completely free boundaries it ranges from $-1\,\mathrm{dB}$ to $+3\,\mathrm{dB}$, approximately. The average reconstruction error to be expected with KHI is roughly $\pm 2\,\mathrm{dB}$ for simply supported and infinite boundary conditions and decreases with frequency from $+4\,\mathrm{dB}$ to $\pm 1\,\mathrm{dB}$ for free boundaries. Measurement at a distance of approximately $\lambda_B/6$ from the boundaries is generally required to use KHI with good conscience. It has been shown that at specific frequencies and positions the actual reconstruction error may be well above these averaged values, mostly when drops in the response have to be predicted. Assuming one does want to keep measurements within a couple of centimeters from the edges and the source area, the considered wavelengths should therefore not exceed 0.25 m-0.30 m.

Given small wavelengths, a large number of sampling points are required, naturally. The smallest considered bending wavelength was 0.09 m, which in total required about 180 measurement positions for NSBSH and a rather frightening 290 for KHI. It can be concluded that for anything other than low-frequency analysis, the engineer without a professional laser scanning system will need to dedicate a substantial amount of time.

NSBSH in particular relies on severe data processing. Tikhonov regularization with a regularization parameter $\lambda = 5 \cdot 10^{-3}$ was applied, meaning that regularization had to be intensified compared to the simulations. The empirical functions for the cut-off value of the wavenumber remained unchanged from Chapter 5. It was shown that the method requires frequency averaging in order to mitigate frequent over- and undershooting, which means that it is not very well suited to analyze narrow band spectra.

Naturally, the experiment introduces some additional error caused by inaccuracies of the measurement positions, measurement noise or unaccounted physical effects. Moreover, the assumption of a pure bending wave field can only hold to a certain extent in practice, especially at high frequencies. As wavelengths become smaller, the setup will facilitate moment excitation and even the conversion from

bending waves to other wave types will occur, resulting in a field that does not satisfy the primary theoretical assumptions. For the wavelengths considered in this thesis, such effects are assumed to be reasonably small, however.

7

Concluding remarks

The extrapolation of bending wave fields in homogenous plates was investigated. From a number of structural response measurements along the edges and around the area of excitation, the continuous spatial field and the spectra of the response were reconstructed without knowledge of the mechanical boundaries or the magnitude and exact location of the excitation forces. Two general approaches were therefore presented. The first one, referred to as NSBSH, applies the principle behind Fourier transform-based Near-Field Acoustic Holography (NAH) and includes the structural near-field deliberately. The second approach, referred to as KHI, utilizes the Kirchhoff-Helmholtz integral and requires far-field conditions at the measurement positions.

The theoretical considerations, numerical investigations and practical results that constitute this thesis are certainly conclusive. Is it possible to exercise a form of Near-Field Acoustic Holography in a pure structure-borne sound setting? Yes, it is. But the analytical Fourier transform-based way of doing so imposes severe limitations on the measurement geometry and the extrapolatable field area. The limitations are even bigger than in NAH because the medium is usually bound in every direction, and to some extent the utilized propagation functions impose a limitation with regard to the mechanical boundary conditions of the plate. The search for a suitable set of analytical solutions leaves only the polar coordinate system, which is not conformal to most plate structures.

Does the inclusion of the structural near-field benefit the reconstruction like the hydrodynamic near-field benefits its airborne paragon? No, not to the same extent. It was shown that choosing the near-field-based method can certainly improve the reconstruction error by several decibels compared to the investigated far-field method, but only in the presence of a strong near-field and for large wavelengths. In any other regard there is no big advantage. On the contrary, given a free plate, where the near-field influence is the strongest, the physical model used for NSBSH is not the best fit. The method therefore tends to be at its most inaccurate exactly

when it should be at its best. This leads to the conclusion that the supposed core virtue of the method is one of its primary challenges at the same time. Should the need for an accurate extrapolation method in the presence of near-fields in the lower or intermediate frequency range, i.e. for bending wavelengths up to 0.2 m, develop, the approach stays interesting of course.

Going forward, the most pressing question is how this kind of extrapolation can be made admissible in Cartesian coordinates besides polar coordinates. In terms of geometry, NAH started off limited as well and has since been advanced to deal with complex situations, as outlined in a literature overview by Wu [76]. If the development described therein is taken as a leading example, analytical transforms will have to be abandoned in favor of approximations in order to develop NSBSH further. It might be possible to utilize a decidedly approximate expansion of basis functions for Cartesian coordinates, with the error regarded as a minimization problem. It might also be possible to develop a numerical hybrid-approach through finite or boundary element methods by introducing additional information about the structure in question. In any way, the main challenge will be to keep the near-field included specifically. Otherwise, one would be better advised to keep it simple and turn to an approach like KHI, as presented in this thesis. This conclusion of course leads to the arguably most important question to be asked after reading the preceding chapters: Do the results for KHI justify to disregard the structural near-field, stay clear of free boundaries and enjoy the ability to choose arbitrary contours for extrapolation? If the engineer faces anything other than completely free boundaries and large wavelengths and does not need to fight over every decibel, yes.

Of course it needs to be reiterated that the main assumption made for both NSBSH and KHI is that of a homogenous and isotropic structure, which is becoming rare in industrial practice. Given that only free-space Green or propagation functions are used in both methods, it was not surprising to find that they fail if the structure is orthotropic. However, it was quickly demonstrated just how unusable both methods are if the structure is even slightly orthotropic. Therefore, even if KHI suffices for bending wave field extrapolation in a homogenous plate, the effect of structural discontinuities needs to be included in some form in order to render it truly usable in engineering practice. This is assuming that the discontinuities are spaced such that the corresponding near-fields can also be neglected. In this regard it may be helpful to look at the field of seismics, where the elastic formulation of the Kirchhoff-Helmholtz integral [77] is long since used for wave field extrapolation in a medium in which different layers cause reflection [78]. There, the field is decomposed into longitudinal and shear waves that are then extrapolated quite like the acoustic field.

It is also worth noting that, since KHI was derived from a differential equation that also describes the propagation of longitudinal waves in a plate, it could be used to extrapolate a quasi-longitudinal wave field in a plate as well. This might be another interesting path for future research.

Putting aside any limitations for the sake of discussion, are these methods feasible then? If a scanning system is available, yes. If the equipment consists of a couple of accelerometers, not so much. Of course things may look different for low-frequency analysis, where only a few measurement positions are needed. Still, this situation contradicts one of the initially stated reasons for the interest in structural wave field extrapolation. With a laser scanning system there is only need for such extrapolation if certain parts of the structure are not accessible for measurement. Disregarding monetary or time constraints, it has to be noted that the presented extrapolation of a structural wave field requires a lot of data to be sampled, and this appears to counter the initial premise.

If forced to choose one method over the other, the author would go with KHI certainly. Both methods have appealing premises, and it was proven that indeed neither the actual boundary conditions or geometry of the plate, nor the excitation forces need to be known to extrapolate the field. In the case of NSBSH, some boundary conditions will be more problematic by nature, which also counters that argument to some extent. Overcoming these problems will be a challenge, but the appeal of structure-borne wave field extrapolation surely warrants further research in this direction. As this thesis indicates, the inclusion of the structural near-field in the process is definitely possible, but not essential in most situations.

A

Fourier analysis

A.1 Fourier series

A spatially periodic function $f(s)$ with period C can be expressed in terms of the Fourier series

$$f(s) = \sum_{n=-\infty}^{\infty} a_n \mathrm{e}^{-jk_n s}, \quad k_n = \frac{2\pi n}{C}, \tag{A.1.1}$$

where its coefficients are given by

$$a_n = \frac{1}{C} \int_0^C f(s) \mathrm{e}^{jk_n s} \, \mathrm{d}s. \tag{A.1.2}$$

Hereby, k_n can be regarded as a harmonic spatial frequency and $1/C$ as the fundamental spatial frequency.

A.2 Relation between Fourier series and continuous Fourier transform

Because of the discreteness of the spatial fequencies, i.e. wavenumbers, considered by Eq. (A.1.1), one can formulate

$$\Delta k = \frac{2\pi}{C} \leftrightarrow \frac{1}{C} = \frac{\Delta k}{2\pi}. \tag{A.2.1}$$

The integral limits in Eq. (A.1.2) can be changed:

$$a_n = \frac{1}{C} \int_{-C/2}^{C/2} f(s) \mathrm{e}^{jk_n s} \, \mathrm{d}s. \tag{A.2.2}$$

Using Eq. (A.2.1) and injecting Eq. (A.2.2) into Eq. (A.1.1) results in

$$\begin{aligned} f(s) = &\sum_{n=-\infty}^{\infty} \frac{\Delta k}{2\pi} \int_{-C/2}^{C/2} f(s) \mathrm{e}^{jk_n s} \, \mathrm{d}s \, \mathrm{e}^{-jk_n s} \\ =&\frac{1}{2\pi} \sum_{n=-\infty}^{\infty} \mathrm{e}^{-jk_n s} \int_{-C/2}^{C/2} f(s) \mathrm{e}^{jk_n s} \, \mathrm{d}s \, \Delta k \\ \equiv&\frac{1}{2\pi} \sum_{n=-\infty}^{\infty} \mathrm{e}^{-jk_n s} F(k) \, \Delta k. \end{aligned} \tag{A.2.3}$$

It shall now be assumed that $f(s)$ is a non-periodic function by letting the period become infinite. For $C \to \infty$ it follows that $\Delta k \to dk$, wherefore the sum in Eq. (A.2.3) turns into an integral. As a consequence, the Fourier series becomes the inverse Fourier transform

$$f(s) = \frac{1}{2\pi} \int_{-\infty}^{\infty} F(k) \mathrm{e}^{-jks} \, dk \equiv \mathcal{F}_s^{-1}\{F(k)\}, \tag{A.2.4}$$

with the forward Fourier transform

$$F(k) = \int_{-\infty}^{\infty} f(s) \mathrm{e}^{jks} \, ds \equiv \mathcal{F}_s\{f(s)\}. \tag{A.2.5}$$

This short deduction shows that for a spatially non-periodic function, in which case an infinite set of infinitesimally narrow wavenumbers is needed, the Fourier series becomes a continuous Fourier integral. For a periodic function, which can be seen as a special case of a non-periodic function, the continuous Fourier transform must be applicable as well as a consequence. The continuous Fourier transform will then return discrete amplitudes which constitute the series coefficients that build the Fourier series.

A.3 Relation between Fourier series and discrete Fourier transform

The periodic spatial function $f(mS)$, sampled in the mth interval S, shall be considered instead of the continuous function $f(s)$. Discrete sampling of a continuous function can be mathematically expressed as a multiplication by an impulse train

$$\Psi_S(s) = S \sum_{m=-\infty}^{\infty} \delta(s - m\Delta S). \tag{A.3.1}$$

After replacing $f(s)$ in Eq. (A.1.2) with

$$f_{\mathrm{smp}}(s) = f(s)\Psi_S(s), \tag{A.3.2}$$

the sifting property of the delta function leads to the Fourier series coefficients of the sampled function

$$a_{n,\mathrm{smp}} = \frac{1}{C}\int_0^C f_{\mathrm{smp}}(s)\ \mathrm{e}^{jk_n s}\ \mathrm{d}s = \frac{1}{C}\sum_{m=0}^{(C/S)-1} f(mS)\ \mathrm{e}^{jk_n mS} S. \tag{A.3.3}$$

For an integer number of sampling points $M = C/S$, Eq. (A.3.3) becomes

$$\begin{aligned} a_{n,\mathrm{smp}} &= \frac{S}{C}\sum_{m=0}^{M-1} f(mS)\ \mathrm{e}^{jk_n mS} = \frac{1}{M}\sum_{m=0}^{M-1} f(mS)\ \mathrm{e}^{jk_n mS} \\ &= \frac{1}{M}\sum_{m=0}^{M-1} f(mS)\ \mathrm{e}^{j2\pi nm/M}, \end{aligned} \tag{A.3.4}$$

which demonstrates that for a discretely sampled periodic signal the coefficients of a Fourier series are given by the discrete Fourier transform (DFT), divided by the number of sampling points within a period. The above deduction has been made analogously to the time domain [79].

The conclusion of the considerations in Appendices A.2 and A.3 concerns the implementation of NSBSH. The velocity distribution along a closed contour may have been derived as a Fourier series in polar coordinates, but thanks to the inherent spatial periodicity this is actually the inverse Fourier transform of a series of coefficients that can be obtained by taking the Fourier transform. Recognizing that discrete sampling is necessary in practice, it is reassuring to know that the sought-after series coefficients will be obtained by taking the DFT of the spatial distribution along the contours. In terms of numerical implementation, basic FFT-routines can be used to exercise the DFT.

A.4 Definition of the temporal Fourier transform

The forward transform from time domain to frequency domain is considered to be

$$F(\omega) = \int_{-\infty}^{\infty} f(t)\mathrm{e}^{-j\omega t}\ \mathrm{d}t \equiv \mathcal{F}_t\{f(t)\}, \tag{A.4.1}$$

resulting in the corresponding inverse transform

$$f(t) = \frac{1}{2\pi}\int_{-\infty}^{\infty} F(\omega)\mathrm{e}^{j\omega t}\ \mathrm{d}\omega \equiv \mathcal{F}_t^{-1}\{F(\omega)\}. \tag{A.4.2}$$

A.5 Definition of the spatial Fourier transform in one dimension

The forward transform from spatial domain to wavenumber domain is considered to be

$$F(k_x) = \int_{-\infty}^{\infty} f(x) \mathrm{e}^{jk_x x} \, \mathrm{d}x \equiv \mathcal{F}_x\{f(x)\}, \tag{A.5.1}$$

resulting in the corresponding inverse transform

$$f(x) = \frac{1}{2\pi} \int_{-\infty}^{\infty} F(k_x) \mathrm{e}^{-jk_x x} \, \mathrm{d}k_x \equiv \mathcal{F}_x^{-1}\{F(k_x)\}. \tag{A.5.2}$$

In comparison to the temporal Fourier transforms, the sign in the argument of the exponential functions is changed. This is done to use a physically reasonable convention, in which waves propagate in positive x-direction with progressing time.

For NSBSH, as imagined in this thesis, a polar coordinate system is used. The Fourier transform has to be taken in the φ-coordinate along a closed circular contour that is 2π-periodic in φ. A corresponding transform pair can be defined as follows:

$$F_n(r) = \int_{-\pi}^{\pi} f(r, \varphi) \mathrm{e}^{jn\varphi} \, \mathrm{d}\varphi \equiv \mathcal{F}_\varphi\{f(r, \varphi)\}, \tag{A.5.3}$$

$$f(r, \varphi) = \frac{1}{2\pi} \sum_{-\infty}^{\infty} F_n(r) \mathrm{e}^{-jn\varphi} \, \mathrm{d}n \equiv \mathcal{F}_\varphi^{-1}\{F_n(r)\}. \tag{A.5.4}$$

A.6 Definition of the spatial Fourier transform in two dimensions

The transform pair that relates spatial domain and wavenumber domain in two dimensions is considered to be

$$F(k_x, k_y) = \iint_{-\infty}^{\infty} f(x, y) \mathrm{e}^{jk_x x} \mathrm{e}^{jk_y y} \, \mathrm{d}x \, \mathrm{d}y \equiv \mathcal{F}_x \mathcal{F}_y\{f(x, y)\}, \tag{A.6.1}$$

$$f(x, y) = \frac{1}{(2\pi)^2} \iint_{-\infty}^{\infty} F(k_x, k_y) \mathrm{e}^{-jk_x x} \mathrm{e}^{-jk_y y} \, \mathrm{d}k_x \, \mathrm{d}k_y \equiv \mathcal{F}_x^{-1} \mathcal{F}_y^{-1}\{F(k_x, k_y)\}. \tag{A.6.2}$$

B

Integral representation of the Hankel function of second kind

For the modified Bessel function of the second kind $K_n(z)$, Abramowitz and Stegun [49] give the following relationships:

$$K_n(z) = \int_0^\infty \mathrm{e}^{-z\cosh(\upsilon)} \cosh(n\upsilon)\, \mathrm{d}\upsilon, \tag{B.0.1}$$

$$K_n(z) = -\frac{\pi j}{2} \mathrm{e}^{-\frac{1}{2}n\pi j} H_n^{(2)}(z\mathrm{e}^{-\frac{1}{2}\pi j}). \tag{B.0.2}$$

For $n = 0$, Eq. (B.0.1) can be rewritten as

$$K_0(z) = \int_0^\infty \mathrm{e}^{-z\cosh(\upsilon)}\, \mathrm{d}\upsilon = \frac{1}{2}\int_{-\infty}^\infty \mathrm{e}^{-z\cosh(\upsilon)}\, \mathrm{d}\upsilon, \tag{B.0.3}$$

and Eq. (B.0.2) can be rewritten as

$$K_0(z) = -\frac{\pi j}{2} H_0^{(2)}(-zj). \tag{B.0.4}$$

From Eqs. (B.0.3) and (B.0.4) it can be concluded that

$$H_0^{(2)}(z) = \frac{j}{\pi}\int_{-\infty}^\infty \mathrm{e}^{-jz\cosh(\upsilon)}\, \mathrm{d}\upsilon. \tag{B.0.5}$$

C

Solutions for the expansion coefficients

C.1 Infinite plate

The solutions for the expansion coefficients in Eq. (3.2.28) are found to be

$$A_n = \frac{v_n(r_2)H_n^{(2)}(-jk_Br_1) - v_n(r_1)H_n^{(2)}(-jk_Br_2)}{H_n^{(2)}(k_Br_2)H_n^{(2)}(-jk_Br_1) - H_n^{(2)}(k_Br_1)H_n^{(2)}(-jk_Br_2)}, \tag{C.1.1}$$

$$B_n = \frac{-H_n^{(2)}(k_Br_1)\{v_n(r_2)H_n^{(2)}(-jk_Br_1) - v_n(r_1)H_n^{(2)}(-jk_Br_2)\}}{H_n^{(2)}(-jk_Br_1)\{H_n^{(2)}(k_Br_2)H_n^{(2)}(-jk_Br_1) - H_n^{(2)}(k_Br_1)H_n^{(2)}(-jk_Br_2)\}} + \frac{v_n(r_1)}{H_n^{(2)}(-jk_Br_1)}. \tag{C.1.2}$$

C.2 Finite plate

The solutions for the expansion coefficients in Eq. (3.2.32) are found to be

$$A_n = \frac{v_n(r_1) - B_n K_2 - C_n K_3 - D_n K_4}{K_1}, \tag{C.2.1}$$

$$B_n = \frac{v_n(r_2) - K_5 \dfrac{v_n(r_1)}{K_1} - C_n \dfrac{K_7 - K_3 K_5}{K_1} - D_n \dfrac{K_8 - K_4 K_5}{K_1}}{\dfrac{K_6 - K_2 K_5}{K_1}}, \tag{C.2.2}$$

$$C_n = \frac{E_5 - D_n E_3}{E_1}, \tag{C.2.3}$$

$$D_n = \frac{E_6 - \dfrac{E_2 E_5}{E_1}}{E_4 - \dfrac{E_3 E_2}{E_1}}, \tag{C.2.4}$$

with

$$E_1 = K_{11} - \frac{K_3 K_9}{K_1} - \left\{ K_7 - \frac{K_3 K_5}{K_1} \right\} \frac{K_{10} - \dfrac{K_2 K_9}{K_1}}{K_6 - \dfrac{K_2 K_5}{K_1}}, \tag{C.2.5}$$

$$E_2 = K_{15} - \frac{K_3 K_{13}}{K_1} - \left\{ K_7 - \frac{K_3 K_5}{K_1} \right\} \frac{K_{14} - \dfrac{K_2 K_{13}}{K_1}}{K_6 - \dfrac{K_2 K_5}{K_1}}, \tag{C.2.6}$$

$$E_3 = K_{12} - \frac{K_4 K_9}{K_1} - \left\{ K_8 - \frac{K_4 K_5}{K_1} \right\} \frac{K_{10} - \dfrac{K_2 K_9}{K_1}}{K_6 - \dfrac{K_2 K_5}{K_1}}, \tag{C.2.7}$$

$$E_4 = K_{16} - \frac{K_4 K_{13}}{K_1} - \left\{ K_8 - \frac{K_4 K_5}{K_1} \right\} \frac{K_{14} - \dfrac{K_2 K_{13}}{K_1}}{K_6 - \dfrac{K_2 K_5}{K_1}}, \tag{C.2.8}$$

where

$$K_1 = H_n^{(2)}(k_B r_1), \tag{C.2.9}$$
$$K_2 = H_n^{(2)}(-jk_B r_1), \tag{C.2.10}$$
$$K_3 = H_n^{(1)}(k_B r_1), \tag{C.2.11}$$
$$K_4 = H_n^{(1)}(-jk_B r_1), \tag{C.2.12}$$
$$K_5 = H_n^{(2)}(k_B r_2), \tag{C.2.13}$$
$$K_6 = H_n^{(2)}(-jk_B r_2), \tag{C.2.14}$$
$$K_7 = H_n^{(1)}(k_B r_2), \tag{C.2.15}$$
$$K_8 = H_n^{(1)}(-jk_B r_2), \tag{C.2.16}$$
$$K_9 = H_n^{(2)}(k_B r_3), \tag{C.2.17}$$
$$K_{10} = H_n^{(2)}(-jk_B r_3), \tag{C.2.18}$$
$$K_{11} = H_n^{(1)}(k_B r_3), \tag{C.2.19}$$
$$K_{12} = H_n^{(1)}(-jk_B r_3), \tag{C.2.20}$$
$$K_{13} = H_n^{(2)}(k_B r_4), \tag{C.2.21}$$
$$K_{14} = H_n^{(2)}(-jk_B r_4), \tag{C.2.22}$$
$$K_{15} = H_n^{(1)}(k_B r_4), \tag{C.2.23}$$
$$K_{16} = H_n^{(1)}(-jk_B r_4). \tag{C.2.24}$$

D

Solutions to the forced vibration problems

D.1 Infinite plate

The analytical solution to the problem of a thin, isotropic, infinite plate excited by a set of normal point forces is found by superposing the following solution for a single excitation in polar coordinates [42]

$$v(r,\omega) = F_0 Y_{\mathrm{pl},\infty}[H_0^{(2)}(k_B r) - H_0^{(2)}(-jk_B r)]. \tag{D.1.1}$$

Equation (D.1.1) contains the point mobility of an infinite plate, established as

$$Y_{\mathrm{pl},\infty} = \frac{1}{8\sqrt{B'm''}}. \tag{D.1.2}$$

The mechanical mobility in general is a complex frequency response function [80], defined as

$$Y_{i,j}(\omega) = \frac{v_i(\omega)}{F_j(\omega)}, \tag{D.1.3}$$

where $F_j(\omega)$ is the complex amplitude of the excitation force and $v_i(\omega)$ is that of the resulting velocity response.
The point mobility describes the case in which the position $i = j$. As seen in Eq. (D.1.2), in the case of an infinite plate it is independent of frequency.
The plate response to a number of point excitations is obtained by linear superposition of the single responses

$$v(r,\omega) = \sum_{j=1}^{N} F_j Y_{\mathrm{pl},\infty}[H_0^{(2)}(k_B r_j) - H_0^{(2)}(-jk_B r_j)], \tag{D.1.4}$$

with the relation between polar and Cartesian coordinates

$$r_j = \sqrt{(x_j - x)^2 + (y_j - y)^2}, \tag{D.1.5}$$

where the index j denotes the excitation point.

D.2 Stiffened infinite plate

The solution to the problem of a stiffened infinite plate excited by a set of normal point forces is found by using a force substitution approach. A thin infinite plate is coupled with infinite Euler-beams along a finite number of coupling points. The initial excitation is assumed to cause certain reactive forces at the coupling points, so that the response of the stiffened plate can be considered as the superposition of the response to the initial excitation force and the reactive forces. Reactive moments are neglected, such as the contribution of coupling effects. The utilized model is depicted in Fig. D.1, but for a detailed explanation of the approach it is referred to the source paper [73].

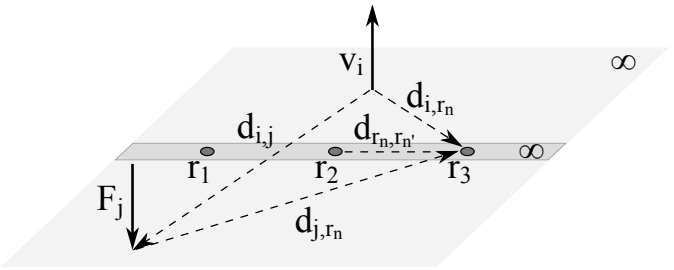

Figure D.1: Geometry for the modeling of a stiffened infinite plate: infinite plate point-coupled with an infinite beam.

The velocity at the excitation point j is given by

$$v_j = Y_{\mathrm{pl},\infty} F_j - Y_{j,r_n}[Y_{r_n,r_{n'}} + Y_{\mathrm{be},r_n,r_{n'}}]^{-1} Y_{r_n,j} F_j, \tag{D.2.1}$$

with

$$Y_{j,r_n} = Y_{\mathrm{pl},\infty}[H_0^{(2)}(k_B d_{j,r_n}) - H_0^{(2)}(-jk_B d_{j,r_n})], \tag{D.2.2}$$

$$Y_{r_n,r_{n'}} = Y_{\mathrm{pl},\infty}[H_0^{(2)}(k_B d_{r_n,r_{n'}}) - H_0^{(2)}(-jk_B d_{r_n,r_{n'}})], \tag{D.2.3}$$

$$Y_{\mathrm{be},r_n,r_{n'}} = \frac{\omega}{4Bk_B^3}[\mathrm{e}^{-jk_B d_{r_n,r_{n'}}} - j\mathrm{e}^{-jk_B d_{r_n,r_{n'}}}], \tag{D.2.4}$$

$$Y_{r_n,j} = Y_{\mathrm{pl},\infty}[H_0^{(2)}(k_B d_{r_n,j}) - H_0^{(2)}(-jk_B d_{r_n,j})]. \tag{D.2.5}$$

Y_{j,r_n} is the matrix of transfer mobilities between the excitation point and the coupling points for the uncoupled infinite plate. $Y_{r_n,r_{n'}}$ is the mobility matrix

for the coupling points of the uncoupled infinite plate. $Y_{\mathrm{be},r_n,r_{n'}}$ is the mobility matrix for the coupling points of the uncoupled infinite beam. The matrix built by Eq. (D.2.3) gives the point mobility of an infinite plate $Y_{\mathrm{pl},\infty}$ when $r_n = r_{n'}$. Equivalently, the matrix built by Eq. (D.2.4) gives the point mobility of an infinite beam

$$Y_{\mathrm{be},\infty} = \frac{\omega(1-j)}{4Bk_B^3} \tag{D.2.6}$$

when $r_n = r_{n'}$. $Y_{r_n,j}$ is the matrix of transfer mobilities between the coupling points and the excitation point for the uncoupled infinite plate.

The velocity at the response point i is given by

$$v_i = Y_{i,j}F_j - Y_{i,r_n}[Y_{r_n,r_{n'}} + Y_{\mathrm{be},r_n,r_{n'}}]^{-1}Y_{r_n,j}F_j, \tag{D.2.7}$$

with

$$Y_{i,j} = Y_{\mathrm{pl},\infty}[H_0^{(2)}(k_B d_{i,j}) - H_0^{(2)}(-jk_B d_{i,j})], \tag{D.2.8}$$

$$Y_{i,r_n} = Y_{\mathrm{pl},\infty}[H_0^{(2)}(k_B d_{i,r_n}) - H_0^{(2)}(-jk_B d_{i,r_n})]. \tag{D.2.9}$$

D.3 Simply supported plate

The analytical solution to the problem of a thin, isotropic, simply supported plate, excited by a normal point force F_0 at the position x_0, y_0, is found by superposing a set of orthogonal modes [28]:

$$v(x,y,\omega) = \frac{j\omega F_0}{m''}\sum_{m=1}^{\infty}\sum_{n=1}^{\infty}\frac{\Psi_{mn}(x_0,y_0)\Psi_{mn}(x,y)}{\omega^2-\omega_n^2}, \tag{D.3.1}$$

with

$$\Psi_{mn}(x,y) = \frac{2}{\sqrt{L_x L_y}}\sin(\frac{m\pi x}{L_x})\sin(\frac{n\pi y}{L_y}) \tag{D.3.2}$$

and

$$\omega_{mn} = \sqrt{\frac{B'}{m''}}\left[(\frac{m\pi}{L_x})^2 + (\frac{n\pi}{L_y})^2\right], \tag{D.3.3}$$

where $n = \{1,2,3,...\}, m = \{1,2,3,...\}$. The plate response to a whole set of point forces is obtained by linear superposition of the single responses.

D.4 Free plate

The solution to the problem of an all-around free plate excited by a set of normal point forces is obtained from FEM-analysis, using the *Structural Mechanics Module* of the commercial software COMSOL™, version 4.2. A two-dimensional mesh of triangular elements is used, with the maximum length of the elements set to $\lambda_B/10$. The normal velocity values calculated by COMSOL are then exported into MATLAB®.

List of figures

List of tables

Nomenclature

Symbol		Unit	Page
A_n	arbitrary expansion coefficient		18
B	bending stiffness of a beam	Nm^2	142
B'	bending stiffness of a plate	Nm	15
B_n	arbitrary expansion coefficient		18
C	spatial period	m	131
C_n	arbitrary expansion coefficient		20
D_n	arbitrary expansion coefficient		20
F	force	N	141
F_0	excitation force	N	42
$G(...)$	Green's function in free space		42
$H_n^{(1)}(...)$	nth order Hankel function of the first kind		17
$H_n^{(2)}(...)$	nth order Hankel function of the second kind		17
$J_n(...)$	nth order Bessel function		17
K	arbitrary coefficient		138
K	coefficient in the Kirchhoff-Helmholtz integral		47
$K_n(...)$	nth order modified Bessel function		135
N	number of sampling points along a single contour		24
N_{tot}	total number of sampling points		62
P	acoustic sound power	W	59
Q	arbitrary coefficient		138
$Q^{\mathrm{f}}(...)$	propagation function for the velocity in a homogenous fluid		13
$Q_n^{\mathrm{fin}}(...)$	propagation function for the normal velocity of a finite plate		20
$\mathbf{Q}_n^{\mathrm{fin}}(...)$	propagation function for the normal velocity of a finite plate (vector notation)		20
$Q_n^{\mathrm{inf}}(...)$	propagation function for the normal velocity of an infinite plate		19

$\mathbf{Q}_n^{\mathrm{inf}}(...)$	propagation function for the normal velocity of an infinite plate (vector notation)		19
$R(...)$	arbitrary function		16
S	surface	m^2	45
V	volume	m^3	45
$Y(...)$	mechanical mobility	m/(Ns)	141
$Y_n(...)$	nth order Neumann function		17
$Y_{\mathrm{pl},\infty}(...)$	mechanical point mobility of an infinite plate	m/(Ns)	141
$X_f(...)$	planar wavenumber filter for a homogenous fluid		35
$X_p(...)$	wavenumber filter for the considered plate		35
a_n	arbitrary expansion coefficient		17
b_n	arbitrary expansion coefficient		17
c	speed of sound in a homogenous fluid	m/s	59
c_B	simple bending wave phase velocity	m/s	20
$c_{B,\mathrm{corr}}$	corrected bending wave phase velocity	m/s	20
c_n	arbitrary expansion coefficient		17
d_n	arbitrary expansion coefficient		17
d_{span}	distance between inner and outer hologram contour	m	37
d_{st}	standoff distance	m	23
h	thickness	m	20
j	imaginary unit		13
k	wavenumber in a homogenous fluid	1/m	13
k_B	simple bending wavenumber	1/m	15
$k_{B,\mathrm{corr}}$	corrected bending wavenumber	1/m	20
k_c	cut-off value for wavenumbers		35
$k_{x,y,z}$	wavenumber in a homogenous fluid in x-, y- or z-direction	1/m	13
k_φ	circumferential wavenumber in a homogenous fluid	1/m	13
m''	mass per unit area	$\mathrm{kg/m}^2$	15
n	order of the Fourier component		16
n	direction vector normal to the boundary contour		44
n_c	cut-off value for orders		35
p	sound pressure	$\mathrm{N/m}^2$	13
r	general coordinate or radius	m	13
t	time	s	15
u	displacement	m	15
v	velocity	m/s	15
v_n	nth Fourier component of the normal velocity	m/s	17
Δd_{st}	hologram contour distance (NSBSH)	m	23

$\Delta L_H(...)$	relative decay of the evanescent wave	dB	32
$\Delta L_v(...)$	velocity level difference	dB	59
$\Delta L_{\overline{v}}(...)$	level difference of the spatially averaged square velocity	dB	59
$\Delta L_{v,\mathrm{input}}(...)$	level difference between contaminated and accurate input data	dB	58
Δr	boundary contour distance	m	51
Δx	sampling point distance	m	24
$\Phi(...)$	arbitrary function		16
$\Psi(...)$	arbitrary function		45
$\Omega(...)$	smoothing norm		38
Ω	surface	m^2	46
α	filter slope		35
α_n	arbitrary expansion coefficient		17
α_n^*	arbitrary expansion coefficient		18
β_n	arbitrary expansion coefficient		17
β_n^*	arbitrary expansion coefficient		18
γ_n	arbitrary expansion coefficient		17
$\delta(...)$	dirac function		42
δ_n	arbitrary expansion coefficient		17
ϵ	radius	m	46
λ	regularization parameter		38
λ_B	bending wavelength	m	20
ρ_0	density in a surrounding fluid	kg/m^3	59
σ	radiation efficiency		59
σ_i	singular value		37
σ_v	standard deviation of the simulated velocity magnitude	m/s	58
σ_ϕ	standard deviation of the simulated velocity phase	rad	58
ϕ	phase angle	rad	92
φ	angle	rad	13
ω	angular frequency	1/s	15

Abbreviation		Page
BEM	Boundary Element Method	8
BWPM	number of bending wavelengths per unit meter	8
DFT	discrete Fourier transform	24
FEM	Finite Element Method	7
FFT	fast Fourier Transform	24

FR	force reconstruction	5
KHI	Kirchhoff-Helmholtz integral extrapolation	44
NAH	Near-Field Acoustic Holography	8
NSBSH	Near-Field Structure-Borne Sound Holography	22

Operator

$\nabla^2 = \Delta$	squared Nabla, Laplace
∂	partial derivative
d	total derivative
min(...)	minimium of the function
argmin(...)	argument that minimizes the function
Re(...)	real part
Im(...)	imaginary part
$\underline{\lvert(...)\rvert}$	magnitude
$\overline{(...)}$	average
$(...)^T$	transpose
$(...)^{-1}$	inverse

Bibliography

[1] **Bobrovnitskii, Y. I.** The problem of vibration field reconstruction: statement and general properties. *Journal of Sound and Vibration*, 247: 145–163, 2001.

[2] **Dobson, B. J.** and **Rider, E.** A review of the indirect calcuation of excitation forces from measured structural response data. *Proceedings of the Institution of Mechanical Engineers, Part C: Journal of Mechanical Engineering Science*, 204: 69–75, 1990.

[3] **Zhang, Y.** and **Adin Mann III, J.** Measuring the structural intensity and force distribution in plates. *Journal of the Acoustical Society of America*, 99: 345–353, 1996.

[4] **Zhang, Y.** and **Adin Mann III, J.** Examples of using structural intensity and the force distribution to study vibrating plates. *Journal of the Acoustical Society of America*, 99: 354–361, 1996.

[5] **Pezerat, C.** and **Guyader, J. L.** Force analysis technique: reconstruction of force distribution on plates. *Acustica united with Acta Acustica*, 86: 322–332, 2000.

[6] **Pezerat, C.** and **Guyader, J. L.** Two inverse methods for localization of external sources exiting a beam. *Acta Acoustica*, 3: 1–10, 1995.

[7] **Liu, Y.** and **Shepard Jr., W. S.** An improved method for the reconstruction of a distributed force acting on a vibrating structure. *Journal of Sound and Vibration*, 291: 369–387, 2006.

[8] **Jiang, X. Q.** and **Hu, H. Y.** Reconstruction of distributed dynamic loads on a thin plate via mode-selection and consistent spatial expression. *Journal of Sound and Vibration*, 323: 626–644, 2009.

[9] **Karlsson, S. E. S.** Identification of external structural loads from measured harmonic responses. *Journal of Sound and Vibration*, 196: 59–74, 1996.

[10] **Williams, E. G.**, **Dardy, H. D.** and **Fink, R. G.** A technique for measurement of structure-borne intensity in plates. *Journal of the Acoustical Society of America*, 78: 2061–2068, 1985.

[11] **Pascal, J.-C.**, **Loyau, T.** and **Carniel, X.** Complete determination of structural intensity in plates using laser vibrometers. *Journal of Sound and Vibration*, 161: 527–531, 1993.

[12] **Morikawa, R.**, **Sadayuki, U.** and **Nakamura, K.** Error evaluation of the structural intensity measured with a scanning laser doppler vibrometer and a k-space signal processing. *Journal of the Acoustical Society of America*, 99: 2913–2921, 1996.

[13] **Nejade, A.** and **Singh, R.** Flexural intensity measurement on finite plates using modal spectrum ideal filtering. *Journal of Sound and Vibration*, 256: 33–63, 2002.

[14] **Arruda, J. R. F.** and **Mas, P.** Localizing energy sources and sinks in plates using power flow maps computed from laser vibrometer measurements. *Shock and Vibration*, 5: 235–253, 1998.

[15] **Halkyard, C. R.** and **Mace, B. R.** A fourier series approach to the measurement of flexural wave intensity in plates. *Journal of Sound and Vibration*, 203: 101–126, 1997.

[16] **Tessler, A.** and **Spangler, J. L.** Inverse FEM for full-field reconstruction of elastic deformations in shear deformable plates and shells. *Proceedings of the second European workshop on structural health monitoring, Munich, Germany*. 2004.

[17] **Tessler, A.** and **Spangler, J. L.** A least-squares variational method for full-field reconstruction of elastic deformations in shear-deformable plates and shells. *Computer Methods in Applied Mechanics and Engineering*, 194: 327–339, 2005.

[18] **Chierichetti, M.** and **Ruzzene, M.** Dynamic displacement field reconstruction through a limited set of measurements: application to plates. *Journal of Sound and Vibration*, 331: 4713–4728, 2012.

[19] **Berkhout, A. J.**, **de Vries, D.** and **Brink, M. C.** Array technology for bending wave field analysis in constructions. *Journal of Sound and Vibration*, 300: 25–42, 2007.

[20] **Maginness, M. G.** The reconstruction of elastic wave fields from measurements over a transducer array. *Journal of Sound and Vibration*, 20: 219–240, 1972.

[21] **Hoerchens, L.** Imaging of material inhomogeneities with flexural waves. Ph.D. thesis, Technische Universiteit Delft, 2010.

[22] **Hoerchens, L.** and **de Vries, D.** Acoustical imaging in beams and plates using boundary reflections. *Proceedings of Forum Acusticum 2011, Aalborg, Denmark, P. 2373-2378.* 2011.

[23] **Doelman, N. J.** A general theory for wave field extrapolation in bounded and unbounded homogenous media. *Journal of the Acoustical Society of America*, 88: 1964–1974, 1990.

[24] **Berkhout, A. J.** *Applied seismic wave theory.* Elsevier Science Publishers B. V., 1987.

[25] **Wapenaar, C. P. A.** Kirchhoff-Helmholtz downward extrapolation in a layered medium with curved interfaces. *Geophysical Journal International*, 115: 445–455, 1993.

[26] **Berkhout, A. J.**, **de Vries, D.** and **Vogel, P.** Acoustic control by wave field synthesis. *Journal of the Acoustical Society of America*, 93: 2764–2778, 1993.

[27] **Hildebrand, B. P.** and **Brenden, B. B.** *An introduction to acoustical holography.* Plenum Press, New York, 1974.

[28] **Williams, E. G.** *Fourier acoustics.* Academic Press, 1999.

[29] **Williams, E. G.** and **Maynard, J. D.** Holographic imaging without the wavelength resolution limit. *Physical Review Letters*, 45: 554–557, 1980.

[30] **Maynard, J. D.**, **Williams, E. G.** and **Lee, Y.** Nearfield acoustic holography: I. Theory of generalized holography and the development of NAH. *Journal of the Acoustical Society of America*, 78: 1395–1413, 1985.

[31] **Williams, E. G.** and **Dardy, H. D.** Generalized nearfield acoustical holography for cylindrical geometry: theory and experiment. *Journal of the Acoustical Society of America*, 81: 389–407, 1987.

[32] **Candel, S. M.** and **Chassaignon, C.** Radial extrapolation of wave fields by spectral methods. *Journal of the Acoustical Society of America*, 76: 1823–1828, 1984.

[33] **Blacodon, D.**, **Candel, S. M.** and **Elias, G.** Radial extrapolation of wave fields from synthetic measurements of the nearfield. *Journal of the Acoustical Society of America*, 82: 1060–1072, 1987.

[34] **Veronesi, W. A.** and **Maynard, J. D.** Digital holographic reconstruction of sources with arbitrarily shaped surfaces. *Journal of the Acoustical Society of America*, 85: 588–598, 1989.

[35] **Kim, G.-T.** and **Lee, B. H.** 3-D sound source reconstruction and field reprediction using the Helmholtz integral equation. *Journal of Sound and Vibration*, 136: 245–261, 1990.

[36] **Bai, M. R.** Application of BEM (boundary element method)-based acoustic holography to radiation analysis of sound sources with arbitrarily shaped geometries. *Journal of the Acoustical Society of America*, 92: 533–549, 1992.

[37] **Kim, B.-K.** and **Ih, J.-G.** On the reconstruction of vibro-acoustic field over the surface enclosing an interior space using the boundary element method. *Journal of the Acoustical Society of America*, 100: 3003–3016, 1996.

[38] **Greussing, D.**, **Cavallari, M.**, **Bonhoff, H. A.** and **Petersson, B. A. T.** The conception of structure-borne-sound-based near-field holography. *Journal of Sound and Vibration*, 331: 4132–4144, 2012.

[39] **Greussing, D.** Near-field structure-borne sound holography for finite plates. *Proceedings of the 19th International Congress on Sound and Vibration (ICSV 19), Vilnius, Lithuania*. 2012.

[40] **Greussing, D.** Near-field structure-borne sound holography: theory vs. practice. *Proceedings of Noise-Con 2013, Denver, USA*. 2013.

[41] **Morse, P. M.** and **Feshbach, H.** *Methods of theoretical physics*. McGraw-Hill Book Company, 1953.

[42] **Cremer, L.**, **Heckl, M.** and **Petersson, B.** *Structure-borne sound*. Springer, 2005.

[43] **Leissa, A. W.** *Vibration of plates*. Office of technology utilization, National Aeronautics and Space Administration, Washington, D.C., 1969.

[44] **Miller, W.** *Symmetry and separation of variables*. Addison-Wesley Pub. Co., 1977.

[45] **Morse, P. M.** and **Ingard, K. U.** *Theoretical Acoustics*. McGraw-Hill Book Company, 1968.

[46] **Schot, S. H.** Eighty years of Sommerfeld's radiation condition. *Historia Mathematica*, 19: 385–401, 1992.

[47] **Poletti, M. A.** A unified theory of horizontal holographic sound systems. *Journal of the Audio Engineering Society*, 48: 1155–1182, 2000.

[48] **Kolundžija, M.** Spatial acoustic signal processing. Ph.D. thesis, École Polytechnique Fédérale De Lausanne, 2012.

[49] **Abramowitz, M.** and **Stegun, I. A.**, editors. *Handbook of mathematical functions with formulas, graphs, and mathematical tables*. Dover Publications Inc., New York, ninth Dover printing, tenth GPO printing edition, 1972.

[50] **Petersson, B. A. T.** Geometrical and spatial effects on effective mobilities of annular interfaces. *Journal of Sound and Vibration*, 202: 511–537, 1997.

[51] **Bonhoff, H. A.** and **Eslami, A.** Interface mobilities for characterization of structure-borne sound sources with multi-point coupling. *Acta Acustica united with Acustica*, 98: 384–391, 2012.

[52] **Fahy, F. J.** *Sound intensity*. E & FN Spon, 1995.

[53] **Petersson, B. A. T.** and **Heckl, M.** Concentrated excitation of structures. *Journal of Sound and Vibration*, 196: 295–321, 1996.

[54] **Pan, X.** and **Hansen, C. H.** The effect of error sensor location and type on the active control of beam vibration. *Journal of Sound and Vibration*, 165: 497–510, 1993.

[55] **Bobrovnitskii, Y. I.** On the energy flow in evanescent waves. *Journal of Sound and Vibration*, 152: 175–176, 1992.

[56] **Lande, R.** and **Langley, R.** The energetics of cylindrical bending waves in a thin plate. *Journal of Sound and Vibration*, 279: 513–518, 2005.

[57] **Noiseux, D. U.** Measurement of power flow in uniform beams and plates. *Journal of the Acoustical Society of America*, 47: 238–247, 1970.

[58] **Heckl, M. A.** Compendium of impedance formulas, Report No. 774, Job No. 110022, Office of Naval Research, Code 411, Washington 25, D. C. Technical report, Bolt Beranek and Newman Inc., 1961.

[59] **Halkyard, C. R.** and **Mace, B. R.** Feedforward adaptive control of flexural vibration in a beam using wave amplitudes. *Journal of Sound and Vibration*, 254: 117–141, 2002.

[60] **Halkyard, C. R.** and **Mace, B. C.** Adaptive active control of flexural waves in a beam in the presence of a nearfield. *Journal of Sound and Vibration*, 285: 149–171, 2005.

[61] **Kabanikhin, S. I.** Definitions and examples of inverse and ill-posed problems. *Journal of Inverse and III-posed Problems*, 16: 317–357, 2008.

[62] **Keller, J. B.** Inverse problems. *The American Mathematical Monthly*, 83: 107–118, 1976.

[63] **Hadamard, J.** Sur les problèmes aux dérivées partielles et leur signification physique. *Princeton University Bulletin*, 13: 49–52, 1902.

[64] **Veronesi, W. A.** and **Maynard, J. D.** Nearfield acoustic holography (NAH) II. Holographic reconstruction algorithms and computer implementation. *Journal of the Acoustical Society of America*, 81: 1307–1322, 1987.

[65] **Williams, E. G.** Regularization methods for near-field acoustical holography. *Journal of the Acoustical Society of America*, 110: 1976–1988, 2001.

[66] **Hansen, P. C.** *Rank-deficient and discrete ill-posed problems.* SIAM Philadelphia, 1998.

[67] **Hansen, P. C.** Regularization tools: a MATLAB package for analysis and solution of discrete ill-posed problems. version 4.1., accessed July 9th, 2013. URL `http://www.mathworks.com/matlabcentral/fileexchange/52-regtools`.

[68] **Fahy, F. J.** and **Walker, J. G.**, editors. *Fundamentals of noise and vibration.* E & FN Spon, 1998.

[69] **Spors, S.** Active listening room compensation for spatial sound reproduction systems. Ph.D. thesis, Friedrich-Alexander-Universität, Erlangen-Nürnberg, 2006.

[70] **Hänsler, E.** and **Schmidt, G.**, editors. *Topics in acoustic echo and noise control.* Springer Berlin Heidelberg New York, 2006.

[71] **Gaul, L.**, **Kögl, M.** and **Wagner, M.** *Boundary element methods for engineers and scientists.* Springer-Verlag Berlin Heidelberg New York, 2003.

[72] **Thite, A. N.** and **Thompson, J. D.** The quantification of structure-borne transmission paths by inverse methods. Part 1: Improved singular value rejection methods. *Journal of Sound and Vibration*, 264: 411–431, 2003.

[73] **Mayr, A. R.** and **Gibbs, B. M.** Point and transfer mobility of point-connected ribbed plates. *Journal of Sound and Vibration*, 330: 4798–4812, 2011.

[74] **Thite, A. N.** and **Thompson, D. J.** Selection of response measurement locations to improve inverse force determination. *Applied Acoustics*, 67: 797–818, 2006.

[75] **Champoux, Y.**, **Brunet, S.** and **Berry, A.** On the construction of a simply supported rectangular plate for noise and vibration studies. *Experimental Techniques*, 20: 24–26, 1996.

[76] **Wu, S. F.** Methods for reconstructing acoustic quantities based on acoustic pressure measurements. *Journal of the Acoustical Society of America*, 124: 2680–2697, 2008.

[77] **Pao, Y.-H.** and **V., V.** Huygens' principle, radiation conditions, and integral formulas for the scattering of elastic waves. *Journal of the Acoustical Society of America*, 59: 1361–1371, 1976.

[78] **Wapenaar, C. P. A.** and **Berkhout, A. J.** *Elastic wave field extrapolation.* Elsevier Science Publishers B. V., 1989.

[79] **Smith, J. O. I.** *Mathematics of the discrete fourier transform (DFT) with audio applications.* W3K Publishing, 2008.

[80] ISO 7626-1
Vibration and shock - experimental determination of mechanical mobility - Part 1: Basic definitions and transducers, First edition, 1986.